

AN ABSTRACT OF THE THESIS OF

Jason A. Tobias for the degree of Master of Science in Mechanical Engineering presented on June 6, 2007.

Title: Characterization of the Near-field Flow Structure of an Acoustically Self-excited Jet in a Large Enclosure Using Particle Image Velocimetry (PIV).

Abstract approved:

Vinod Narayanan

An experimental study of the near-field flow structure produced by an incompressible turbulent Acoustically Self-Excited Jet (ASEJ) in a large enclosure using Particle Image Velocimetry (PIV) is presented. The salient feature of this jet is that it provides an increase in near-field mixing and turbulence without additional external power input. In the present experiments, the jet exits into an enclosure whose nearest wall is 26 jet diameters from the nozzle center. Three nozzle exit Reynolds numbers (Re) of 27,000, 49,000 and 71,000 were studied for two frequencies of excitation of the jet, and compared with the free pipe jet without excitation. Results indicate that the peak turbulence intensity based on nozzle exit velocity in the near-field is enhanced by as much as 50 percent for the ASEJ compared to the unexcited jet at downstream locations less than 2 nozzle diameters away from the nozzle exit. The second stage of excitation is found to increase the near-field turbulence to a greater

extent than the first stage of excitation. Entrainment of surrounding air in the near-field of the jet is enhanced due to the acoustic self-excitation. Streamwise variations of streamwise mean velocity along the centerline of the jet compare well with data reported by Hasan and Hussain (1982) for both the unexcited jet and first stage ASEJ. Peak turbulent intensity along the jet centerline is lower than that reported by Hasan and Hussain (1982) for first stage ASEJ but higher for second stage ASEJ. This enhancement in turbulent intensity for second stage ASEJ is thought to be due to acoustic feedback from the enclosure walls.

©Copyright by Jason A. Tobias
June 6, 2007
All Rights Reserved

Characterization of the Near-field Flow Structure of an Acoustically Self-excited Jet in
a Large Enclosure Using Particle Image Velocimetry (PIV)

by
Jason A. Tobias

A THESIS

submitted to

Oregon State University

in partial fulfillment of
the requirements for the
degree of

Master of Science

Presented June 6, 2007
Commencement June 2008

Master of Science thesis of Jason A. Tobias presented on June 6, 2007.

APPROVED:

Major Professor, representing Mechanical Engineering

Head of the Department of Mechanical, Industrial and Manufacturing Engineering

Dean of the Graduate School

I understand that my thesis will become part of the permanent collection of Oregon State University libraries. My signature below authorizes release of my thesis to any reader upon request.

Jason Tobias, Author

ACKNOWLEDGEMENTS

The author expresses sincere appreciation to everyone who inspired him to learn, encouraged him to carry on, and listen with open ears during the course of obtaining this degree. The author would like to thank Dr. Vinod Narayanan for giving him a chance to be part of this challenging project, for being a great advisor, but most of all for being a good friend. The author would like to thank Dr. Jim Liburdy and Dr. Murty Kanury for the many great discussions both in and out of class and for the great courses taught (and of course for serving on his thesis defense committee). The author would like to thank Dr. Mike Hartman for representing the Graduate School on his thesis defense committee. The author would like to thank Steve Adams and Brian Jensen for the help with the fabrication of parts and the teaching of basic machining skills vital to completing this research. The author would like to thank his lab mates Vishal Patil, Jeromy Jenks, Dan Krebs, Younghoon Kwak, Greg Mouchka and any one else he forgot for making the lab such a fun place to work. Also, the author can't forget to thank the USME for making Friday nights just a little bit more fun than they should be in graduate school. Finally, the author would like to thank his family Theresa, Toby, and Jeremy Tobias along with a good friend of his Dan Staley for always being there whether he was happy, sad, freaking out, or any other description of the various states of the human mind.

TABLE OF CONTENTS

	<u>Page</u>
1 INTRODUCTION & MOTIVATION.....	1
1.1 Motivation.....	3
2 LITERATURE REVIEW.....	5
2.1 Perturbation of axisymmetric jets flows	5
2.2 Particle Image Velocimetry (PIV)	9
3 EXPERIMENTAL FACILITY.....	11
3.1 General experimental set-up	11
3.2 Data acquisition hardware for acoustic studies.....	16
3.3 PIV data acquisition hardware	17
4 EXPERIMENTAL PROCEDURE	19
4.1 Target mass flow rates for fixed jet conditions.....	19
4.2 Acoustic study to determine collar lengths	20
4.3 PIV study to characterize flow field	21
5 DATA REDUCTION AND ANALYSIS	27
5.1 Sound pressure level and frequency.....	27
5.2 Mass flow rate data reduction	28
5.2.1 Primary mass flow rate	28
5.2.2 Secondary seeded mass flow rate	29
5.3 PIV data reduction	31
5.3.1 Instantaneous velocity field	31

TABLE OF CONTENTS (Continued)

	<u>Page</u>
5.3.2 Mean velocity field	33
5.3.3 Turbulent intensity field.....	34
5.3.4 Mean vorticity fields.....	34
5.3.5 Fluctuating velocity correlation	35
5.3.6 Kinetic energy of the mean flow.....	35
5.3.8 Mean volumetric flow rate.....	36
5.3.9 Generation of whole field image maps	36
5.4 Uncertainty Analysis.....	36
6 RESULTS AND DISCUSSION	41
6.1 Collar length study – Sound pressure level and frequency.....	42
6.2 PIV studies - Centerline data	43
6.3 Whole field results	60
7 CONCLUSIONS.....	70
BIBLIOGRAPHY	72
APPENDIX A: CALIBRATION.....	76
A.1 Calibration of pressure transducers	76
A.2 Calibration of thermocouples.....	78
A.3 Calibration of microphone	80
APPENDIX B: UNCERTAINTY CALCULATIONS	82

TABLE OF CONTENTS (Continued)

	<u>Page</u>
B.1 Uncertainty in mass flow data.....	82
B.1.1 Uncertainty in temperature measurements.....	82
B.1.2 Uncertainty in pressure measurements.....	84
B.1.3 Uncertainty in primary mass flow rate.....	85
B.1.4 Uncertainty in secondary mass flow rate	87
B.1.5 Uncertainty in total mass flow rate	88
B.2 Uncertainty in acoustic data	89
B.3 Uncertainty in PIV data.....	90
B.3.1 Uncertainty in instantaneous velocity	90
B.3.2 Uncertainty in mean velocity	91
B.3.3 Uncertainty in fluctuating velocity.....	92
B.3.4 Uncertainty in vorticity calculations	93
B.3.5 Uncertainty in volumetric flow rate	94
APPENDIX C: PIV DATA FOR THE REYNOLDS NUMBER OF 27000 AND 71000.....	96
C.1 PIV data for the Reynolds number of 27,000.....	96
C.2 PIV data for Reynolds of 71,000.....	103

LIST OF FIGURES

<u>Figure</u>	<u>Page</u>
1.1: Schematic of the acoustically self-excited jet phenomenon.	2
3.1: Schematic of the jet experimental facility.....	12
3.2: Photographs of experimental facility - (a) Inside view of the enclosure, showing plenum and nozzle; (b) coordinate system of figure 3.2a; (c) Outside view of the enclosure, showing the imaging set-up.	14
3.3: Pictures of the nozzle studied – (a) circular pipe jet used for unexcited jet conditions; (b) ASEN nozzle used for excited jet conditions.	16
3.4: Schematic of light sheet optics layout.....	18
4.1: Camera position for leveling of ASEJ.	22
6.1: SPL as a function of L_c	41
6.2: SPL f as a function of L_c	41
6.3: Comparison of streamwise variation of U_c/U_e along the centerline of the jet for the unexcited jet with Hasan and Hussain (1982).	44
6.4: Comparison of streamwise variation of U_c/U_e along the centerline of the jet for first stage ASEJ with Hasan and Hussain (1982).	45
6.5: Comparison of streamwise variation of U_c/U_e along the centerline of the jet for second stage ASEJ with Hasan and Hussain (1982).	46
6.6: Streamwise variation of U_c/U_e along the centerline of the jet.....	47
6.7: Comparison of streamwise variation of u'/U_e along the centerline of the jet for the unexcited free jet with Hasan and Hussain (1982).	50
6.8: Comparison of streamwise variation of u'/U_e along the centerline of the jet for first stage ASEJ with Hasan and Hussain (1982).	51
6.9: Comparison of streamwise variation of u'/U_e along the centerline of the jet for second stage ASEJ with Hasan and Hussain (1982).	52
6.10: Streamwise variation of u'/U_e along the centerline of the jet.	53

LIST OF FIGURES (Continued)

<u>Figure</u>	<u>Page</u>
6.11: Cross-stream variation of v'/U_e along the jet centerline.	56
6.12: Streamwise variation of \dot{Q}/\dot{Q}_e	58
6.13: Whole field streamwise variation of U/U_e - (a) unexcited jet, (b) first stage ASEJ, (c) second stage ASEJ.....	60
6.14: Whole field variation of mean vorticity Ω/Ω_{\max} - (a) unexcited jet, (b) first stage ASEJ, (c) second stage ASEJ.	61
6.15: Whole field streamwise variation of u'/U_e - (a) unexcited jet, (b) first stage ASEJ, (c) second stage ASEJ.....	63
6.16: Whole field streamwise variation of v'/U_e - (a) unexcited jet, (b) first stage ASEJ, (c) second stage ASEJ.....	64
6.17: Whole field variation in fluctuating velocity correlation $\overline{u'v'}/U_e^2$ - (a) unexcited jet, (b) first stage ASEJ, (c) second stage ASEJ.	66
6.18: Whole field variation of mean kinetic energy Q^2/U_e^2 - (a) unexcited jet, (b) first stage ASEJ, (c) second stage ASEJ.	68
6.19: Whole field variation of turbulent kinetic energy q^2/U_e^2 - (a) unexcited jet, (b) first stage ASEJ, (c) second stage ASEJ.	69
A.1: Calibration curve for critical flow meter pressure transducer.....	76
A.2: Calibration curve for the rotameter pressure transducer.....	77
A.3: Calibration curve for the critical flow meter thermocouple.....	78
A.4: Calibration curve for the rotameter thermocouple.....	79
C.1: Whole field streamwise variation of U/U_e - (a) unexcited jet; (b) first stage ASEJ; (c) second stage ASEJ.....	96
C.2: Whole field streamwise variation of Ω/Ω_{\max} - (a) unexcited jet; (b) first stage ASEJ; (c) second stage ASEJ.....	97

LIST OF FIGURES (Continued)

<u>Figure</u>	<u>Page</u>
C.3: Whole field streamwise variation of u'/U_e - (a) unexcited jet; (b) first stage ASEJ; (c) second stage ASEJ.....	98
C.4: Whole field streamwise variation of v'/U_e - (a) unexcited jet; (b) first stage ASEJ; (c) second stage ASEJ.....	99
C.5: Whole field variation in fluctuating velocity correlation $\overline{u'v'}/U_e^2$ - (a) unexcited jet; (b) first stage ASEJ; (c) second stage ASEJ.	100
C.6: Whole field variation of mean flow kinetic energy Q^2/U_e^2 - (a) unexcited jet; (b) first stage ASEJ; (c) second stage ASEJ.	101
C.7: Whole field variation of turbulent kinetic energy q^2/U_e^2 - (a) unexcited jet; (b) first stage ASEJ; (c) second stage ASEJ.	102
C.8: Whole field streamwise variation of U/U_e - (a) unexcited jet; (b) first stage ASEJ; (c) second stage ASEJ.....	103
C.9: Whole field variation of mean vorticity Ω/Ω_{\max} - (a) unexcited jet; (b) first stage ASEJ; (c) second stage ASEJ.	104
C.10: Whole field streamwise variation of u'/U_e - (a) unexcited jet; (b) first stage ASEJ; (c) second stage ASEJ.....	105
C.11: Whole field streamwise variation of v'/U_e - (a) unexcited jet; (b) first stage ASEJ; (c) second stage ASEJ.....	106
C.12: Whole field variation in fluctuating velocity correlation $\overline{u'v'}/U_e^2$ - (a) unexcited jet; (b) first stage ASEJ; (c) second stage ASEJ.	107
C.13: Whole field variation of mean flow kinetic energy Q^2/U_e^2 - (a) unexcited jet; (b) first stage ASEJ; (c) second stage ASEJ.	108
C.14: Whole field variation of turbulent kinetic energy q^2/U_e^2 - (a) unexcited jet; (b) first stage ASEJ; (c) second stage ASEJ.	109

LIST OF TABLES

<u>Table</u>	<u>Page</u>
4.1: Experimental Matrix for Acoustic and PIV Studies	21
4.2: Camera frame and laser timing in PIV studies	26
5.1: The uncertainty in global measurements.	37
5.2: The uncertainty in PIV data	38
6.1. ASEJ collar lengths based on acoustic data for 1st and 2nd stage excitation.	42
6.2: Values of U_e for all jet conditions studied.	48
A.1: Constant coefficient values for microphone calibration curve.....	80
A.2: Calibration data for microphone	81
B.1: Uncertainty values in temperature measurements for $Re = 49,000$	84
B.2: Uncertainty values in pressure measurements for $Re = 49,000$	85

Characterization of the Near-field Flow Structure of an Acoustically Self-excited Jet in a Large Enclosure Using Particle Image Velocimetry (PIV)

1 INTRODUCTION & MOTIVATION

Turbulent jets present an interesting case for investigation due to their significance in many industries and their ongoing role in the growth of humankind's physical understanding of turbulence in general. Turbulent jets have become commonplace in today's technological society in many areas such as propulsion, heat transfer using jet impingement, combustion, or any usually buoyant plume exiting the exhaust of cars, factories, and homes. Visit any library, or better yet Google™ "turbulent jet" and it is easy to see from the plethora of journal articles on the subject that turbulent jets have been a cornerstone of both the experimental and theoretical exploration into the mysteries of turbulence and fluid dynamics for well over 100 years. In particular, during the 1970s, axisymmetric turbulent jets were of great interest to researchers who discovered that large scale orderly structures existed in jet turbulence.

In their pioneering study, Crow and Champagne (1971) set out to show that large scale orderly structures exist in jet turbulence and that these structures could be amplified and controlled by a periodic surging applied at the jet exit. This periodic surging was produced using a loud speaker. Such experiments allowed Crow and Champagne (1971) to present very compelling evidence of the existence of orderly structures in jet turbulence and the possibility of controlling and enhancing that structure via acoustic excitation. In the years following, many more studies were published such as that by Hasan and Hussain (1982) who summarized the different ways in which orderly structures had been artificially induced in jet turbulence by

previous researchers such as by using loud speakers, periodic-ribbon excitation, spark generation, or by fluid injection. More importantly, they characterized the flow field of a device known as the “whistler nozzle” that would produce orderly structure in jet turbulence via self-sustained acoustic excitation.

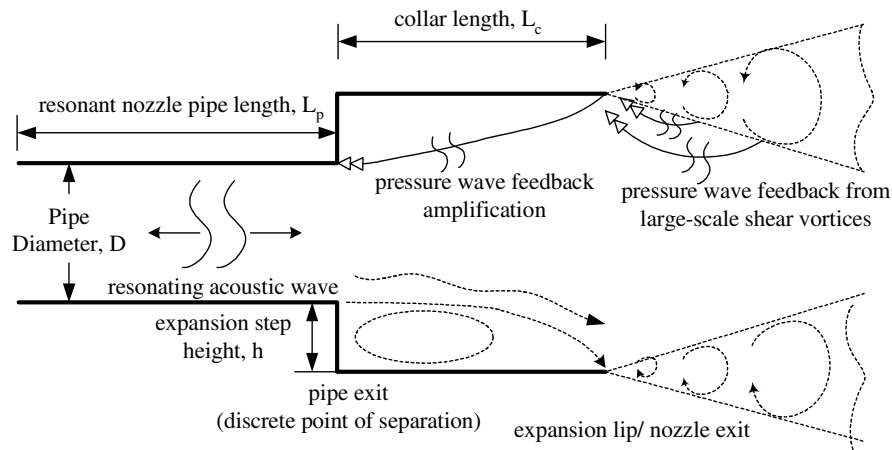


Figure 1.1: Schematic of the acoustically self-excited jet phenomenon.

Hill and Greene (1977) are the first known researchers to study and document the acoustically self-excited jet and coined the term "whistler nozzle", due to the loud pure tone produced by the device. Figure 1.1 shows a schematic of the whistler nozzle. Henceforth, this nozzle will be referred to as the Acoustic Self-Excitation Nozzle (ASEN), and the jet that emanates from it will be called the Acoustically Self-Excited Jet (ASEJ). The two acronyms (i.e. ASEN and ASEJ) were decided upon because it was felt they better describe the physical phenomena of the nozzle compared to the term “whistler” nozzle. The ASEN (see Fig. 1.1) consists of a constant diameter pipe with an axisymmetric sudden expansion at the pipe exit. It has been shown by Hussain

and Hasan (1983) that the whistler excitation is a result of the coupling of two independent resonant mechanisms: organ-pipe resonance of the constant diameter pipe section, and shear layer tone resulting from the shear layer at the pipe exit impinging on the collar lip in an oscillatory fashion. In a qualitative sense, the resonating pipe acts as an energy redistribution device that selectively channels the multi-scale near field turbulent energy into frequencies of a particular jet mode (one of the inherent hydrodynamic instability modes in jet turbulence) thus amplifying the near-field flow structure corresponding to that jet mode. The particular jet mode excited depends on the “stage” of acoustic self-excitation. Here, stage denotes the same as any edge-tone system. This resonance is created by receiving an acoustic (pressure wave) feedback through the expansion (Rockwell (1983)) from the large-scale vortices in the near-field jet. The expansion region plays the role of a feedback amplifier. Hasan and Hussain (1979) were able to derive an empirical correlation to predict the pure-tone frequencies at which an ASEN can induce controlled excitation of a circular jet based on the controlling – the pipe diameter, D , the step height, h , the collar length, L_c , the pipe length, L_p , the stage of excitation, and mode of excitation. The novelty of this jet lies in inducing and sustaining resonance without the help from an external device.

1.1 Motivation

Whereas spatially local information of the ASEN flow field was obtained in the previous studies mentioned above, these measurements were performed using single or multiple arrays of hot wire probes, thereby precluding quantitative visualization of the entire flow field at any instant in time. Such an instantaneous

whole field image could be used to determine the instantaneous vector fields of the ASEN and provide a qualitative picture of the flow structure. The motivation behind this study is to document the near-field flow close to the exit of an ASEJ using whole-field quantitative measurements. Note, that “near-field” in this thesis, refers to downstream locations of less than 10 pipe nozzle diameters. Two-dimensional Particle Image Velocimetry (PIV) measurements were obtained for a steady axisymmetric free jet and both first and second stage ASEJ at three turbulent Reynolds numbers. The flow fields of first and second stage ASEJ are compared with that of the steady axisymmetric free jet.

2 LITERATURE REVIEW

Literature review presented in this chapter covers the two main areas of direct relevance to this thesis. First, a review of the various methods used to modulate the velocity of a turbulent incompressible axisymmetric jet, and the effect of the velocity modulation on such jets is discussed. Second, a short review of the Particle Image Velocimetry (PIV) measurement technique is provided because this is the main measurement technique used in this study.

2.1 Perturbation of axisymmetric jets flows

The modulation of a turbulent axisymmetric jets velocity has been studied extensively over the last thirty years. There have been many methods used to modulate the velocity of axisymmetric jets such as precessing jet nozzles (Wong et al. (2003); Nathan et al. (1998); Schachenmann and Rockwell (1980)) and mechanical pulsing with valves (Dano (2005); Mladin and Zumbrennen (1997); Binder and Favre-Marinet (1973)). However, only the two most relevant methods to work presented in this thesis will be discussed in this literature review, namely the acoustical modulation of a jets velocity via a loud speaker and acoustic self-excitation via an ASEN.

The effect of acoustical modulation has shown promise in attaining some control over the near-field structure in jet turbulence. Amplification or suppression of the root mean square (rms) velocity fluctuations within the jet along with increased entrainment of the surrounding fluid into the jet has been shown. Both the amplification of rms velocity fluctuation within the jet and increased entrainment of surrounding fluid into the jet indicate greater turbulent mixing in the near field of such

acoustically excited jets. Transport processes such as heat and mass transfer can benefit from the control of jet turbulence and increased turbulent mixing. Thus, the effect of acoustically modulating axisymmetric jet velocity has been studied for jet impingement heat transfer.

Early studies involving the acoustic modulation of a jet's velocity were concerned with the documentation of orderly structure in jet turbulence. These studies used a controlled acoustic excitation via a loud speaker in order to amplify orderly structure in jet turbulence above the background noise inherent to such flows. Crow and Champagne (1971), in their pioneering study, documented the effect of a periodic forcing applied via a loud speaker to a turbulent axisymmetric jet issuing into a quiescent environment. They showed that when the jet was forced at the "preferred mode" having a Strouhal number of $St = 0.3$ (based on the jet diameter), a significant increase of up to 32 percent in the surrounding flow entrainment occurred. Also, the rms fluctuating velocity along the centerline of the jet was amplified by approximately 10 percent over the unexcited jet. Zaman and Hussain (1980) concluded that the augmentation of rms velocity fluctuation experienced by an acoustically excited turbulent axisymmetric jet was associated with vortex pairing in the jet. They showed that vortex pairing in circular jets occurred in two distinct modes of excitation: the first being 'the shear layer mode' when $St \approx 0.012$ (based on the initial shear layer momentum thickness) and 'the jet column mode' with $St \approx 0.85$ (based on the jet diameter). More recently, Drobniak and Klajny (2002) revisited the work of Zaman and Hussain (1980) by presenting an experimental stability analysis of a free round jet performed with the use of acoustic excitation. They show remarkable video footage of

vortex shedding from the jet exit for both the jet column and shear layer modes discussed by Zaman and Hussain (1980). Acoustic modulation of a jet's velocity via a loud speaker is prevalent however; it has not been the only method of acoustically exciting an incompressible turbulent axisymmetric jet.

A nozzle known as the “whistler” nozzle (see Fig. 1.1) has been shown to greatly increase turbulent jet mixing rates via a self-sustained acoustic excitation. Hill and Green (1979) detail their discovery of the whistler nozzle showing the entrainment of surrounding fluid into the jet is increased and rms velocity fluctuations in the near-field of the jet are amplified by approximately 10 percent relative to the unexcited jet when the jet is forced at Strouhal number of $St = 0.315$. Hasan and Hussain (1982) characterized the whistler nozzle experimentally for various choices of the controlling parameters: namely, pipe length (L_p), jet diameter (D), collar length (L_c), stage of excitation (i.e. $j = 1, 2, 3$, etc.), acoustic speed (a_o), and mode of excitation (i.e. $n = \frac{1}{2}$ or 1). With their extensive data Hasan and Hussain (1979) were able to generate an empirical correlation to predict the resonance frequencies (f_H) of acoustic self-excitation based on the controlling parameters listed above (see Eq. 2.1).

$$\frac{f_H}{a_o n} \left(L_p + 1.65 \frac{L_c}{j} + 0.7D \right) = 1 \quad (2.1)$$

It was shown in Hussain and Hasan (1983) that the whistler nozzle phenomena results from the coupling of two independent resonance mechanisms: the shear layer tone resulting from the oscillating impingement of the pipe exit shear layer on the collar lip, and organ-pipe resonance of the constant diameter pipe section. Rockwell

(1983) gives a general review of the oscillations of impinging shear layers and the noise produced by them. Extending their work on circular whistler nozzles Husain and Hussain (1999) characterized the flow field of an elliptic whistler nozzle. They show that in the near-field mass entrainment is significantly higher (70 percent) than the unperturbed jet.

Increased turbulent mixing of an acoustically excited jet is expected to enhance both heat and mass transfer. Herman (2000) gives a thorough review of the impact of flow oscillations on convective heat transfer. Several publications on the subject of acoustic excitation applied to jet impingement heat transfer are available (Tianshu and Sullivan (1996); Can and Etemoglu (2003); Hwang and Cho (2003)) however; two are particularly relevant to this thesis. Page et al. (1995) studied the jet impingement heat transfer of a whistler nozzle compared to a unperturbed jet with both jet's exit located three jet diameters above the impingement surface. They showed that the average convective heat transfer coefficient of the impinging whistler nozzle was enhanced by approximately 60 percent compared to the unexcited jet. Cvetinovic et al. (2000) presented a similar study of jet impingement heat transfer of a whistler nozzle relative to that of an unexcited jet. They showed the maximum Nusselt numbers (Nu) of excited and non-excited jets were identical however, the excited jet produced maximum Nu with its jet exit located five diameters from the impinging surface while the non-excited jet had a maximum Nu with its jet exit located at nine diameters from the impinging surface.

2.2 Particle Image Velocimetry (PIV)

Until the early 1990s measurement of fluid velocity has been performed predominately using two measurement techniques, namely hot-wire anemometry and Laser Doppler Anemometry (LDA). A hot-wire anemometer is an instrument that measures the velocity of a moving fluid based on the rate of heat loss to the moving fluid by the sensor. The sensor of a hot-wire anemometer is a metallic resistive temperature detector (RTD). By placing the RTD in one leg of a Wheatstone bridge the resistance across the RTD can be measured. The Resistance-temperature relationship of an RTD is well known so that the temperature of a RTD can be inferred by a resistance measurement. With the temperature of the RTD known the convective heat transfer from the RTD by the moving fluid can be solved. Thus, the velocity of the flow field can be determined using King's Law relating the rate of heat transfer from the sensor to the fluids velocity (Figliola and Beasley (2000)). Hot-wire anemometers are a mainstay in the study of turbulent flows due to their high frequency response (on the order of 10^4 Hz). However, they are intrusive to the flow; hence, a laser based measurement technique was developed.

Laser Doppler Anemometers utilize the Doppler effect to measure the local velocity in a moving fluid (Figliola and Beasley (2000)). By focusing a laser beam to a point in the flow, light is scattered from particles moving with the flow. Thus, the Doppler shift of the light scattered from particles moving with the flow is used to infer the local instantaneous velocity of the moving fluid. Similar to hot-wire anemometers, LDA has a high frequency response (on the order of 10^3 - 10^7 Hz). Also similar to the

drawback of hot-wire anemometry, LDA provides only single-point velocity measurements. Thus Particle Image Velocimetry (PIV) was developed to allow for entire flow fields velocity to be measured at an instance in time in a minimally-intrusive manner.

The Particle Image Velocimetry (PIV) measurement technique has been in development over the last twenty years. Adrian (2005) gives a good general review on the development of PIV as a measurement technique, major milestones overcome, and the current state of the art. To this author's knowledge, Adrian (1984) was the first to describe PIV as a measurement technique. Modern PIV units consist of three main components; a digital camera (usually a CCD), a pulsed laser (usually dual-cavity doubly-pulsed Nd:YAG), and beam collimating optics to produce a sheet of laser light. The basics of the PIV measurement technique are as follows. First, seed particles following the flow field are illuminated with the sheet of laser light in two consecutive, short bursts. Laser light reflected and scattered by the seeds is captured by the camera in pairs of images with known times between image pairs. The image pairs are then divided into interrogation windows of known size. Within each interrogation window the average displacement of particles in the interrogation window is calculated using cross-correlation. Keane and Adrian (1992) give an in depth review of cross-correlation techniques applied to PIV. With the displacement of seed particles measured in each interrogation window and the known time interval between image pairs, a velocity vector can be determined for each interrogation window. Raffel et al. (1998) give a good general review of all aspects of the PIV measurement technique.

3 EXPERIMENTAL FACILITY

In this chapter, the experimental facility for jet studies and the nozzle geometry are discussed in detail. An acoustic study was performed to determine the collar lengths (L_c) that resulted in a first and second stage acoustically self excited jet (ASEJ), respectively. Therefore the data acquisition hardware used to complete the acoustic measurements is discussed next. Concluding this chapter is a detailed discussion of the data acquisition hardware used to obtain Particle Image Velocimetry (PIV) measurements.

3.1 General experimental set-up

Jet studies were conducted in the experimental facility shown as a schematic in Fig. 3.1. Compressed air was supplied by the industrial compressor located in the basement of Rogers Hall at Oregon State University. Air was first passed through a five-micron filter and regulated to a typical pressure of 690 kPa gage (100 psig) prior to flowing into the first 320-liter settling tank (settling tank 1 in Fig. 3.1) located in the laboratory. After exiting the first settling tank, the air flow was separated into two paths. Most of the air flowed into a second 320-liter settling tank (settling tank 2 in Fig. 3.1) through a 0.03-micron-element filter and a precision pressure regulator (ControlAir Inc., type 700). The remaining air was regulated to a pressure of 207 kPa gauge (30 psi) and routed to the seeder in order to produce the required seeding particles for obtaining PIV measurements.

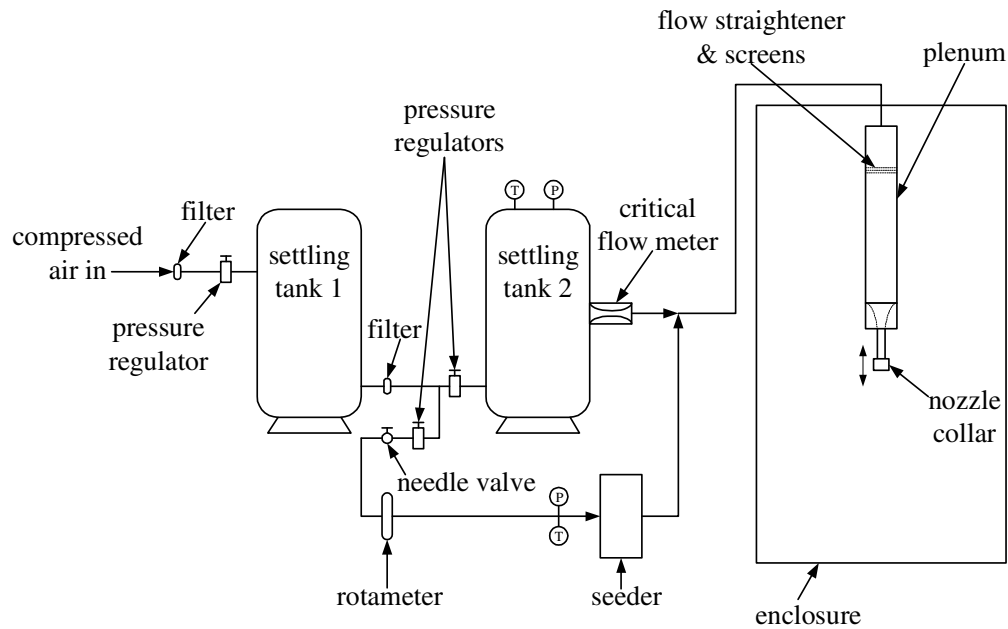


Figure 3.1: Schematic of the jet experimental facility.

Mass flow rate of air exiting the second settling tank was measured with a calibrated critical flow meter (Flow-Dyne Engineering, Inc., N080125-SPT). The critical flow meter had a throat diameter of 3.175 mm (0.125 in). In order to obtain mass flow rate from the critical flow meter, the stagnation pressure and temperature had to be measured in the second settling tank. Stagnation pressure was measured with a calibrated variable reluctance differential pressure transducer (Validyne Engineering, DP15). Stagnation pressure was acquired from the transducer with a laptop computer (Dell, Inspiron 5150) running a LabVIEW® Virtual Instrument (VI) that communicated with a universal serial bus (USB) data acquisition card (National Instruments, USB-6009). Stagnation temperature was measured with a calibrated thermocouple (Omega Engineering, Inc., K type) and digital thermocouple readout (Omega Engineering, Inc., HH23).

Mass flow rate of air routed to the seeder was measured using a correlated rotameter (Gilmont, GF-1560) located directly upstream from the seeder. To account for the compressibility of air, the working pressure and temperature of the rotameter had to be measured in order to use the correction factor supplied with the rotameter (see chapter 5 for more details). For this configuration the working pressure and temperature of the rotameter was the pressure and temperature prior to the rotameter. Working pressure was measured with a calibrated variable reluctance differential pressure transducer (Validyne Engineering, DP15). Stagnation pressure was acquired from the transducer with a laptop computer (Dell, Inspiron 5150) running a LabVIEW® Virtual Instrument (VI) communicating with a universal serial bus (USB) data acquisition card (National Instruments, USB-6009). Working temperature was measured with a calibrated thermocouple (Omega Engineering, Inc., K type) and digital thermocouple readout (Omega Engineering, Inc., HH23).

Seed particles for PIV measurements were generated using an air-assist Laskin atomizer (Raffel et al. (1998)). The Laskin atomizer used in this study had a diameter of 1 mm and was submerged in a reservoir of olive oil which was the working fluid for atomization. This atomizer produced an oil aerosol with an average particle size of 11 μm determined from the average diameter of seeds imaged with a micro lens. The decision to use olive oil as the working fluid and acquire a Laskin atomizer with a 1 mm diameter was based on the previous experience of a colleague seeding air jet flows (Dano (2005)). Concentration of seed particles was controlled by adjusting a needle valve located upstream of the Laskin atomizer.

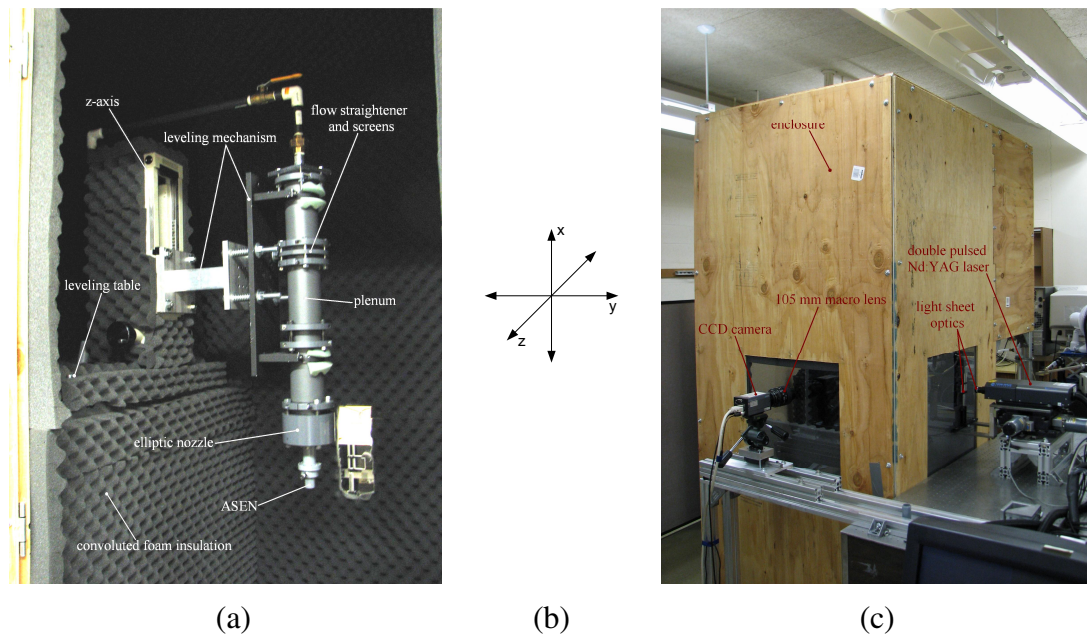


Figure 3.2: Photographs of experimental facility - (a) Inside view of the enclosure, showing plenum and nozzle; (b) coordinate system of figure 3.2a; (c) Outside view of the enclosure, showing the imaging set-up.

Experiments were performed in the enclosure shown in Fig. 3.2a & c. Seeding of the entire flow field for PIV measurements was made possible by the enclosure. Both the jet and surrounding ambient air were seeded prior to measurements to prevent velocity biasing. The enclosure test section was approximately 1.01 m wide, 0.86 m long and 2.13 m tall. The jet was positioned 0.33 m (i.e. 26 jet diameters) away from the closest wall to the nozzle center, and impinged on the enclosure floor 1.02 m (i.e. 80 jet diameters) downstream at its lowest position. Convoluted foam insulation was used to line the inner walls of the enclosure to reduce the effect of acoustic reflections from the chamber inner walls.

Within the enclosure (see Fig. 3.2a), the acoustic self-excitation nozzle (ASEN) to be studied was mounted at the end of a plenum. The 53.3-cm-long plenum was fabricated using CPVC and had an inner diameter of 5.1 cm. A flow straightening element along with three fine mesh screens were used to reduce the magnitude of turbulence intensity at the pipe exit. The flow straightening element and screens were located approximately 36 cm upstream from the pipe exit within the plenum. An elliptic nozzle with an area contraction ratio of 16:1 constituted the final section of the plenum. The ASEN was mounted directly to the end of the elliptic nozzle. The test section (i.e. plenum and ASEN) was attached to a z-axis using a leveling mechanism allowing for the test section to be tilted about both the x and y axes. Approximately 20 cm of vertical movement was possible with the z-axis. A leveling table was used to mount the z-axis and test section to the enclosure in order to ensure perpendicularity of the z-axis. With the z-axis leveled by this table, it was possible to level the test section relative to the PIV camera and laser (see Fig. 3.2c).

Shown in Figs. 3.3a & b are pictures of the circular pipe jet used for the unexcited case and ASEN, respectively. The ASEN was fabricated using CPVC and consists of a constant inner diameter (1.27 cm) pipe section that is 10.16 cm (i.e. 8 nozzle diameters) long. The outer diameter of the ASEN at the pipe exit is 2.22 cm resulting in a step height (i.e. pipe wall thickness) of 0.476 cm. To induce an acoustically self excited jet (ASEJ) (see Fig. 3.3b), collars are slid around the outer diameter of the ASEN to a collar length that results in an acoustic self excitation. The unexcited jet (see Fig. 3.3a) is simply the ASEN without any collar slid around the pipe exit.

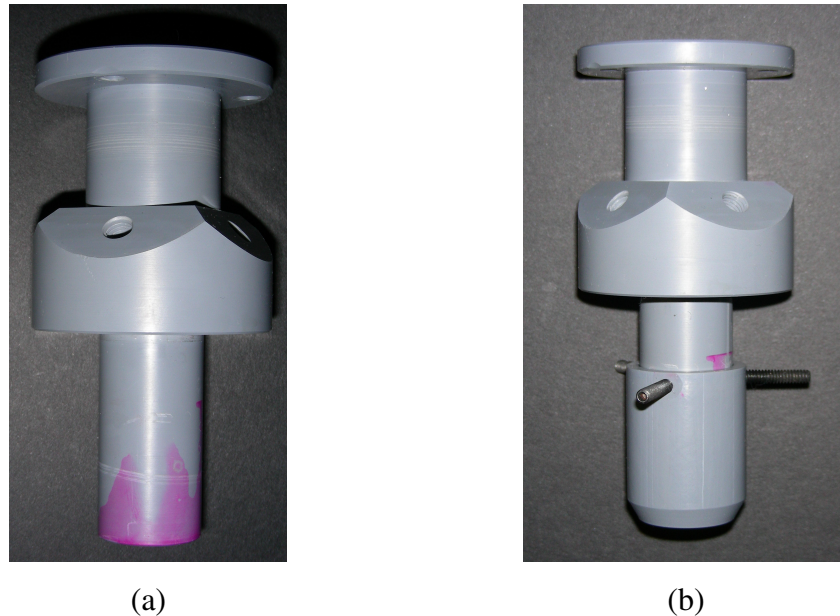


Figure 3.3: Pictures of the nozzle studied – (a) circular pipe jet used for unexcited jet conditions; (b) ASEN nozzle used for excited jet conditions.

3.2 Data acquisition hardware for acoustic studies

An acoustic study was performed to determine the collar length (L_c) that resulted in a first and second stage acoustically self excited jet (ASEJ). The collar length for first and second stage ASEJ was selected based on the extension at which the overall sound pressure level reached a peak value relative to the inherent noise associated with the unexcited jet. Acoustic data were obtained using a calibrated studio condenser microphone (Marshall Electronics, MXL 603s) with a frequency range of 30 – 20,000 Hz. The condenser microphone was calibrated against an integrating sound level meter (Ono Sokki, LA-2111). Pure-tone sound for calibration was provided by a synthesized function generator (Tectronix, AFG2020). Amplification of the signal produced by the function generator was achieved with a

250 W car audio amplifier (Kenwood, KAC5201), supplying power to a 240 W Pioneer car audio speaker of 15.2 cm x 20.3 cm dimension.

3.3 PIV data acquisition hardware

PIV data was acquired with a stock digital PIV system (Dantec Dynamics Ltd.). The digital PIV system consisted of a dedicated data acquisition processor (Dantec Dynamics Ltd., FlowMap™ System Hub), a 12-bit, 1344 x 1024 pixel array CCD camera (Hamamatsu Photonics, Hi Sense MKII), and a double-pulse Nd:YAG laser (New Wave™ Research, Solo PIV-III). Communication with both the camera and the laser along with the synchronization of the camera to the laser was achieved using the FlowMap™ System Hub. The FlowMap™ System Hub had a 1 GB input buffer that permitted continuous acquisition of 250 image pairs at a resolution of 1344 by 1024 CCD pixels.

Image pairs were recorded with the CCD camera. A standard macro lens (Nikon™, 105mm f/2.8 Micro-Nikkor) was used to capture image pairs. The CCD camera was located approximately 51 cm from the axis of the jet as measured from the end of the camera lens to the jet axis. With the camera in position the average field of view was 4.66 cm by 3.54 cm in the cross-stream (radial) and streamwise directions, respectively.

Illumination of the oil aerosol within the flow field was achieved with the double-pulse Nd:YAG laser. In order to illuminate a plane within the flow field a sheet of laser light was required. The laser sheet was produced using two cylindrical lenses in series shown as a schematic in Fig. 3.4. The first lens was a 12.5 mm diverging lens

that expanded the 3.5 mm diameter laser beam to a 3.5 mm thick sheet of laser light in the vertical direction. The second lens was a 500 mm converging lens placed orthogonal to the first this lens focused the light sheet to approximately 1 mm in thickness at the test section that was located 500 mm from the second lens.

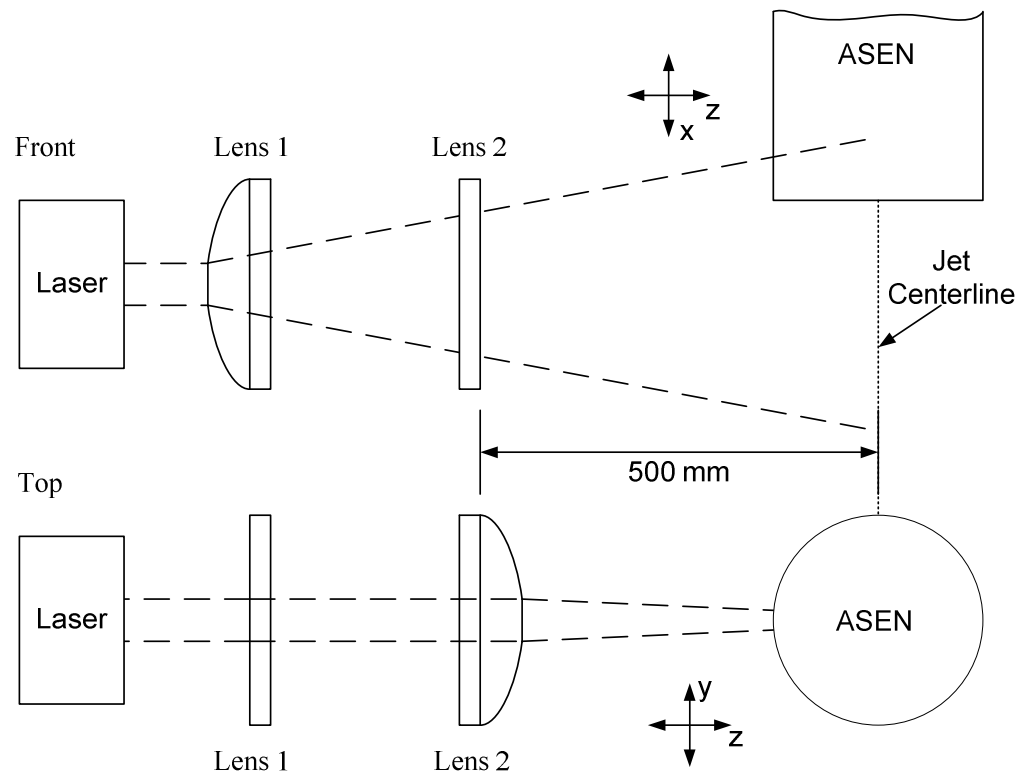


Figure 3.4: Schematic of light sheet optics layout.

4 EXPERIMENTAL PROCEDURE

In this chapter, the experimental procedures developed to acquire data for both the acoustic and PIV studies presented in this thesis are discussed in detail. Three turbulent exit Reynolds numbers of the unexcited jet, first and second stage ASEJ, corresponding to 27,000, 49,000, and 71,000 were investigated for both studies. The Reynolds numbers reported are based on the diameter of the jet exit (12.7 mm) and the average mass flow rate of each case recorded. The chapter begins with a discussion of how nominal flow conditions are ensured and monitored. Next, the experimental procedure used to collect acoustic data is discussed. Finally, the experimental procedure developed to acquire two-dimensional PIV data on a single plane passing through the axis of the ASEJ and unexcited jet is discussed.

4.1 Target mass flow rates for fixed jet conditions

Preliminary observations indicated that pressure in the second settling tank cycled at a low frequency with the duty cycle of the compressor. In the worst case of the largest mass flow rate corresponding to Re of 71,000, the pressure in the second settling tank varied between 627 kPa and 648 kPa (91 psia and 94 psia) over a time interval of approximately 10 minutes. Because of the fluctuating pressure, both acoustic and PIV data were collected at jet conditions fixed by target mass flow rates. The target mass flow rates were 4.9, 8.7, and 12.7 g/s for jet Reynolds numbers of 27,000, 49,000 and 71,000, respectively. The acquisition of data at target mass flow rates was achieved by having the mass flow rate monitored continuously. When the mass flow rate was within ± 0.0625 g/s (0.5 percent of the largest target flow rate), an

indicator was initiated and data were collected. These fluctuations in pressure have a very small frequency (in $1.6(10^{-3})$ cycles per second) when compared to any frequency scales associated with the turbulent flow or acoustic perturbation, which are typically in the order of several hundred cycles per second (Hz). Therefore, by using this target mass flow rate procedure, the effect of the pressure fluctuations on the turbulent jet flow field is expected to be minimal.

4.2 Acoustic study to determine collar lengths

Hasan and Hussain (1983) showed that the loud pure tone associated with the first and second stage excitations of an ASEN occur within a band of collar lengths (L_c). When the collar is extended beyond the nozzle pipe exit, there is initially no significant increase in the noise produced over that of the free jet. Then, abruptly, a loud pure tone is induced. With a continuous increase in L_c beyond the initial point of excitation, the tone increases slightly in intensity, reaches a local maximum, then begins to decrease slightly in intensity until the tone abruptly becomes inaudible. This represents the first stage of excitation. Further extension of L_c would similarly result in a second pure tone local maximum, indicative of the second stage.

To determine L_c for first and second stage ASEJ, an acoustic study was performed. Overall sound pressure levels and frequency as a function of L_c for each of the cases studied were recorded at a fixed position relative to the jet exit. The fixed position chosen was approximately five nozzle diameters downstream of the jet exit and twenty nozzle diameters in the radial direction from the centerline of the jet. Since only the relative difference in sound pressure level above that of the free jet was

desired, the spatial variation of the acoustic signal within the enclosure was not critical. However, the microphone was kept fixed at this location downstream of the nozzle exit for the entire duration of the experiment to eliminate the expected spatial dependence of the acoustic signal being measured. To ensure that this relative distance remained constant between the unexcited jet and the ASEJ, the ASEN was raised using the z-axis an equivalent amount to each L_c recorded. The voltage acquired from the microphone was amplified and recorded using a USB data acquisition card and a LabVIEW Virtual Instrument (VI). To ensure that the results obtained from the collar length study were valid for the PIV studies, the acoustic data were collected with the flow seeded as it would be for PIV measurement.

As a base case, the sound pressure level of the free jet was first recorded then L_c was increased until the first sign of excitation was sensed. The sound pressure level at this position was recorded, along with L_c . The collar length was then extended in 1-mm increments and sound pressure level was recorded at each increment until the pure tone was no longer detected. At each L_c , seven sets at 32,768 samples of the voltage signal were recorded at 48 kHz by the microphone. The sampling frequency of 48 kHz was chosen to ensure the Nyquist criterion was met (Figliola and Beasley (2000)).

Table 4.1: Experimental Matrix for Acoustic and PIV Studies

Re = 27,000	Unexcited jet	First stage ASEJ	Second stage ASEJ
Re = 49,000			
Re = 71,000			

4.3 PIV study to characterize flow field

The goal of the PIV study was to characterize the near-field flow structure of the unexcited jet compared with both first and second stage ASEJ for the three jet conditions shown in Table 4.1. This was accomplished by acquiring two-dimensional PIV data on a single plane passing through the axis of symmetry of each jet. Recall that, on average, the field of view imaged by the CCD camera was 4.66 cm by 3.54 cm in the cross-stream and streamwise direction, respectively. Thus, only 3.54 cm (3 diameters) of a jets flow in the streamwise direction could be studied if only one fixed viewing station was used to acquire PIV measurements. Therefore, the ASEN was raised via the z-axis (see fig. 3.2a) to record five consecutive viewing stations in the streamwise direction, allowing for approximately 14 continuous diameters of each jets flow to be studied. In order to ensure, to a good degree of certainty, that each jets centerline was fixed relative to the CCD camera and laser as the ASEN was raised, a robust leveling procedure was developed.

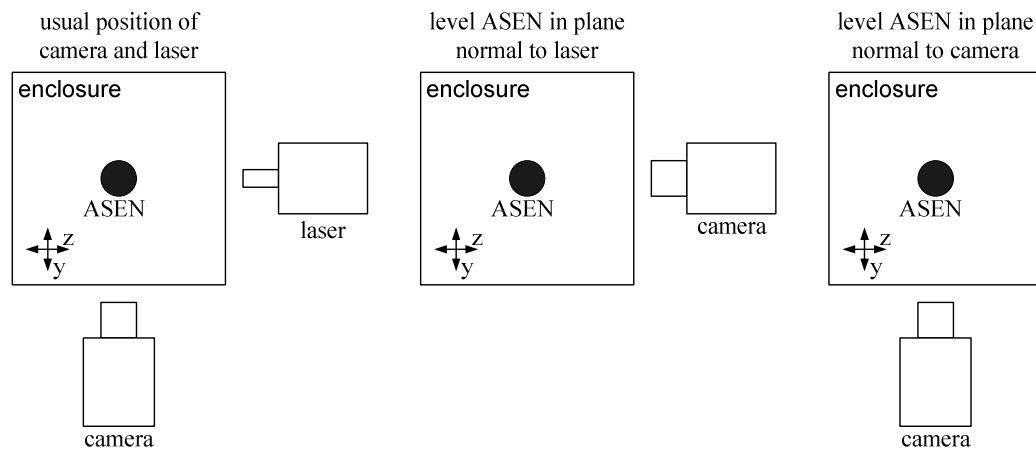


Figure 4.1: Camera position for leveling of ASEJ.

The leveling procedure is depicted schematically in Fig. 4.1 and required the ASEN to be leveled optically in both the plane normal to the camera and the plane normal to the laser. By leveling the ASEN in both planes, the ASEN axis of symmetry was fixed relative to both the laser and camera as the ASEN was raised. Since the camera was to be used to optically level the ASEN, the ASEN was leveled in the plane normal to the laser first so the camera only had to be moved once. Leveling of the CCD camera was achieved by using the two bubble levels of a standard tripod head upon which the camera was mounted. Next, a high-tolerance stainless steel location pin having a diameter of 12.7 mm was inserted into the exit of the jet. The edge of the pin was located in the camera images, thereby allowing for the ASEN to be leveled optically in the plane normal to the laser. Contrast between black and white pixels in the CCD camera was maximized while imaging the location pin by eliminating the laboratory lights and using a flashlight to reflect light off a white screen placed behind the ASEN. Once the jet was leveled in the plane normal to the laser, the camera was returned to its original position and the whole procedure was repeated in order to level the ASEN in the plane normal to the camera.

With the ASEN leveled in both the plane normal to the camera and the plane normal to the laser, the ASEN axis of symmetry was positioned approximately at the middle pixel of the CCD camera optically. This was accomplished by measuring the width of the location pin lodged in the exit of the ASEN with the camera in CCD pixels. Again, contrast between white and black pixels in the images of the location pin was maximized by the white screen technique previously discussed. With the width of the location pin in pixels known, the pixel corresponding to the middle of the

CCD chip could be placed to a fairly good certainty (within 4 CCD pixels) on the centerline of the location pin by translating the camera from side to side on a linear traverse. The pixel location corresponding to the ASEN axis was recorded for each case to ensure consistency between cases and the reduction of data later on.

Once the ASEN was leveled and the camera was positioned, the laser light sheet was positioned so that it was perpendicular and coincident to the ASEN axis of symmetry. The light sheet was made perpendicular to the ASEN axis of symmetry by adjusting the first cylindrical lens (see Fig. 3.4 lens 1). Next, the light sheet was placed coincident to the ASEN axis of symmetry by translating the laser and light sheet optics via a xy traversing stage. Finally, the second cylindrical lens (see Fig. 3.4 lens 2) was placed 500 mm away from the ASEN axis of symmetry with the xy traversing stage. Recall, that the second cylindrical lens had a focal length 500 mm. Thus, by placing the second cylindrical lens 500 mm away from the ASEN axis of symmetry the light sheet thickness was focused to approximately 1 mm at the ASEN axis of symmetry.

With the mechanical set up the ASEN complete, the PIV measurement was set up for the jet condition being recorded. Set up of the PIV measurement required the ASEN to be operated at the jet condition being recorded. Thus, air flow to the ASEN was initiated; seed particles were introduced by the Laskin nozzle upstream of the plenum; and the total mass flow rate of air was set to the target mass flow rate defining the jet condition being recorded. Next, the CCD camera was focused on seed particles in the plane illuminated by the Nd:YAG laser. With the camera focused, air flow to

the ASEN was stopped in order to determine the actual dimensions of the field of view imaged by the camera.

Actual dimensions of the field of view imaged by the camera were determined by inserting the location pin used for leveling in the exit of the ASEN and measuring the diameter of the pin in CCD pixels. The CCD camera had a known pixel pitch of $6.45 \mu\text{m}/\text{pixel}$ square and the location pin had a diameter of 12.7 mm. Thus, a constant scale factor (S) for converting from photo detector array dimensions to actual image dimension was found as

$$S = \frac{12.7 \text{ mm}}{6.45(10^{-3}) \left(\frac{\text{mm}}{\text{pixel}} \right) D_{\text{pixels}}} \quad (4.1)$$

where, D_{pixels} was the diameter of the pin measured in CCD pixels. With S known, the actual dimensions of the field of view imaged by the camera were determined by multiplying the number of pixels (i.e. 1344 pixels by 1024 pixels) in the camera array by the pixel pitch ($6.45(10^{-3}) \text{ mm}/\text{pixel}$) and S. As was mentioned before, the actual dimensions of field of view imaged by the camera in this study was on average 4.66 cm by 3.54 cm in the cross stream and streamwise direction, respectively.

With the field of view calibrated, PIV data were collected for the jet condition being recorded. The first step in PIV data acquisition was to introduce seeds upstream of the jet test section with the Laskin atomizer. After some time the entire enclosure filled with seed particles and uniform seeding density in PIV images was insured by capturing images of the flow field with the camera. With the flow seeded the cross-correlation used to measure average particle displacement within a single interrogation

window was optimized. A detailed discussion of the cross-correlation used and the validation of instantaneous velocity maps are discussed in Chapter 5. With the cross-correlation optimized to produce validated instantaneous velocity maps, actual data acquisition was commenced. For each jet condition (see Table 4.1), 750 pairs of images were collected at five viewing stations for a combined field of view of 4.66 cm by 17.7 cm (3.7 by 13.9 jet diameters) in the cross-stream and streamwise directions, respectively. The number of image pairs was selected based on preliminary experiments studying the effect of number of instantaneous vector maps necessary to create a representative mean flow field map. These 750 image pairs had to be captured in three separate runs because of the limitation of the buffer size in the FlowMap™ system hub. The first 250 images were collected continuously while the following two sets of 250 images were collected in 25 sets of 10 images pairs. The time between image pairs and pairs of images was kept fixed for each jet condition as shown in Table 4.2. For the last two sets of PIV data collected, the time between each of the 25 sets of 10 image pairs was randomly selected.

Table 4.2: Camera frame and laser timing in PIV studies

Jet Condition	Δt image pair	Δt pairs of images
Re = 27,000	3.5 μ s	250 ms
Re = 49,000	1.5 μ s	250 ms
Re = 71,000	1.5 μ s	250 ms

5 DATA REDUCTION AND ANALYSIS

In this chapter, the methods of data reduction and analysis performed in part of this study are discussed. Following the discussion of data reduction and analysis, a brief overview of the associated uncertainty in the data is presented. The MatLab® programs used for data reduction and analysis along with a detailed description of the uncertainty analysis are provided in the appendices.

5.1 Sound pressure level and frequency

Sound pressure level and frequency data were obtained by the method described in chapter three. Seven sets of the AC voltage signal transmitted by the microphone was sampled at 48 kHz for 0.68 s (i.e. 32,768 samples were collected) by a dedicated computer running a labVIEW® virtual instrument (VI). The labVIEW® VI reduced the seven sets of data into power spectrums. Power spectrums were then fed into MatLab® running a script that extracted the peak rms voltage for each of the seven sets of data along with the frequency at which that peak voltage was centered. The seven peak rms voltages and associated frequencies were then averaged to determine an average peak rms voltage and frequency for each collar position recorded. With the average peak rms voltage and frequency in hand the microphone calibration curve was used to determine the overall sound pressure level (dB) for each collar position recorded. The calibration curve for the microphone used to measure overall sound pressure level along with the constant coefficients for that curve are located in appendix A.

5.2 Mass flow rate data reduction

As was discussed in chapter three, the jet flow studied was a combination of primary and secondary streams of air. Primary air flow to the jet was measured using a critical flow meter. Secondary air flow to the jet for PIV seeding was measured using a rotameter. Both measurement devices required temperature and pressure measurements of their respective flows to account for the compressibility of air and obtain a true mass flow rate.

5.2.1 Primary mass flow rate

Mass flow rate in kg/s of primary air flow to the jet was calculated using a relationship supplied by the critical flow meter manufacturer (Flow-Dyne Engineering, Inc.) with an added unit conversion to SI units,

$$\dot{m}_{SF} = K_{SF} \left(\frac{P_{SF}}{\sqrt{T_{SF}}} \right) \left(\frac{0.4536 \text{ kg}}{1 \text{ lbm}} \right) \quad (5.1)$$

where P_{SF} is the stagnation pressure in psia, T_{SF} is the stagnation temperature in $^{\circ}\text{R}$, and K_{SF} is the calibration coefficient in $\text{lbm}^{\circ}\text{R}^{1/2}/\text{psia}^*s$ supplied with the critical flow meter. The calibration coefficient K_{SF} depended on P_{SF} as

$$K_{SF} = a + bP_{SF} + \frac{c}{\sqrt{P_{SF}}} \quad (5.2)$$

where a , b and c are constant coefficients supplied with the curve fit by the manufacturer. Both the stagnation pressure and temperature were measured upstream of the critical flow meter in the second settling tank (see Fig. 3.1). Stagnation pressure and temperature were obtained by sampling the voltage from their respective

transducers with a LabVIEW® VI. The LabVIEW® VI converted the voltage acquired from the respective transducers using calibration curves. The calibration curve for the pressure transducer used to measure P_{SF} was

$$P_{SF} = 8.0V_{PSF} + P_{atm} \text{ (psia)} \quad (5.3)$$

where V_{PSF} was the voltage of the pressure transducer in V used to measure P_{SF} and P_{atm} was atmospheric pressure in psia. The atmospheric pressure, P_{atm} (in psia) was read into the LabVIEW® program during experimentation. The calibration curve for the thermocouple used to measure T_{SF} along with a unit conversion from degrees Celsius to degrees Rankin was

$$T_{SF} = 1.8((0.9984V_{TSF} - 0.1313)(^{\circ}\text{C}) + 273.15)(^{\circ}\text{R}) \quad (5.4)$$

where V_{TSF} was the voltage of the thermocouple in V used to measure T_{SF} .

5.2.2 Secondary seeded mass flow rate

Mass flow rate in kg/s of secondary seeded air to the jet was calculated using a relationship supplied by the rotameter manufacturer (Gilmont) with an added unit conversion to SI units.

$$\dot{m}_R = \dot{Q}_{RS} \left(\frac{\text{L}}{\text{min}} \right) \rho \left(\frac{\text{kg}}{\text{m}^3} \right) \left[\left(\frac{P_R \text{ (Hgmm)}}{760 \text{ (Hgmm)}} \right) \left(\frac{530 \text{ (}^{\circ}\text{R)}}{T_R \text{ (}^{\circ}\text{R)}} \right) \right]^{\frac{1}{2}} \left(\frac{\text{1m}^3}{1000\text{L}} \right) \left(\frac{\text{1min}}{60\text{s}} \right) \quad (5.5)$$

In Eq. 5.5 the term in square brackets was a correction factor to account for the compressibility of air. The working pressure (P_R) in mm of Hg and working temperature (T_R) in $^{\circ}\text{R}$ of the rotameter were measured directly downstream of the rotameter. Working pressure and temperature were obtained by sampling the voltage

from their respective transducers with a LabVIEW® VI. The calibration curve used for the pressure transducer measuring P_R was

$$P_R = (5.0119V_{PR} + P_{atm}(\text{psia})) \left(\frac{51.71 \text{ Hgmm}}{1 \text{ psia}} \right) \quad (5.6)$$

where V_{PR} was the voltage of the pressure transducer in V measuring P_R and P_{atm} was atmospheric pressure in psia. The calibration curve for the thermocouple used to measure T_R was

$$T_R = 1.8 \left[(0.9944V_{TR} - 0.0911) (^{\circ}\text{C}) + 273.15 \right] (^{\circ}\text{R}) \quad (5.7)$$

where V_{TR} was the voltage of the thermocouple in V measuring T_R . To convert from volumetric to mass flow rate the working density ρ in kg/s of the seeder flow was calculated using the measurements of P_R and T_R and the ideal gas law

$$\rho = \frac{P_R(\text{psia}) \left(\frac{6.89 \text{ kPa}}{1 \text{ psia}} \right)}{R_{air} \left(\frac{\text{kPa} \cdot \text{m}^3}{\text{kg} \cdot \text{K}} \right) \left(\left(\frac{1}{1.8} \right) T_R \right) (\text{K})} \quad (5.8)$$

where the gas constant of air (R_{air}) was taken to be $0.287 \text{ kPa} \cdot \text{m}^3 / \text{kg} \cdot \text{K}$. In Eq. 5.5 \dot{Q}_{RS} was the volumetric flow rate in L/min of air at the standard calibration conditions of the rotameter. The standard condition of the rotameter was atmospheric pressure (1 atm) and room temperature ($21 \text{ }^{\circ}\text{C}$). The volumetric flow rate of air at the standard calibration condition of the rotameter was determined by reading the scale value of the rotameter. Rotameter scale reading was converted to volumetric flow rate using the table provided by the manufacturer.

5.3 PIV data reduction

PIV data reduction was largely performed using the FlowManager™ software and MatLab™ programs. Initial data reduction of raw image maps to instantaneous velocity fields and the calculation of mean velocity fields, turbulent intensity fields, vorticity fields, and fluctuating velocity fields from the instantaneous data were performed using FlowManager™. MatLab™ programs were used to calculate volumetric flow rate, turbulent kinetic energy, mean kinetic energy, and Reynolds stress. This section highlights the details of the PIV data reduction.

5.3.1 Instantaneous velocity field

The FlowMap™ System Hub running the FlowManager™ software was used to process two sequential image maps acquired by the CCD camera into instantaneous velocity vector maps. The two sequential image maps were subdivided into a number of so-called interrogation windows. The PIV measurement was based on measuring the average displacement of the particles in an interrogation window between the first and second image maps. Average displacement of particles in an interrogation window was determined using a Fast Fourier Transform (FFT) spatial cross-correlation. The spatial cross-correlation produced many cross-correlation peaks within an interrogation window. A high cross-correlation peak was produced when many of the particles in the first PIV image matched up with their corresponding spatially shifted partners in the second PIV image. Small cross-correlation peaks were produced when individual particles in the first PIV image matched up with other individual particles in the second PIV image. The tallest cross-correlation peak in an interrogation window

was taken to be the true correlation. The location of the tallest cross-correlation peak in an interrogation window corresponds directly to the average displacement of particles within that interrogation window (Dantec Dynamics (2000)). Thus, by dividing the average displacement of particles in an interrogation window by the user input time between laser pulses (see. Table 4.2), a velocity vector for that interrogation window was calculated. Whole field instantaneous vector maps were produced by calculating velocity vectors for all the interrogation windows of two sequential image maps.

In this study, an adaptive spatial cross-correlation was used to process two sequential image maps acquired into instantaneous velocity fields. Adaptive cross-correlation started with interrogation windows of 32 by 64 pixels in the cross-stream and streamwise directions, respectively. One refinement step was used resulting in a final interrogation window size of 16 by 32 pixels in the cross-stream and streamwise directions, respectively. Rectangular interrogation windows with 32 pixels in the streamwise direction were used to increase the dynamic range of the velocity measurement in the streamwise direction (direction of the mean flow).

Measurements performed using PIV are prone to a zero bias in velocity measurements due to the loss of pairs at the edge of an interrogation window (i.e. seed particle travels out of interrogation window between images 1 and 2). The effect of lost pairs can be reduced by using a window function to weigh signal intensities in the center of an interrogation window greater than those intensities at the edge of a window. In the present experiments, a Gaussian window function was used in the

adaptive correlation. The k factor is a scalar weighting variable; in this case k equal to 1 effectively reduces the interrogation window size by 29 percent. An obvious downfall in using window functions is the loss of data at the edge of an interrogation window. However, this data can be and was recovered by overlapping interrogation windows. In the current experiments, the interrogation windows were overlapped by 50 percent.

Because FFT processing is used for spatial cross-correlation, PIV measurements will always produce instantaneous velocity vector maps whether the input is meaningful or not. Therefore, all PIV data must be validated. A cross-correlation peak validation was used in the adaptive correlation. Dantec Dynamics (2000) recommended that the tallest cross-correlation peak produced in an interrogation window be at least 1.2 times taller than the second tallest cross-correlation peak produced in that same interrogation window, and that the tallest cross-correlation peak in the interrogation window have a peak width greater than 3 pixels. Therefore, the peak validation used in the adaptive correlation insured the recommendations of Dantec Dynamics (2000) regarding cross-correlation peaks were met.

5.3.2 Mean velocity field

Mean velocity at a given (i,j) location in the flow field was calculated using data points from the 750 instantaneous velocity fields acquired at that same location ij . Here, i and j refer to index in jet downstream direction and radial (cross-stream) direction, respectively. Mean velocity fields were calculated in FlowManager™ using

$$U_{ij} = \frac{1}{N} \sum_{k=1}^{k=N} u_{ij,k} \quad (5.9)$$

$$V_{ij} = \frac{1}{N} \sum_{k=1}^{k=N} v_{ij,k} \quad (5.10)$$

where N represents the number of samples in the data set, $u_{ij,k}$ is the stream-wise component of instantaneous velocity, and $v_{ij,k}$ is the radial component of instantaneous velocity.

5.3.3 Turbulent intensity field

At a given (i,j) location in the flow field turbulent intensity was calculated using data points from the 750 instantaneous velocity fields acquired at that location.

Using FlowManager™ turbulent intensity fields were generated using the relations

$$v'_{ij} = \sqrt{\frac{1}{N-1} \sum_{k=1}^{k=N} (v_{ij,k} - V_{ij,k})^2} \quad (5.11)$$

$$u'_{ij} = \sqrt{\frac{1}{N-1} \sum_{k=1}^{k=N} (u_{ij,k} - U_{ij,k})^2} \quad (5.12)$$

5.3.4 Mean vorticity fields

Mean vorticity at a given (i,j) location normal to the plane imaged was calculated using FlowManager™ as

$$\Omega_{\theta}(i,j) = \frac{V_{i+1,j} - V_{i-1,j}}{2\Delta x} - \frac{U_{i,j+1} - U_{i,j-1}}{2\Delta r} \quad (5.13)$$

where Δx and Δr are the measured distances between interrogation windows in the streamwise and cross stream directions, respectively. Notice that Eq. 5.13 is the

standard vorticity relationship normal to the xr plane with partial derivatives with respect to x and r estimated by a central difference formula.

5.3.5 Fluctuating velocity correlation

Fluctuating velocity was calculated by taking the difference between the instantaneous and mean velocity fields. Fluctuating velocity at a given (i,j) location was calculated using FlowManager™ as

$$u''_{ij} = u_{ij} - U_{ij} \quad (5.14)$$

$$v''_{ij} = v_{ij} - V_{ij} \quad (5.15)$$

The correlation between stream-wise and cross-stream fluctuating velocities at a given (i,j) location was calculated using a MatLab® program as

$$\overline{u'v'}_{ij} = \frac{1}{N} \sum_{k=1}^{k=N} u''_{ij,k} v''_{ij,k} \quad (5.16)$$

5.3.6 Kinetic energy of the mean flow

The two dimensional kinetic energy of the mean flow at a given (i,j) location was calculated using a MatLab® program as

$$Q_{ij}^2 = \frac{U_{ij}^2 + V_{ij}^2}{2} \quad (5.17)$$

The two dimensional kinetic energy of the turbulence was calculated using a MatLab® program at a given (i,j) location as

$$q^2 = \frac{\overline{u'_{ij}u'_{ij}} + \overline{v'_{ij}v'_{ij}}}{2} \quad (5.18)$$

5.3.8 Mean volumetric flow rate

Mean volumetric flow rate of air flowing through a plane normal to the jet exit was calculated using a MatLab® program as

$$\dot{Q} = \int_0^{r_0} U_{ij} \cdot 2\pi r \cdot dr \quad (5.19)$$

The outer radius r_0 of the jet was chosen such that the velocity at that location was equal to 5 percent of the local centerline velocity in the streamwise direction.

5.3.9 Generation of whole field image maps

Once the data described above were obtained, a Matlab® program was written to piece each of the five fields of view for each of the jet conditions studied together into one image map. Mean velocity vectors and turbulence intensities were normalized by the centerline exit velocity of each case. The X and R position vectors were scaled using the jet diameter; where $X = 0$ and $R = 0$ corresponded to the centerline of the jet at the nozzle exit.

5.4 Uncertainty Analysis

Uncertainty in the mass flow data was dependent upon the uncertainty in the pressure and temperature measurements for both the sonic flow meter and the rotameter (see Eqs. 5.1 and 5.5). Uncertainty in temperature and pressure measurements consisted of bias error associated with the calibration of transducers and precision error due to fluctuation of temperature and pressure during experimentation. Uncertainty values in pressure and temperature measurements for all cases are

reported in Table 5.1. Percent uncertainty for temperature and pressure measurements was based on the average value of the specific case reported. Uncertainty in mass flow rate was determined by applying the Kline-McClintock method (Figliola and Beasley (2000)) on Eqs. 5.1 and 5.5, respectively. Uncertainty values for mass flow rate measurements are reported in Table 5.1. Percent uncertainty for mass flow rate measurements was based on the average value measured for the specific case reported.

Table 5.1: The uncertainty in global measurements.

Re	u_{P_R} (kPa) [%]	$u_{P_{SF}}$ (kPa) [%]	u_{T_R} (°C) [%]	$u_{T_{SF}}$ (°C) [%]	$u_{\dot{m}_{MR}} \cdot (10^6)$ (kg/s) [%]	$u_{\dot{m}_{SF}} \cdot (10^4)$ (kg/s) [%]	$u_{\dot{m}_m} \cdot (10^4)$ (kg/s) [%]
27,000	1.27 [0.87]	2.64 [1.10]	0.35 [1.59]	0.38 [1.75]	6.94 [0.14]	4.59 [9.39]	4.59 [9.39]
49,000	0.78 [0.50]	2.24 [0.51]	0.36 [1.61]	0.51 [2.30]	6.51 [0.07]	9.14 [10.46]	9.14 [10.46]
71,000	0.67 [0.35]	3.98 [0.62]	0.46 [2.07]	0.58 [2.60]	7.96 [0.06]	14.9 [11.70]	1.49 [11.70]

As was discussed earlier, an acoustic study was performed to determine the collar lengths resulting in first and second stage ASEJ. The acoustic study was performed using a studio condenser microphone. The uncertainty in overall SPL data obtained using the condenser microphone was determined to be 3.79 dB. Appendix B shows details of how this uncertainty was determined.

In the PIV study, magnified images of the seed particles indicated that the average seed size seen by the camera was 11 μm . Note that the pixel pitch of the CCD camera was 6.45 μm , and the scale factor between real space and CCD chip was 5.37 on average. As a result of the factors described above the seed size (less than 1 pixel)

in the PIV images captured was less than the ideal size (between 2 and 3 pixels) required for low uncertainty (Keane and Adrian (1992)). Keane and Adrian (1992) determined that the uncertainty in the position for a particle size larger than two pixels in the CCD plane was 0.1 pixels. Dano (2005) justified using the 0.1 pixel uncertainty for seed size less than a pixel with larger density seeding (6-17 seeds per interrogation area) by creating artificial image pairs with known particle displacements and using the FlowManager™ software to determine the velocity field. Therefore, the uncertainty analysis presented here is based on a 0.1 pixel uncertainty for particle displacement.

Table 5.2: The uncertainty in PIV data

Re	$u_{u_{ij}}$ (m/s) [%]	$u_{U_{ij}}$ (m/s) [%]	$u_{u'}$ (m/s) [%]	u_{Ω} (1/s) [%]	$u_{\dot{Q}}$ (m ³ /s) [%]
27,000	0.99 [2.76]	0.04 [0.10]	0.99 [12.80]	206.48 [0.50]	1.44(10 ⁻⁴) [1.96]
49,000	2.31 [3.70]	0.08 [0.13]	2.31 [20.58]	479.06 [0.66]	1.72(10 ⁻⁴) [1.27]
71,000	2.31 [2.61]	0.08 [0.10]	2.31 [13.03]	479.06 [0.48]	2.99(10 ⁻⁴) [1.46]

Estimates of uncertainty in the instantaneous velocity, mean velocity, turbulent intensities, vorticity, and volumetric entrainment are presented in Table 5.2. Note that the percent uncertainty for instantaneous and mean velocities was based on the mean exit velocity of the jet. Percent uncertainty in turbulent intensity was based on the maximum value of turbulent intensity measured in the flow field for each case studied. Percent uncertainty in vorticity was based on the maximum vorticity measured in the flow field for each of the cases studied. Percent uncertainty in volumetric flow rate

was based on the local volumetric flow rate at the location chosen for uncertainty calculations.

In PIV it is not actually the velocity of the flow that is measured but the velocity of the seed particles following the flow. In order to ensure that the seed particles in a flow are actually tracking with the flow, it is important to determine the particle response time and frequencies to a change in flow direction. The equation of motion for a spherical particle in a gas is given by (Dantec Dynamics (2000)):

$$\frac{\pi}{6} d_p^3 \rho_p \frac{dU_p}{dt} = -3\pi\mu d_p V + \frac{\pi}{6} d_p^3 \rho_f \frac{dU_f}{dt} - \frac{\pi}{12} d_p^3 \rho_f \frac{dV}{dt} -$$

Accelerating flow	Stokes viscous force	Pressure gradient force on fluid	Fluid resistance to accelerating sphere	(5.20)
----------------------	----------------------------	---	--	--------

$$- \frac{3}{2} d_p^2 \sqrt{\pi\mu\rho_f} \int_{t_0}^t \frac{\pi}{6} d_p^3 \rho_f \frac{dV}{d\xi} \frac{d\xi}{\sqrt{t-\xi}}$$

Drag force associated with
Unsteady motion

where subscripts p relate to the particle and subscripts f relate to the surrounding fluid. For an approximation of particle response time and frequencies the pressure gradient force, fluid resistance, and drag force associated with unsteady motion can be neglected, leaving a balance between the acceleration force and the viscous force,

$$\frac{dU_p}{dt} = - \frac{18\mu(U_p - U_f)}{d_p^2 \rho_p} \quad (5.21)$$

Solving the differential equation above results in

$$U_p = A(1 - e^{-t/\tau}) \quad \text{with} \quad \tau = \frac{d_p^2 \rho_p}{18\mu} \quad (5.22)$$

where τ is the time constant, d_p is the diameter of the seed particle, ρ_p is the density of olive oil, 900 kg/m^3 , and μ is the viscosity of air, $1.79(10^{-5}) \text{ kg/s}\cdot\text{m}$. Based on a seed particle diameter of $11 \text{ }\mu\text{m}$ the time constant for a particle response to a step change in velocity is $340 \text{ }\mu\text{m}$. Based on the value of τ , two indicative frequencies characterizing the frequency response of the particle to a sudden change in flow direction are given by

$$f_{3\text{dB}} = \frac{1}{2\pi\tau} \quad (5.23)$$

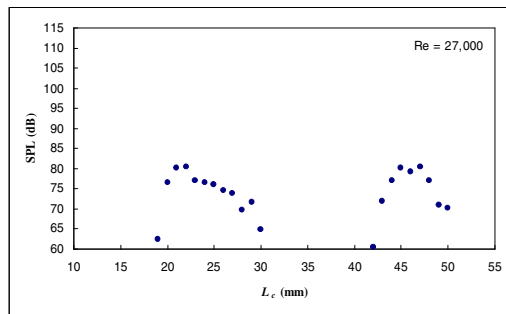
where $f_{3\text{dB}}$ is the frequency within 3dB (error 37 percent) and the frequency leading to an error of 10 percent, $f_{10\%}$ is given by

$$f_{10\%} = \frac{0.5}{2\pi\tau} \quad (5.24)$$

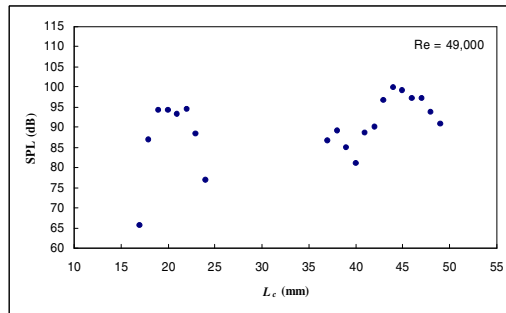
In this study $f_{3\text{dB}}$ and $f_{10\%}$ were 0.470 and 0.227 kHz , respectively.

6 RESULTS AND DISCUSSION

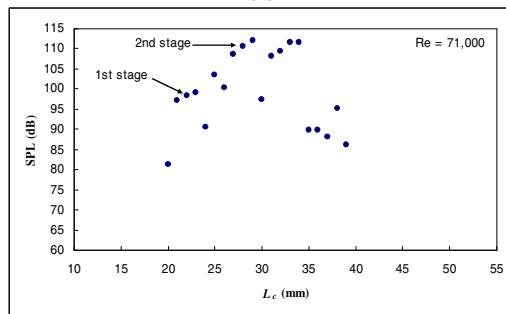
In this chapter results for both the acoustic and PIV studies are presented. First, acoustic data used to determine collar lengths resulting in first and second stage ASEJ are presented. Second, centerline PIV data are presented in order to compare data from the current study to a similar study (Hasan and Hussain (1982)) performed with hot-wire anemometry. Finally, the whole field PIV data is presented to characterize the near-field flow structure of first and second stage ASEJ relative to the unexcited jet.



(a)

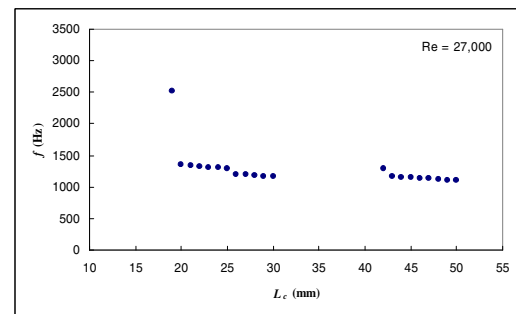


(b)

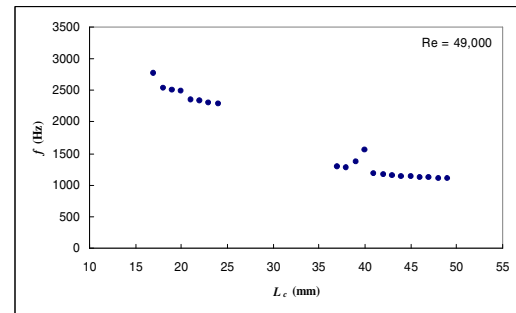


(c)

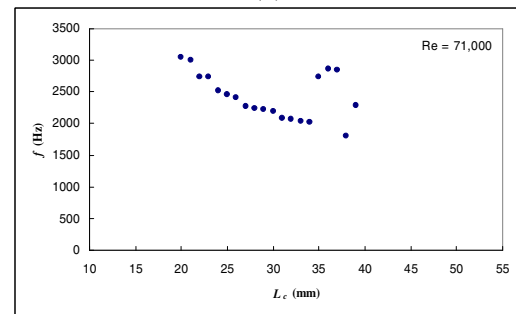
Figure 6.1: SPL as a function of L_c .



(a)



(b)



(c)

Figure 6.2: SPL f as a function of L_c .

6.1 Collar length study – Sound pressure level and frequency

An acoustic study was performed to determine the collar lengths (L_c) that resulted in the first and second stages of the acoustically self excited jet (ASEJ). Figure 6.1 shows the overall Sound Pressure Level (SPL) of the jet as a function of L_c for the three cases studied (i.e. $Re = 27,000, 49,000$ and $71,000$). From Fig. 6.1, it is clear that as L_c is increased, a loud pure tone was suddenly produced, increased in intensity, and then the pure tone abruptly became inaudible. In Fig. 6.2 the pure tone frequency of the ASEJ as a function of L_c is presented. From Fig. 6.2, it is clear that the ASEJ frequency decreased slightly as L_c was increased within a stage. The slight decrease of frequency with increasing L_c and the abrupt appearance and disappearance of the loud pure tone associated with first and second stage ASEJ is consistent with data obtained by Hasan and Hussain (1983).

Table 6.1. ASEJ collar lengths based on acoustic data for 1st and 2nd stage excitation.

Re	j	n	L_c (mm) (L_c/D)	f (Hz)	St_D	SPL (dB)	f_H (Hz)	f & f_H % diff
27,000	1	1/2	22 (2.31)	1320	0.47	80	1162	12.7
49,000	1	1	20 (2.10)	2487	0.51	94	2377	4.52
71,000	1	1	22 (2.31)	2241	0.32	98	2323	-9.8
27,000	2	1/2	45 (4.74)	1146	0.41	80	1155	-0.8
49,000	2	1/2	44 (4.63)	1143	0.23	100	1162	-1.6
71,000	2	1	28 (2.95)	2737	0.39	112	2553	6.9

In Table 6.1, the overall SPL, excitation frequencies, and collar lengths determined from the data in Figs. 6.1 and 6.2 are presented for both first and second stage ASEJ. The seventh column of Table 6.1 is the Strouhal number (non-dimensional frequency of excitation) based on the pipe nozzle exit diameter and exit velocity of the unexcited jet. The eighth column of Table 6.1 shows frequencies calculated using the correlation from Hasan and Hussain (1979) where, a_o is the local speed of sound in air (i.e. assumed constant 341 m/s), j is the stage of excitation (i.e. 1st, 2nd, etc.), n is the mode of excitation (i.e. either half mode or full mode), L_c is the collar length, L_p is the pipe length, and D is the pipe diameter.

$$f_H = \frac{a_o n}{L_p + 1.65 \left(\frac{L_c}{j} \right) + 0.70 D} \quad (6.1)$$

Percent difference between measured (f) and calculated (f_H) frequencies using the Hasan and Hussain (1979) correlation is denoted in the eighth column of Table 6.1. In general measured frequency data matched the Hasan and Hussain (1979) correlation well, with a maximum deviation of 12.7 percent. It should be noted that the step height h , of 0.953 cm used in this study was outside the range of step heights from 0.318 cm to 0.635 cm that were used to determine Eq. 6.1.

6.2 PIV studies - Centerline data

In earlier studies of acoustically excited jets (i.e. Crow and Champagne (1970); Hill and Greene (1977); Hasan and Hussain (1982); Drobniak and Klajny (2002)), experiments were performed using hot wire anemometers. A limitation of this measurement technique is that it provides only a few point measurements at any

instant in time. In order to overcome this limitation earlier researchers traversed the anemometer along numerous streamwise and cross-stream lines within the flow. Plots of the streamwise variation of mean velocity and turbulent intensity along the center line and selected lines corresponding to constant fractions of exit mean velocity along the shear layer of the jet has historically been one method of characterizing axisymmetric turbulent jets. In this study PIV measurements were performed to obtain whole field quantitative mean velocity and turbulent intensity measurements. However, by extracting data along the centerline of the PIV measurements data from this study can be compared to earlier studies using hot wire anemometry.

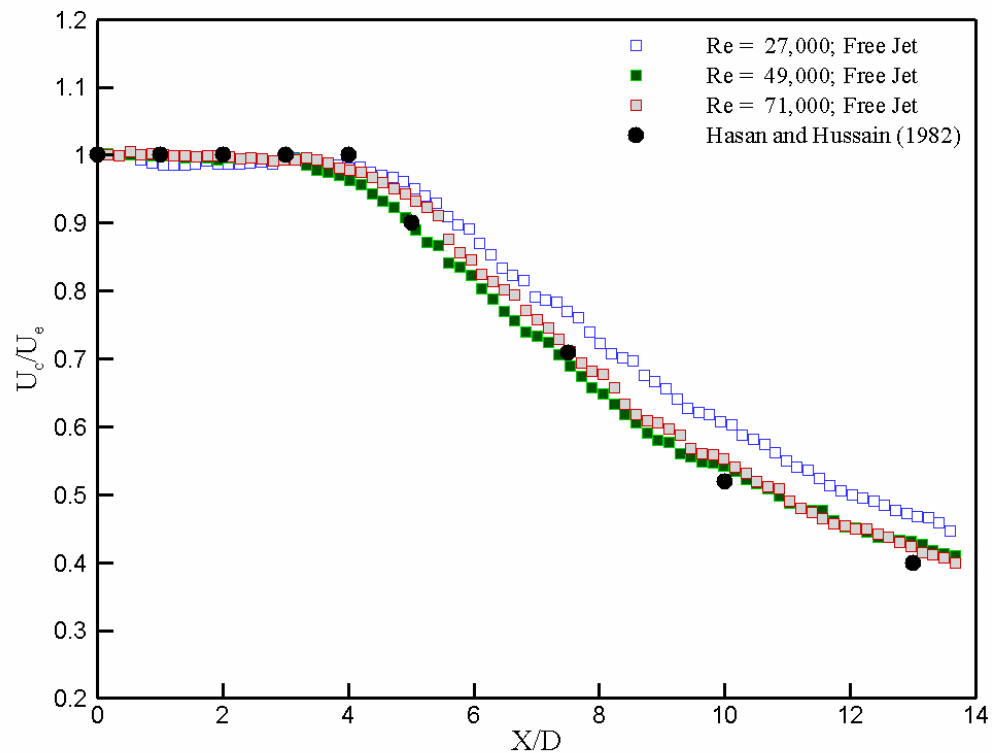


Figure 6.3: Comparison of streamwise variation of U_c/U_e along the centerline of the jet for the unexcited jet with Hasan and Hussain (1982).

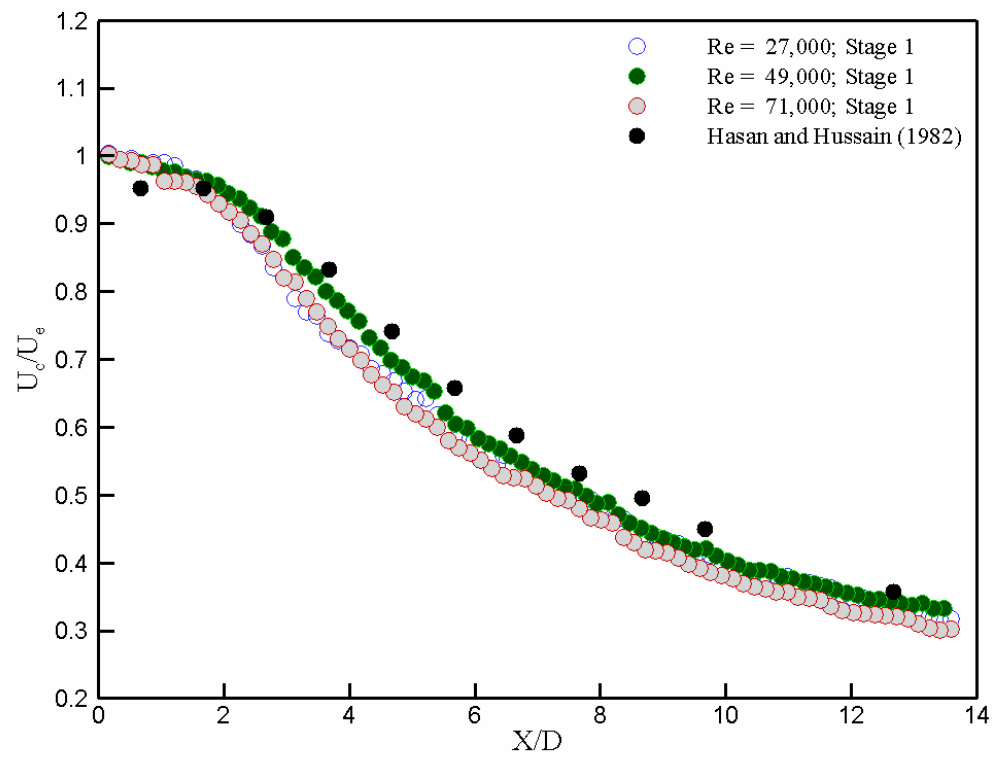


Figure 6.4: Comparison of streamwise variation of U_c/U_e along the centerline of the jet for first stage ASEJ with Hasan and Hussain (1982).

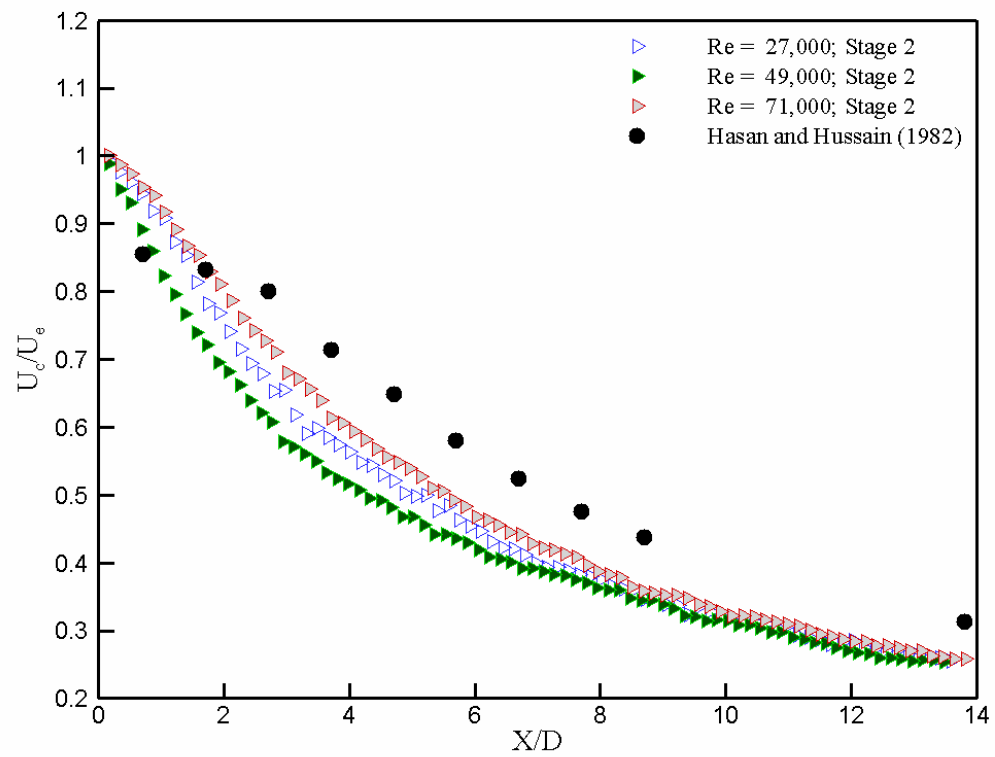


Figure 6.5: Comparison of streamwise variation of U_c/U_e along the centerline of the jet for second stage ASEJ with Hasan and Hussain (1982).

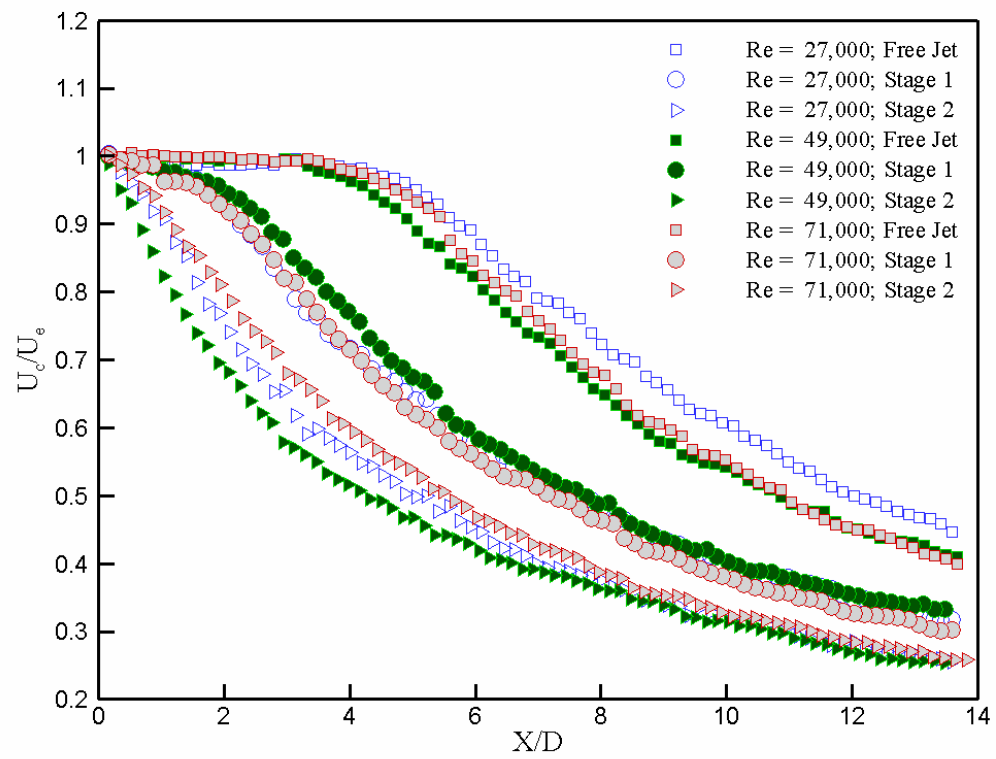


Figure 6.6: Streamwise variation of U_c/U_e along the centerline of the jet.

In Fig. 6.3, plots of the streamwise variation of streamwise mean velocity U_c along the centerline of the jet are compared to Hasan and Hussain (1982) for unexcited jet conditions. Note that the origin for unexcited jet data was at the center of the pipe nozzle exit. For unexcited jet conditions, U_c was normalized using the streamwise mean velocity U_e measured using PIV at the center of the pipe nozzle exit. In Table 6.2, the values used for U_e in all jet conditions studied are shown.

Table 6.2: Values of U_e for all jet conditions studied.

Re	Unexcited jet, U_e (m/s)	1 st stage ASEJ, U_e (m/s)	2 nd stage ASEJ, U_e (m/s)
27,000	88.44	83.87	80.67
49,000	62.51	60.37	57.93
71,000	35.83	34.21	30.23

The specific case chosen for comparison from Hasan and Hussain (1982) for all jet conditions was an ASEN having a pipe length of 15.24 cm, a pipe jet diameter of 2.54 cm, an exit mean velocity of 36 m/s, a Reynolds number of 62,000, and Strouhal numbers of 0.635 and 0.629 for first and second stage ASEJ, respectively. The non-dimensional collar lengths for first and second stage ASEJ (Hasan and Hussain (1982)) was approximately 0.33 and 1.2 pipe jet diameters, respectively. From Fig. 6.3 it is clear that streamwise variation in U_c/U_e for unexcited jet conditions agrees well with the data of Hasan and Hussain (1982). In Fig. 6.4, comparison of first stage ASEJ conditions to Hasan and Hussain (1982) are shown. Note that for ASEJ conditions in this study U_e were measured using PIV at the center of the collar exit rather than the pipe exit as in unexcited jet conditions, and that the origins for ASEJ conditions were

at the center of the collar exit rather than the pipe exit as in unexcited jet conditions. From Fig 6.4 it is clear that streamwise variation of first stage ASEJ conditions agree well with the data of Hasan and Hussain (1982). Figure 6.5 shows comparison of the second stage ASEJ conditions to Hasan and Hussain (1982). This figure indicates that there is a deviation in U_c data for second stage ASEJ compared to Hasan and Hussain (1982). A deviation in second stage data will be apparent in turbulent intensity data as well, reasons for which will be discussed later.

Figure 6.6 is a plot of U_c for all jet conditions studied. Note, trends in streamwise decay of U_c shown in Fig. 6.6 with variation in Reynolds numbers are similar for like cases (i.e. unexcited jet, first or second stage ASEJ). This similarity indicates that both the ASEJ and free jet are Reynolds number independent for the range of Reynolds numbers studied. Crow and Champagne (1970) shows a similar collapse of the streamwise variation in U_c profiles for an unexcited circular pipe jet having Reynolds numbers of 62,000, 83,000 and 103,000. Notice in Fig. 6.6 that the unexcited jets potential core remains up to between 4.5 and 5.0 diameters down stream of the pipe exit. However, at 5.0 diameters downstream of the nozzle exit the first and second stage ASEJ centerline velocity has decayed to approximately 70 and 50 percent, respectively of U_e . This earlier decay in streamwise mean velocity along the centerline of the jet is a strong indicator of increased mixing which causes greater entrainment of surrounding fluid into the near field of an ASEJ when compared with the unexcited jet.

Note that Hasan and Hussain (1982) chose the nozzle pipe exit as the origin ($X/D = 0.0$) for ASEJ and unexcited jet conditions. If the pipe exit is chosen instead of the collar exit for ASEJ conditions, data in Figs. 6.3-6.6 are translated to the right by the respective L_c of first and second stage ASEJ (approximately 2 nozzle pipe diameters for first stage ASEJ and 3.5 nozzle pipe diameters for second stage ASEJ). In this case, the decay in mean velocity at 5.0 nozzle pipe diameters downstream of the pipe exit is 90 and 80 percent of U_e for first and second stage ASEJ, respectively.

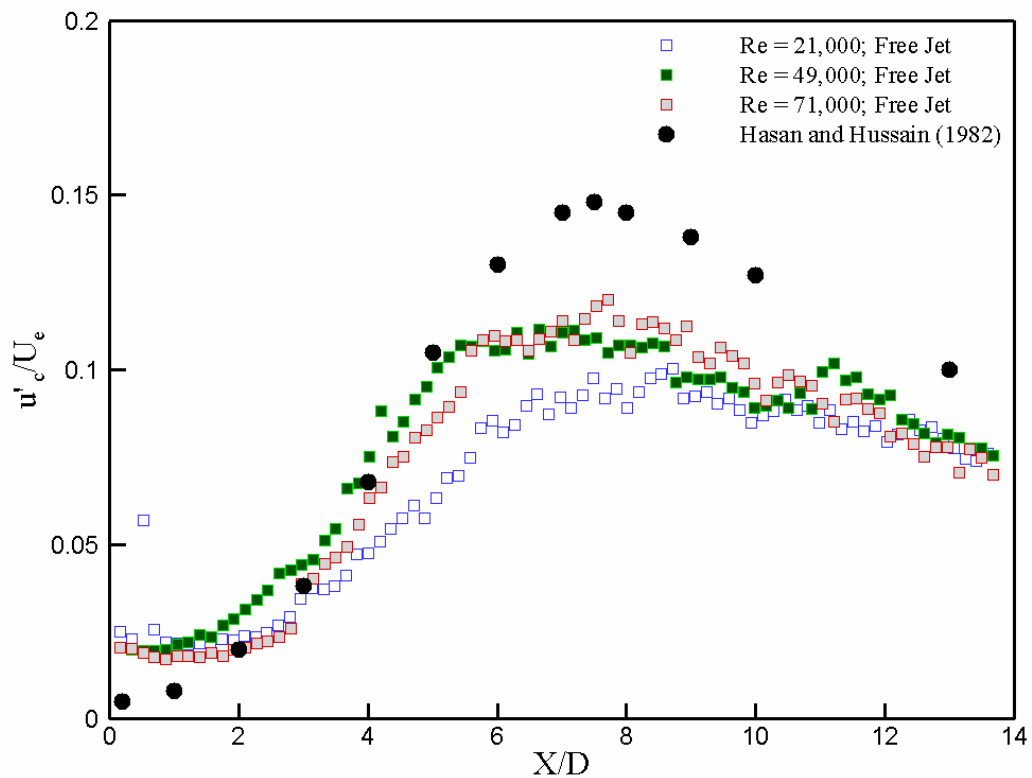


Figure 6.7: Comparison of streamwise variation of u'_c/U_e along the centerline of the jet for the unexcited free jet with Hasan and Hussain (1982).

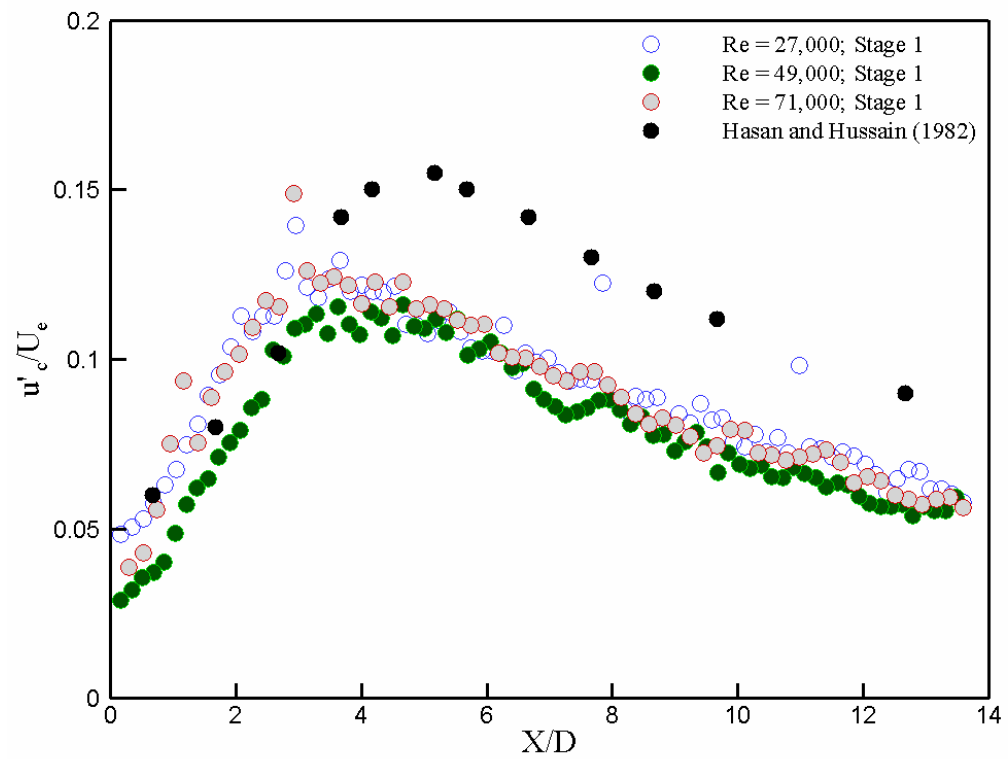


Figure 6.8: Comparison of streamwise variation of u' / U_e along the centerline of the jet for first stage ASEJ with Hasan and Hussain (1982).

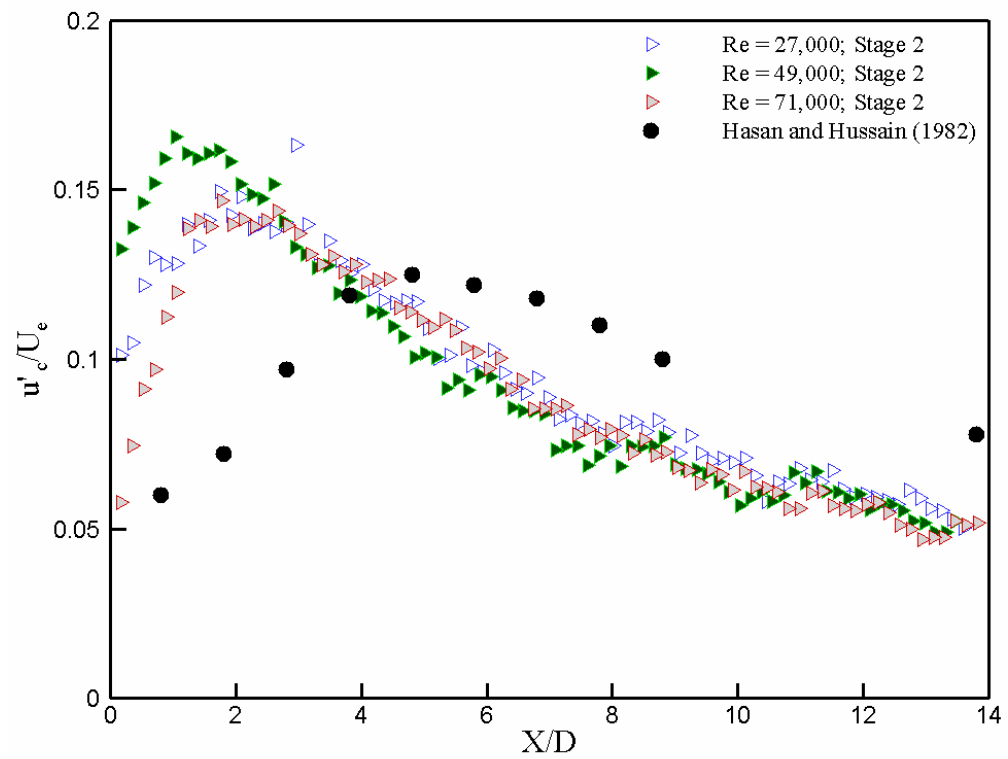


Figure 6.9: Comparison of streamwise variation of u'_c/U_c along the centerline of the jet for second stage ASEJ with Hasan and Hussain (1982).

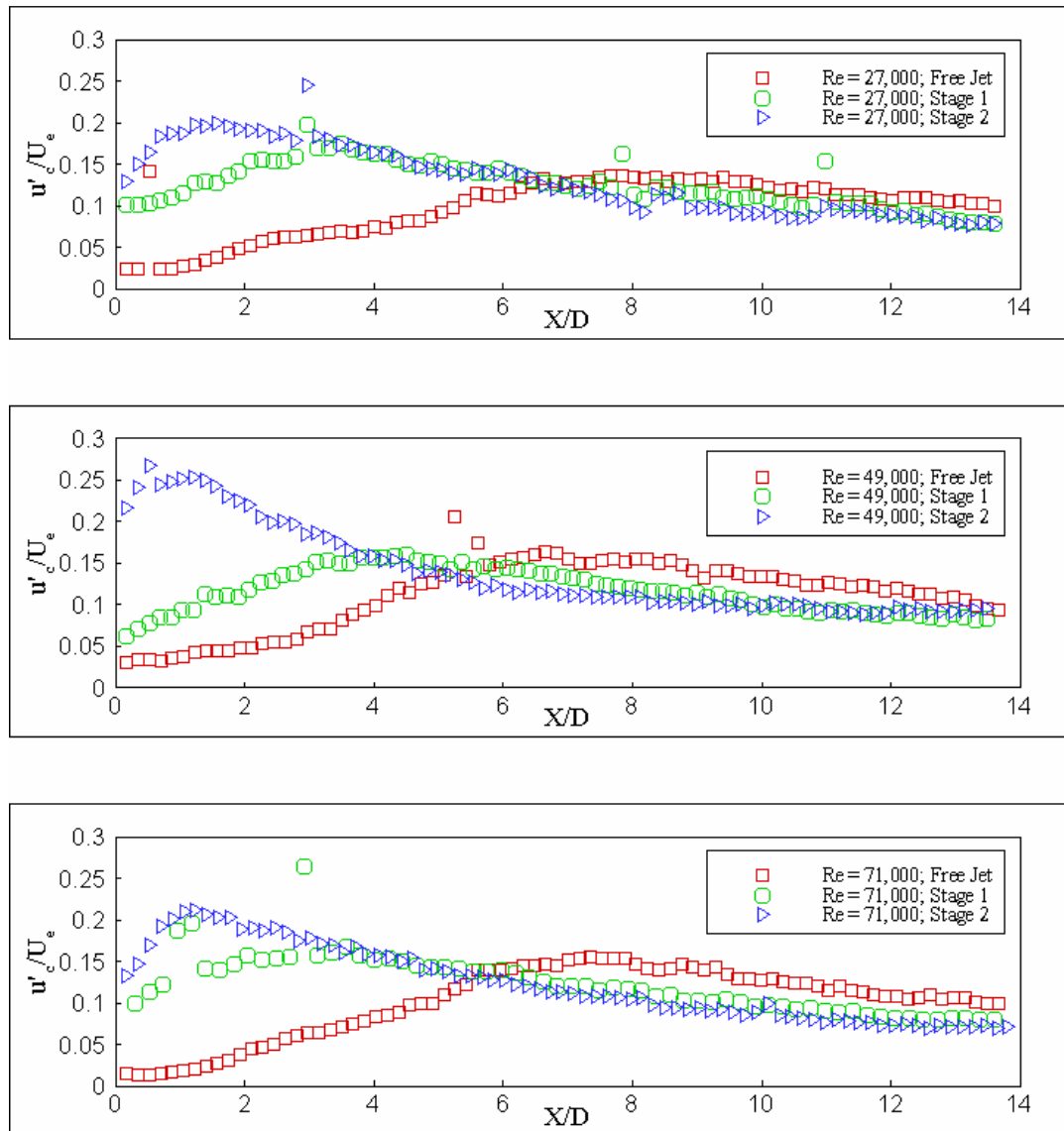


Figure 6.10: Streamwise variation of u'_c/U_e along the centerline of the jet.

A comparison with Hasan and Hussain (1982) for the streamwise turbulent intensity u'_c along the centerline of the jet is shown in Figs. 6.7-6.9. Again, turbulent intensity was normalized using the same U_c shown in Table 6.2. In Fig. 6.7, unexcited jet conditions are shown to have peaks in u'_c at approximately 7-8 jet exit diameters from the nozzle exit, agreeing well with the peak in u'_c measured by Hasan and Hussain (1982). From Fig. 6.7 it is clear that the magnitudes of peak u'_c for unexcited jet conditions are approximately 10 percent. The magnitude in peak turbulent intensity measured by Hasan and Hussain (1982) was approximately 15 percent. The reason for the lower magnitude in peak u'_c in this study is thought to be related to the seeded flow required to obtain PIV measurements. It is reasonable to assume that some of the turbulent and mean flow kinetic energy of the jet would go into moving the seed particles for PIV measurements relative to going into generation of turbulence for the unseeded flow studied by Hasan and Hussain (1982). Also, Hasan and Hussain (1982) document the jet initial condition for all jet conditions studied by recording the streamwise turbulent intensity at the center of the pipe exit and the exit boundary layer of the pipe nozzle. In this study, because the first PIV measurement was 1 mm away from the nozzle exit and because of the low spatial resolution of PIV measurements relative to the exit boundary layer thickness, the jet initial condition was not documented. It is therefore possible that the magnitude of turbulent intensity at the pipe nozzle exit for the current study is less than that of Hasan and Hussain (1982) which would have an effect on the streamwise variation of u'_c thus explaining the lower magnitude of peak u'_c . In Fig. 6.8, first stage ASEJ conditions are compared to Hasan and Hussain (1982). It is clear from Fig. 6.8 that first stage ASEJ conditions

peak in u'_c locations agree well with Hasan and Hussain (1982) but, are slightly shifted closer to the jet exit. Again, magnitudes of peak u'_c for ASEJ conditions are less than that measured by Hasan and Hussain (1982). In Fig. 6.9 second stage ASEJ conditions are compared to Hasan and Hussain (1982). From Fig. 6.9 it is clear that second stage ASEJ conditions do not agree well with Hasan and Hussain (1982). The deviation of second stage ASEJ conditions compared to Hasan and Hussain (1982) is thought to be due to acoustic feedback from the enclosure walls.

Figure 6.10 presents a plot of the streamwise variation of u'_c along the centerline of the jet for all jet conditions studied. From Fig. 6.10, it is clear that u'_c is amplified in the near field for the first and second stage ASEJ when compared to the unexcited jet, with the largest increase occurring in second stage ASEJ. Peak turbulent intensity for second stage ASEJ is between 20 and 25 percent of U_e and occurs between 1 and 1.5 diameters downstream of the collar exit. In comparison, peak turbulent intensity for first stage ASEJ is between 10 and 15 percent of the mean exit velocity located 3.5 to 4 diameters downstream of the collar exit. Notice that peaks in turbulent intensity are approximately the same (10 percent of U_e) for the unexcited jet conditions and first stage ASEJ conditions. It is seen by comparing Figs. 6.7 and 6.8 that the peaks in u'_c for Hasan and Hussain (1982) are approximately the same (15 percent of U_e). This trend in magnitude of peak u'_c again demonstrates good agreement between this study and that of Hasan and Hussain (1982) for both the unexcited jet and first stage ASEJ conditions. If the pipe exit rather than the collar exit is chosen as the starting point for ASEJ peak turbulent intensity positions translate to the right in Fig.

6.10 by the respective L_c of first and second stage ASEJ (approximately 2 nozzle pipe diameters for first stage ASEJ and 3.5 nozzle pipe diameters for second stage ASEJ).

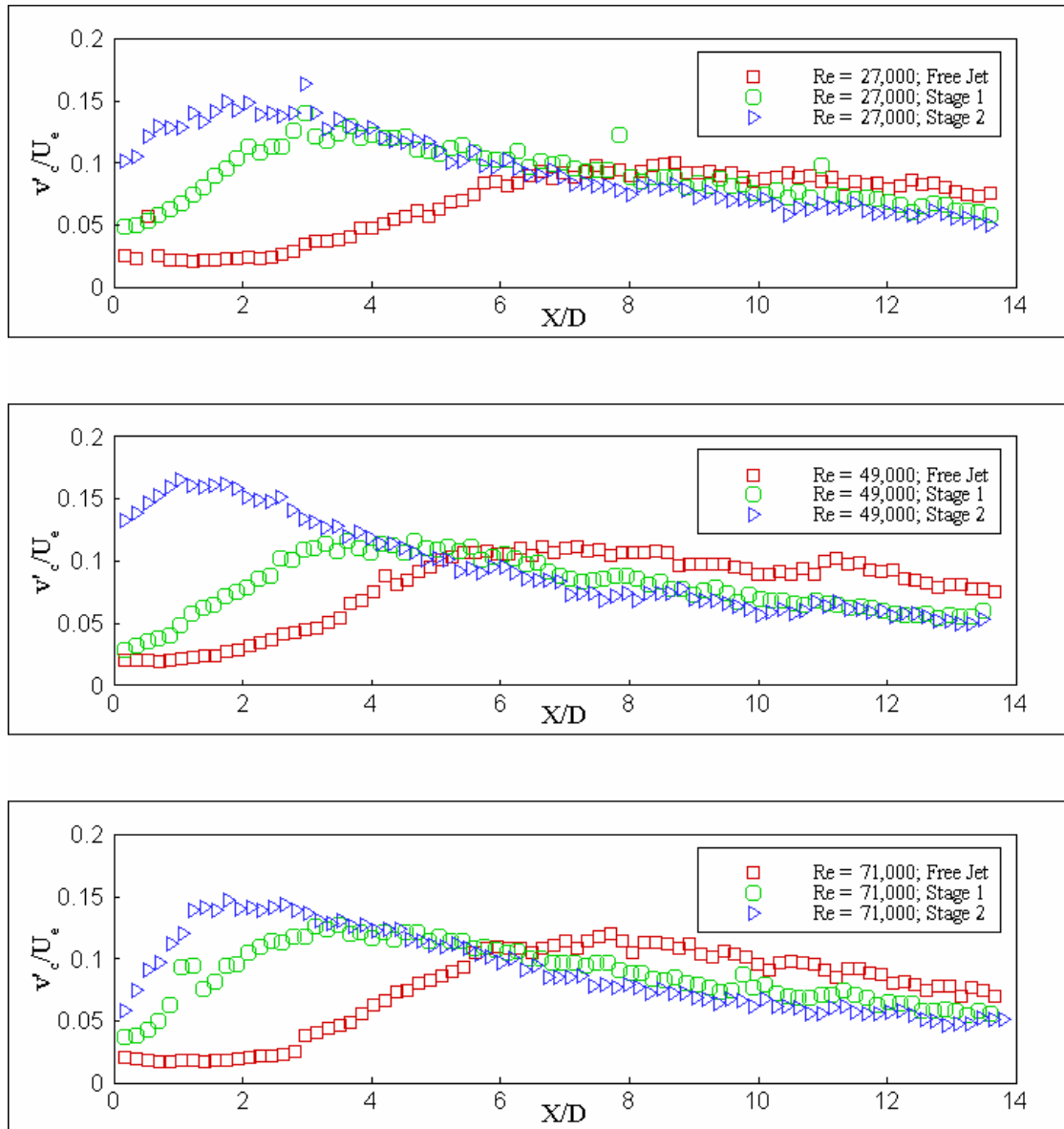


Figure 6.11: Cross-stream variation of v'_c/U_e along the jet centerline.

Jet centerline variation of cross-stream turbulent intensity is presented in Fig. 6.11 normalized using U_e . In Fig 6.11 v'_c for unexcited jet cases is shown to follow the same general trend as u'_c however, peak v'_c is only 10 percent of U_e compared to the 15 percent peaks seen in Fig 6.10 for u'_c . In earlier studies such as Crow and Champagne (1970); Hill and Greene (1977); Hasan and Hussain (1982); Drobniak and Klajny (2002) v'_c was not reported explicitly and hence cannot be compared here. In Fig 6.11, it is clear that v'_c is enhanced for first and second stage ASEJ in the near field when compared to the unexcited jet. As was the case for u'_c , the largest enhancement of v'_c (15 to 17 percent) occurs in the second stage ASEJ between approximately 1.5 and 2 diameters downstream of the jet exit. Peak v'_c in first stage ASEJ is approximately 12 percent and occurs between 3 and 4 diameters from the jet exit. If the pipe exit was chosen as the origin instead of the collar exit the peak v'_c locations shift to the right in Fig. 6.11 by the respective L_c for first and second stage ASEJ.

Figure 6.12 shows streamwise variation of the volumetric flow rate \dot{Q}/\dot{Q}_e for the three jet conditions studied; \dot{Q}_e is the exit volumetric flow rate of the unexcited jet. Exit volumetric flow rate was calculated by dividing the average mass flow rate of each jet condition measured using the mass flow meters by the density of air. The values of \dot{Q}_e calculated were 0.00398, 0.00707, and 0.0103 m³/s for the jet conditions having a Reynolds number of 27,000, 49,000, and 71,000, respectively. Figure 6.12 indicates that the volumetric flow rate increases as a function of distance

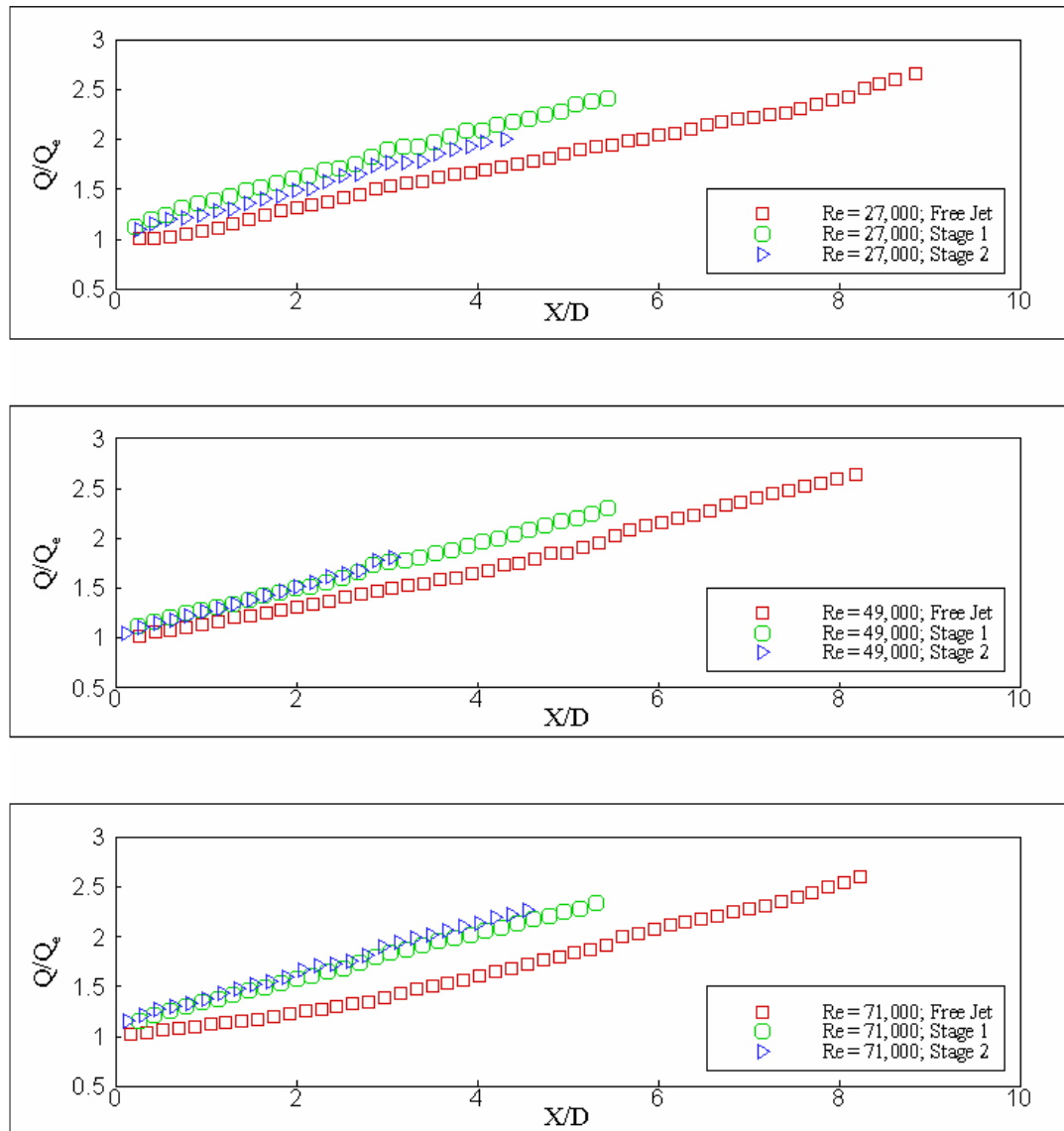


Figure 6.12: Streamwise variation of \dot{Q}/\dot{Q}_e .

from the jet exit. This increase in volumetric flow rate is due to the spread of the jet by entrainment of the surrounding air into the jet. Notice that \dot{Q}/\dot{Q}_e for first and second stage ASEJ is greater than that of the free jet for the entire range reported however; the curves for excited jets compared to first and second stage ASEJ have equal slopes. This suggests that the acoustic self-excitation has the effect of moving the virtual origin of the jet upstream of the ASEJ exit without increasing the rate of entrainment. Hasan and Hussain (1982) show the same effect in their similar study using hot-wire anemometry. Note if the pipe exit rather than the jet exit was used as the origin the data for first and second stage ASEJ shifts to the right by the respective L_c for first and second stage ASEJ resulting in volumetric flow rates close to identical for unexcited jets and first and second stage ASEJ.

6.3 Whole field results

Because trends in the whole field data maps are similar for the three Reynolds numbers studied, only data for $Re = 49,000$ is presented here. Figure 6.13 a, b, & c presents the whole field variation in streamwise mean velocity U_e for the unexcited jet, the first, and second stage ASEJ, respectively. Again, this velocity is normalized using U_e , the mean velocity at the pipe exit for unexcited jets and collar exit for first and second stage ASEJ. Both the X and R axis are scaled by the pipe inner diameter D, of 1.27 cm. Notice that the shape of the U/U_e profile at the jet exit changes from top-hat, typical of fully developed turbulent pipe flow in Fig 6.13a, to a partially parabolic partially top-hat mean velocity profile at the collar exit for the first stage ASEJ Fig.

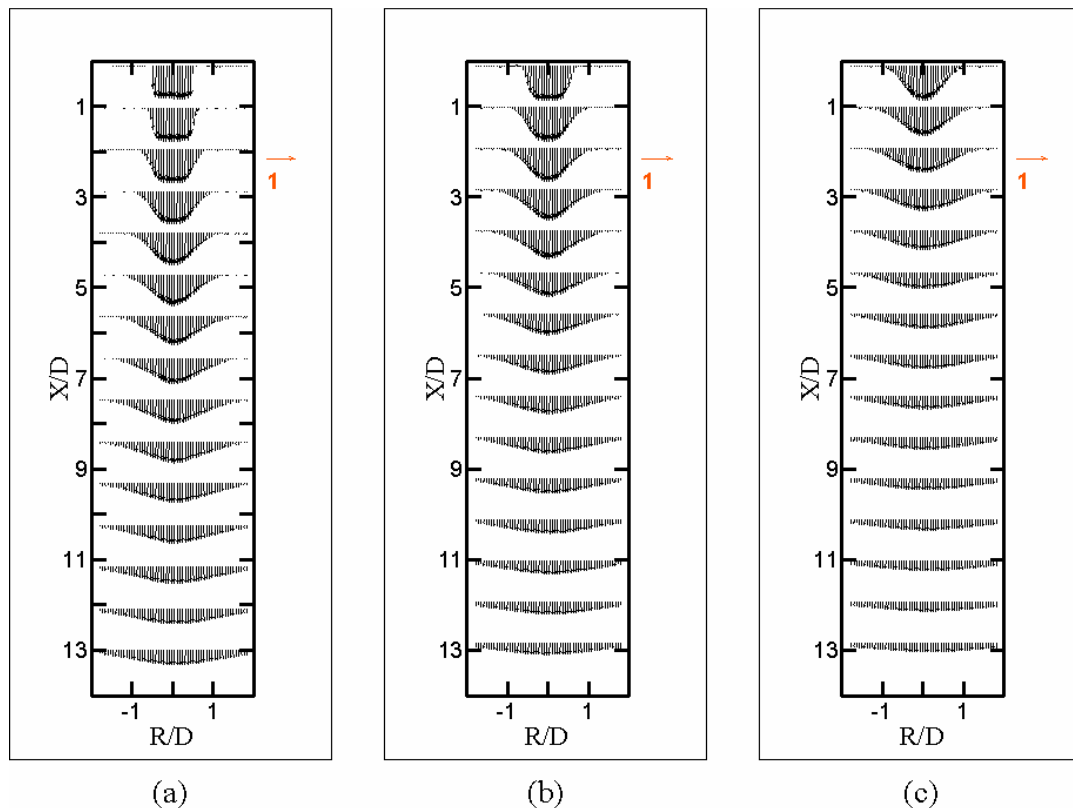


Figure 6.13: Whole field streamwise variation of U/U_e - (a) unexcited jet, (b) first stage ASEJ, (c) second stage ASEJ.

6.13b. Comparing Fig. 6.13b to Fig. 6.13c reveals that the collar exits mean velocity profile for the second stage ASEJ is parabolic compared to the part parabolic/top-hat collar exit mean velocity profile of the first stage ASEJ. The parabolic mean velocity profile at the collar exit for the second stage ASEJ signifies greater diffusion of momentum across the jet indicating larger spread of the jet for second stage ASEJ compared to first stage ASEJ.

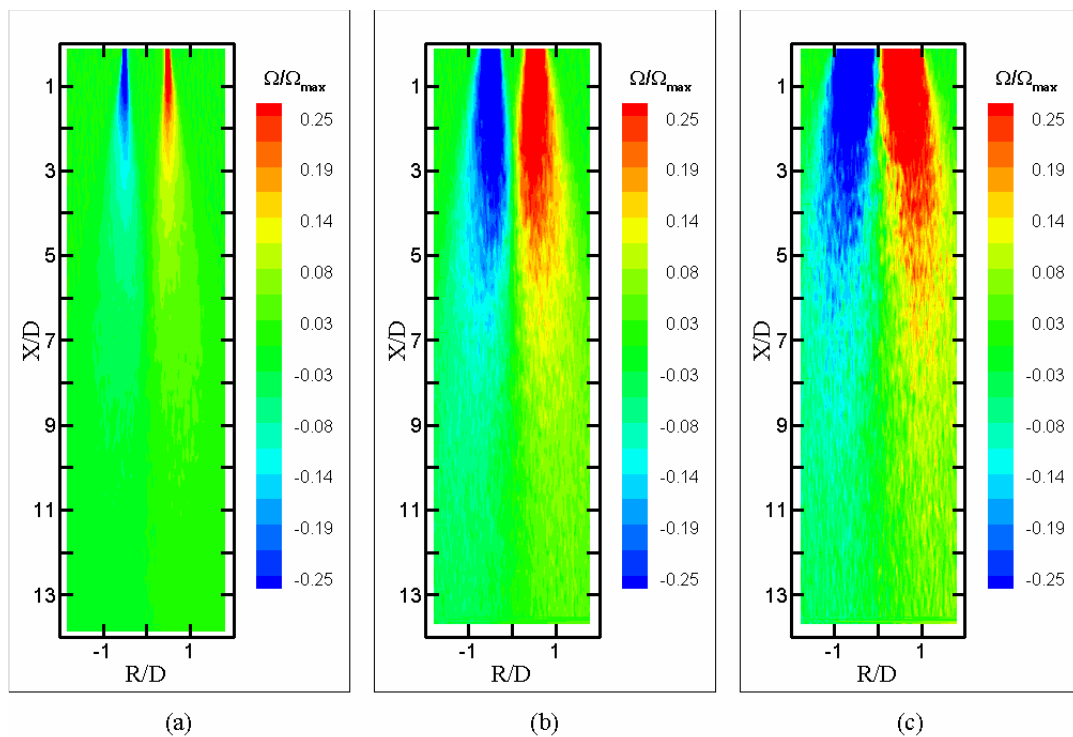


Figure 6.14: Whole field variation of mean vorticity Ω/Ω_{\max} - (a) unexcited jet, (b) first stage ASEJ, (c) second stage ASEJ.

Whole field variation of mean vorticity, Ω , is presented in Figs. 6.14 a, b, & c, for the unexcited jet, the first, and second stage ASEJ, respectively. Mean vorticity is normalized using the maximum mean vorticity, Ω_{\max} , measured within each flow field which was 72,430, 16,494, and 6,969 1/s for the unexcited jet, first, and second stage ASEJ, respectively. The maximum vorticity in each dataset was chosen to normalize

the vorticity data because it allows for unexcited and ASEJ cases to be compared to one another on the same scale (i.e. $0 \leq \Omega_{\max} \leq 1$). Another possible scaling factor would be U_e/D where D is the pipe nozzle inner diameter or, U_e/θ where θ is the momentum thickness of the shear layer at the pipe-nozzle exit. However, U_e/D does not scale the vorticity maps to unity and a determination of θ at the nozzle exit was not possible using PIV due to poor resolution. Notice in Figs. 6.14 a-c that vorticity is greatest close to the nozzle exit and concentrated in the developing shear layer. From Figs 6.14, it is clear that the span wise extent of high vorticity near the nozzle exit is greatest for second stage ASEJ when compared to first stage ASEJ and the unexcited jet. The presence of larger vorticity is indicative of a larger shear layer for first and second stage ASEJ implying that ASEJ experience more turbulent mixing in the near field of the jet when compared to the unexcited jet.

Whole field variation in streamwise turbulent intensity, u' , is presented in Figs. 6.15 a, b, & c, for the unexcited jet, first, and second stage ASEJ, respectively. Likewise, whole field variation of cross-stream turbulent intensity, v' , is presented in Figs. 6.16 a, b, & c, for the unexcited jet, first, and second stage ASEJ, respectively. Both u' and v' are normalized by the streamwise mean velocity, U_e , at the pipe exit for the unexcited jet and the collar exit for first and second stage ASEJ. Presented in this manner, the scale for the plots of Figs. 6.15 and 6.16 are identical and permit a direct comparison of magnitudes. In Fig. 6.15, it is seen that the magnitude of u'/U_e near the jet exit is enhanced for first and second stage ASEJ when compared to the unexcited jet. Also, the magnitude of u'/U_e for second stage ASEJ is enhanced compared to first

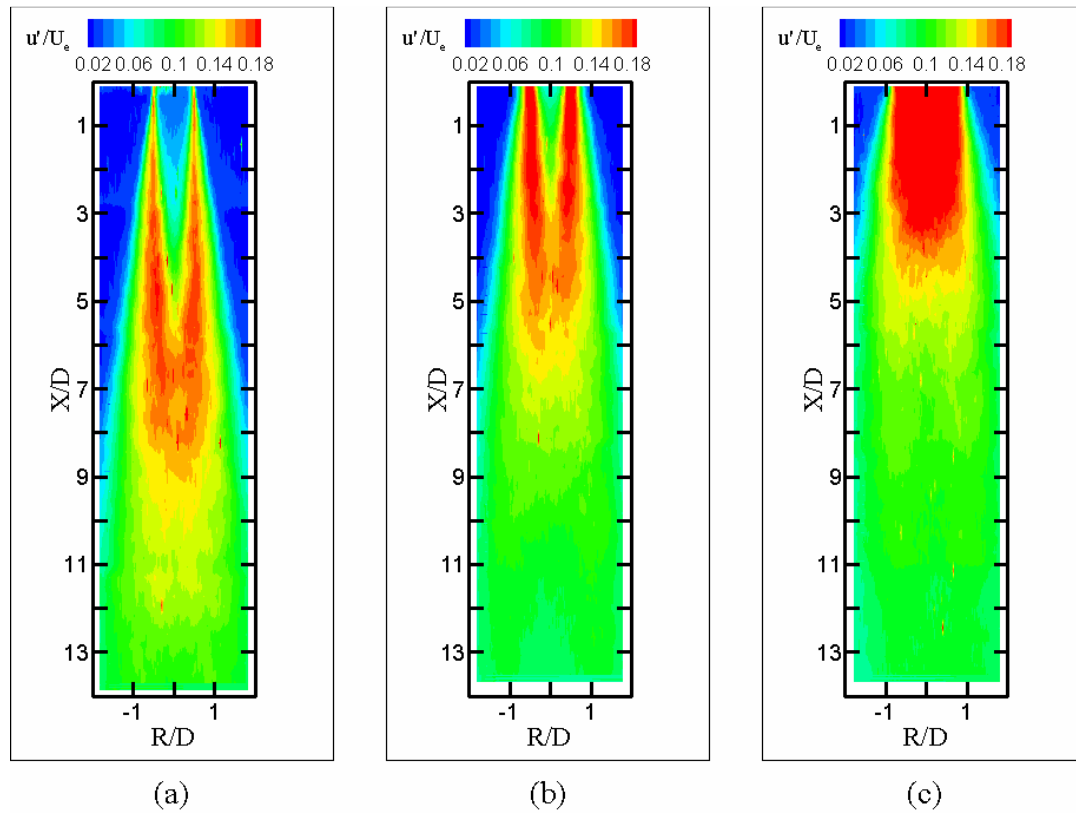


Figure 6.15: Whole field streamwise variation of u'/U_e - (a) unexcited jet, (b) first stage ASEJ, (c) second stage ASEJ.

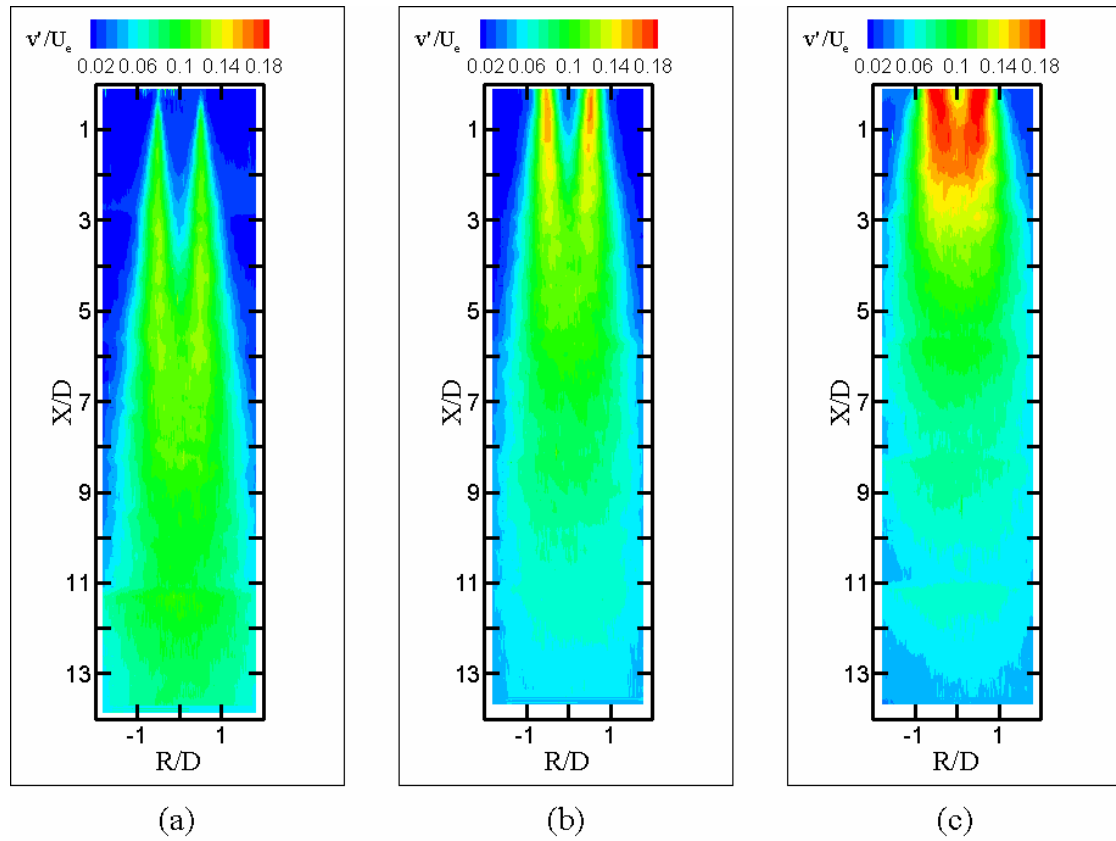


Figure 6.16: Whole field streamwise variation of v'/U_e - (a) unexcited jet, (b) first stage ASEJ, (c) second stage ASEJ.

stage ASEJ. In Fig. 6.16, it is seen that the magnitude of v'/U_e near the jet exit is enhanced for first and second stage ASEJ when compared to the unexcited jet. Also, the magnitude of u'/U_e for second stage ASEJ is enhanced compared to first stage ASEJ. Comparing Figs 6.15 and 6.16 indicate that the u'/U_e for both the ASEJ and unexcited jet are larger than v'/U_e . This is because u'/U_e is in the direction of the mean flow containing most of the turbulent kinetic energy and v'/U_e is a result of a redistribution of turbulent kinetic energy in the jet.

Figure 6.17 a, b & c, are plots of the correlation of streamwise and cross-stream fluctuating velocity, $\overline{u'v'}$, for the unexcited jet, first, and second stage ASEJ, respectively normalized with U_e^2 . The significance of the fluctuating velocity correlation is discussed by Tennekes and Lumley (1972). By examining the kinetic energy of the mean flow Tennekes and Lumley (1972) explain that the expression $-\overline{\rho u'_i u'_j S_{ij}}$ is the turbulent energy production where, ρ is density and S_{ij} is the rate of strain tensor of the mean flow. They show that the turbulent energy production serves to exchange kinetic energy from the mean flow to the turbulence. Figures 6.17 a, b & c, indicate that there is an increase in $\overline{u'v'}$ for both the first and second stage ASEJ in the near field compared to the unexcited jet. Also, the extent of the increased region of $\overline{u'v'}$ is greater for second stage ASEJ compared to first stage ASEJ. Note that in all cases $\overline{u'v'}$ is concentrated in the shear layer of the jet and is negligible in the center of the jet indicating the exchange of mean kinetic energy to turbulence is greatest in the shear layer.

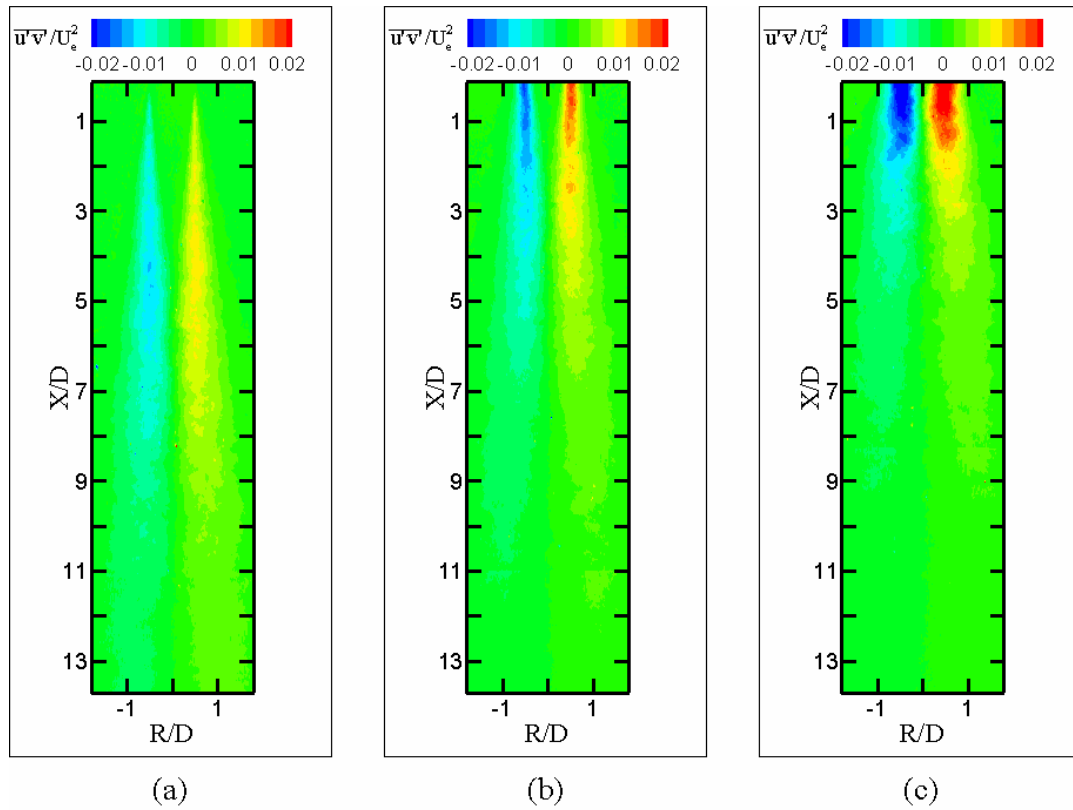


Figure 6.17: Whole field variation in fluctuating velocity correlation $\overline{u'v'}/U_c^2$ - (a) unexcited jet, (b) first stage ASEJ, (c) second stage ASEJ.

Whole field variation of mean flow kinetic energy, Q^2 , is presented in Figs. 6.18 a, b, & c, for the unexcited, first, and second stage ASEJ, respectively normalized by U_c^2 . From Fig. 6.18, it is clear that the acoustic self-excitation has the effect of reducing the magnitude of the mean flow kinetic energy for both the first and second stage ASEJ compared to the unexcited jet. Recall, that the potential core remained for between 4 and 5 pipe nozzle diameters for the unexcited jet and between 2.5 and 3 pipe nozzle diameters for the first stage ASEJ (see Fig. 6.6). In Figs. 6.18 a & b it is shown that the magnitude of Q^2 / U_c^2 for the unexcited jet and first stage ASEJ, respectively begins to decay at the same locations as the potential core of these two jets. Thus, it is clear that the mean flow kinetic energy is associated with the jets potential core. It is shown in Fig 6.18 c that the potential core of the second stage ASEJ is destroyed shortly after the collar exit.

Whole field variation of the turbulent kinetic energy, q^2 , is presented in Figs. 6.19 a, b, & c for the unexcited jet, first, and second stage ASEJ, respectively normalized by U_c^2 . In Fig 6.19 it is shown that the acoustic self-excitation has the effect of increasing the magnitude of q^2 for both first and second stage ASEJ. From Figs. 6.19 a & b it is evident by the low magnitude of q^2 / U_c^2 in the jets potential core that q^2 is associated with the developing shear layer of the jet flow. Comparing Figs. 6.18, and 6.19 it is seen that acoustic self-excitation has the effect of redistributing energy from the mean flow kinetic energy to the turbulent kinetic energy closer to the collar exit for first and second stage ASEJ than to the pipe exit in the unexcited jet.

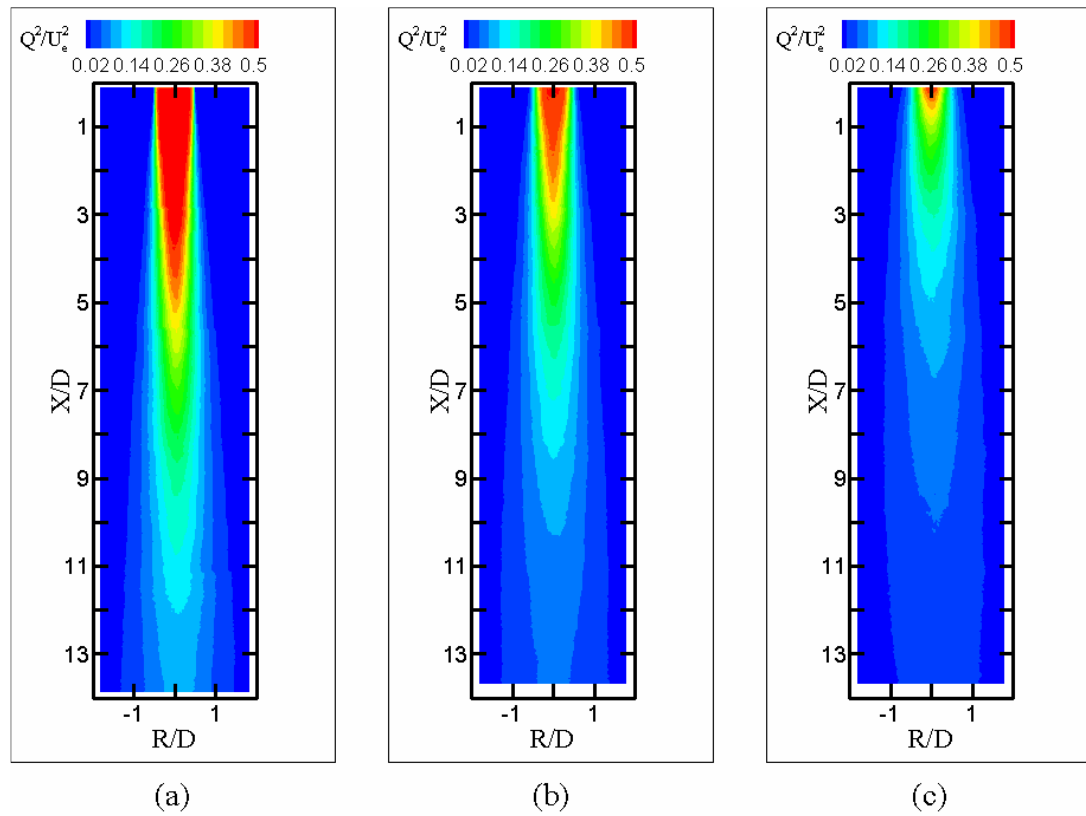


Figure 6.18: Whole field variation of mean kinetic energy Q^2/U_e^2 - (a) unexcited jet, (b) first stage ASEJ, (c) second stage ASEJ.

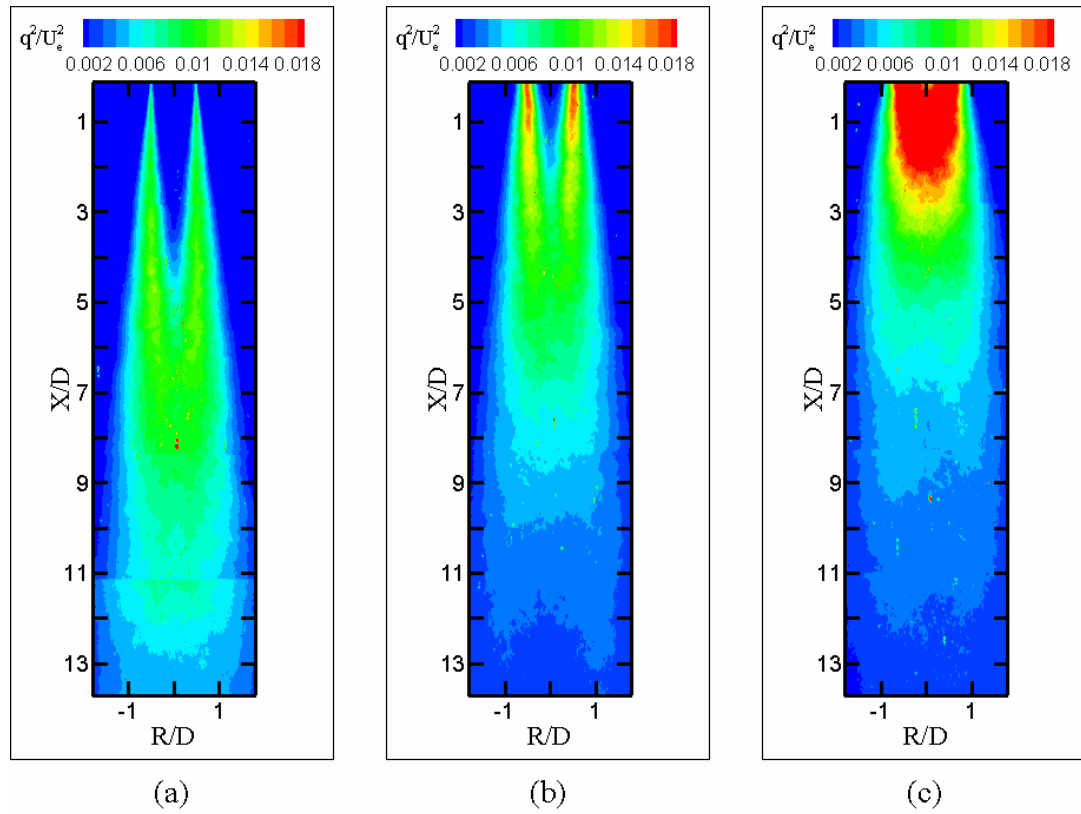


Figure 6.19: Whole field variation of turbulent kinetic energy q^2/U_e^2 - (a) unexcited jet, (b) first stage ASEJ, (c) second stage ASEJ.

7 CONCLUSIONS

An experimental study of the near-field flow structure in an acoustically self-excited jet (ASEJ) issuing into an enclosure was studied for three turbulent Reynolds numbers of $Re = 27,000$, $49,000$ and $71,000$. An acoustic study was performed in order to obtain quantitative measurements of the collar lengths resulting in first and second stage ASEJ for the three jet conditions studied ($Re = 27,000$, $49,000$ and $71,000$). The flow fields of first and second stage ASEJ for the three jet conditions studied were compared with that of an unexcited circular jet. Acoustic excitation was seen to cause an increase in near-field mixing and local turbulence intensity of the first and second stage ASEJ relative to the unexcited jet. For this study, the second stage excitation of the ASEN enhanced mixing and turbulence in the near-field compared to the first stage. Whereas the near-field mixing was enhanced using the ASEN, further downstream, the entrainment rate was almost the same as for the unexcited jet. Also, the far-field turbulence was diminished in comparison to the unexcited jet.

It is recommended that more analysis of the current data be completed such as a POD analysis identifying the dominant modes within the ASEJ compared to the unexcited jet. Also, it would be beneficial to take stereoscopic PIV measurements of an ASEJ to obtain the third component of velocity for the planar data obtained in order to better characterize the near-field flow structure of an ASEJ compared to an unexcited jet. Stereoscopic PIV would be especially helpful in the three dimensional quantitative characterization of the complex vortices that have been shown to emanate from the exit of an elliptical ASEJ (Husain and Hussain (1999)).

To this author's knowledge, the ASEJ has not found wide spread use in any real-world applications in the industry. This could be due to the loud pure tone the jet produces which could be considered an annoyance. Therefore, it is thought that the ASEJ could be scaled down such that the pure tone becomes inaudible to humans. Quite possibly the ASEJ may become useful at a smaller scale and it would be worthwhile to study the ASEJ at such a scale. Finally, the effect oscillating jets have on jet impingement heat transfer and mixing of combustibles has been studied at larger scales; however, not in great detail. If the ASEJ was to become useful at smaller scales it would likely be in the area of heat or mass transfer. Therefore, the ASEJ could be studied at smaller scales applied to jet impingement heat transfer or maybe spray cooling.

BIBLIOGRAPHY

- Adrian, R.J., 2005, "Twenty years of particle image velocimetry," *Experiments in Fluids*, **39**, pp. 159-169.
- Adrian, R.J., 1984, "Scattering particle characteristics and their effect on pulsed laser measurements of fluid flow: speckle velocimetry vs particle image velocimetry," *Applied Optics*, **23**, pp. 1690-1691.
- Binder, G. and Favre-Marinet M., 1973, "Mixing Improvement in Pulsating Turbulent Jets," *Proceedings of the Symposium of the Fluid Mechanics of Mixing, ASME, June 1973, Atlanta Georgia*, pp. 167-172.
- Can, M. and Etemoglu, A.B., 2003, "Investigation into Methods of Enhancing Heat Transfer Under Impinging Air Jets," *Experimental Heat Transfer*, **16**, pp. 171-190.
- Crow, S.C. and Champaign, F.H., 1971, "Orderly structure in jet turbulence," *Journal of Fluid Mechanics*, **48**, pp. 547-591.
- Cvetinovic, D.B., Ukai, M., Nakabe, K. and Suzuki, K., 2000, "Visualizations on Flow Structures of a Self-Sustained Oscillating Jet and its Enhanced Region of Impingement Heat Transfer," *Proceedings of the 9th International Symposium on Flow Visualization held at Heriot-Watt University in Edinburgh 2000*, paper no. 70.
- Dano, B.P.E., 2005, "Interactions of a fully Modulated Inclined Jet with a Crossflow," Ph.D. thesis, Oregon State University, Corvallis.
- Drobniak, S. and Klajny, R., 2002, "Coherent structures of free acoustically stimulated jet, *Journal of Turbulence*," **3**, pp. 2-29.
- Figliola, R.S. and Beasley, B.E., 2000, "Theory and Design for Mechanical Measurements, 3rd addition," John Wiley & Sons, Inc..
- Hasan, M.A.Z and Hussain, A.K.M.F., 1979, "A formula for resonance frequencies of a whistler nozzle," *Journal of the Acoustical Society of America*, **65**, pp. 1140-1142.
- Hasan, M.A.Z and Hussain, A.K.M.F., 1982, "The self-excited axisymmetric jet," *Journal of Fluid Mechanics*, **115**, pp. 59-89.
- Herman, C., 2000, "The Impact of Flow Oscillations on Convective Heat Transfer," *Annual Review of Heat Transfer*, **11**, pp. 495-561.

Hill, W.G. and Greene, P.R., 1977, "Increased Turbulent Jet Mixing Rates Obtained by Self-Excited Acoustic Oscillations," *Journal of Fluids Engineering*, **99**, pp. 520-525.

Husain, H. and Hussain, A.K.M.F., 1999, "The elliptic whistler jet," *Journal of Fluid Mechanics*, **397**, pp. 23-44.

Hussain, A.K.M.F. and Hasan, M.A.Z., 1983, "The 'whistler-nozzle' phenomenon," *Journal of Fluid Mechanics*, **134**, pp. 431-458.

Hussain, A.K.M.F. and Clark, A.R., 1981, "On the Coherent structure of the axisymmetric mixing layer: a flow-visualization study," *Journal of Fluid Mechanics*, **104**, pp. 263-294.

Hussain, A.K.M.F. and Zaman, K.B.M.Q., 1980, "Vortex pairing in a circular jet under controlled excitation. Part 2. Coherent structure dynamics," *Journal of Fluid Mechanics*, **101**, pp. 493-544.

Hwang, S.D. and Cho, H.H., 2003, "Effects of Acoustic excitation positions on heat transfer and flow in axisymmetric impinging jet: main jet excitation and shear layer excitation," *International Journal of Heat and Fluid Flow*, **24**, pp. 199-209.

Keane, R.D. and Adrian, R.J., 1992, "Theory of cross-correlation analysis of PIV images," *Applied Scientific Research*, **49**, pp. 191-215.

Lyons, K.M. and Parr, T.P., 1997, "Characterization of an Acoustically Forced Jet Using Particle Image Velocimetry (PIV)," *Proceedings of the ASME Fluids Engineering Summer Meeting, June 22-26*, paper no. FEDS97-3096.

Nathan, G.J., Alwahabi, Z.T., Newbold, G.J.R., and Nobes, D.S., 2006, "Impacts of a jet's exit flow pattern on mixing and combustion performance," *Progress in Energy and Combustion Science*, **32**, pp. 496-538.

Nathan, G.J., Hill, S.J., and Luxton, R.E., 1998, "An axisymmetric 'fluidic' nozzle to generate jet precession," *Journal of Fluid Mechanics*, **370**, pp. 347-380.

Page, R.H., Chinnock, P.S., and Seyed-Yagoobi, J., 1995, "Self-Oscillation Enhancement of Impingement Jet Heat Transfer," *Journal of Thermophysics and Heat Transfer*, **10**, pp. 380-382.

Raffel, M., Willert, C. and Kompenhans, J., 1998, "Particle Image Velocimetry; A Practical Guide," Springer.

Rockwell, D., 1983, "Oscillations of Impinging Shear Layers," *AIAA Journal*, **21**, pp. 645-664.

Schachenmann, A. and Rockwell, D., 1980, "Self-Sustained Oscillations of Turbulent Pipe Flow Terminated by an Axisymmetric Cavity," *Journal of Sound and Vibration*, **73**, pp. 61-72.

Tenneks and Lumley, 1972, "A First Course in Turbulence," The MIT Press, Cambridge, MS.

Tianshu, L. and Sullivan, J.P., 1996, "Heat transfer and flow structures in an excited circular impinging jet," *International Journal of Heat and Mass Transfer*, **39**, pp. 3695-3706.

Wong, C.Y., Lanspeary, P.V., Nathan, G.J., Kelso, R.M., and O'doherty, T., 2003, "Phase-averaged velocity in a fluidic precessing jet nozzle and its near external field," *Experimental Thermal and Fluid Science*, **27**, pp. 515-524.

Zaman, K.B.M.Q. and Hussain, A.K.M.F., 1980, "Vortex pairing in a circular jet under controlled excitation. Part 1. General jet Response," *Journal of Fluid Mechanics*, **101**, pp. 449-491

Appendices

APPENDIX A: CALIBRATION

A.1 Calibration of pressure transducers

The differential pressure transducers were calibrated using the laboratory calibration unit. The laboratory calibration unit consists of a pipe system having fittings to attach the pressure transducers to be calibrated, lab compressed air source and an Omega® NIST traceable hand held pressure calibration unit. The calibration curves along with their functional relationships for the two pressure transducers used in this study are shown below in Figs A.1 and A.2.

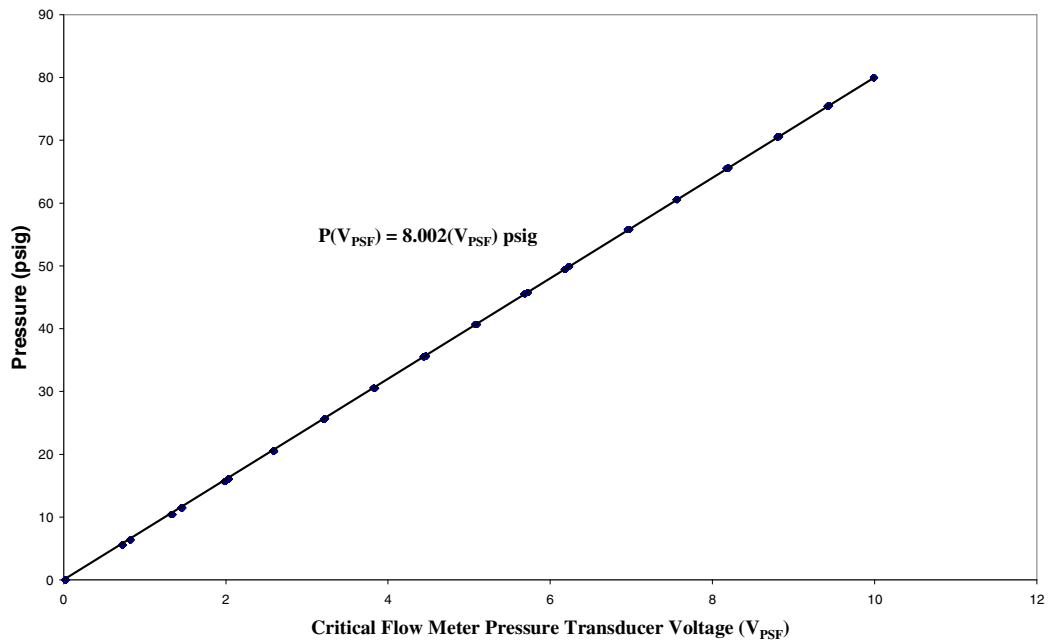


Figure A.1: Calibration curve for critical flow meter pressure transducer.

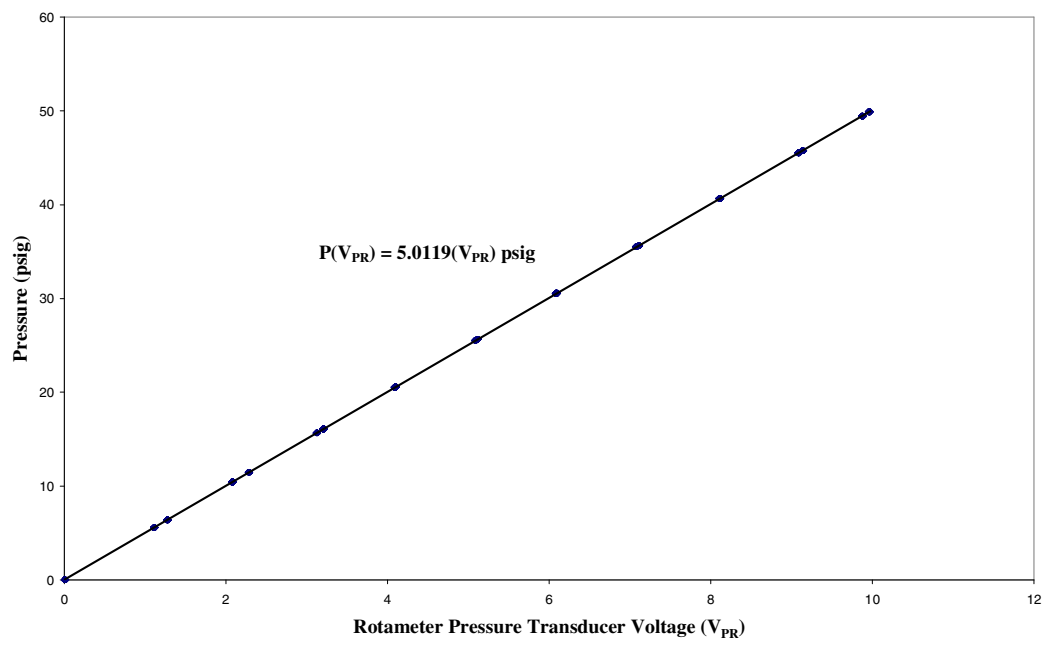


Figure A.2: Calibration curve for the rotameter pressure transducer.

A.2 Calibration of thermocouples

The two thermocouples used in this study were calibrated using a constant temperature water bath and a hand held Omega® calibration unit with a NIST traceable RTD. The calibration data for the two thermocouples used is shown below in Figs A.3 and A.4.

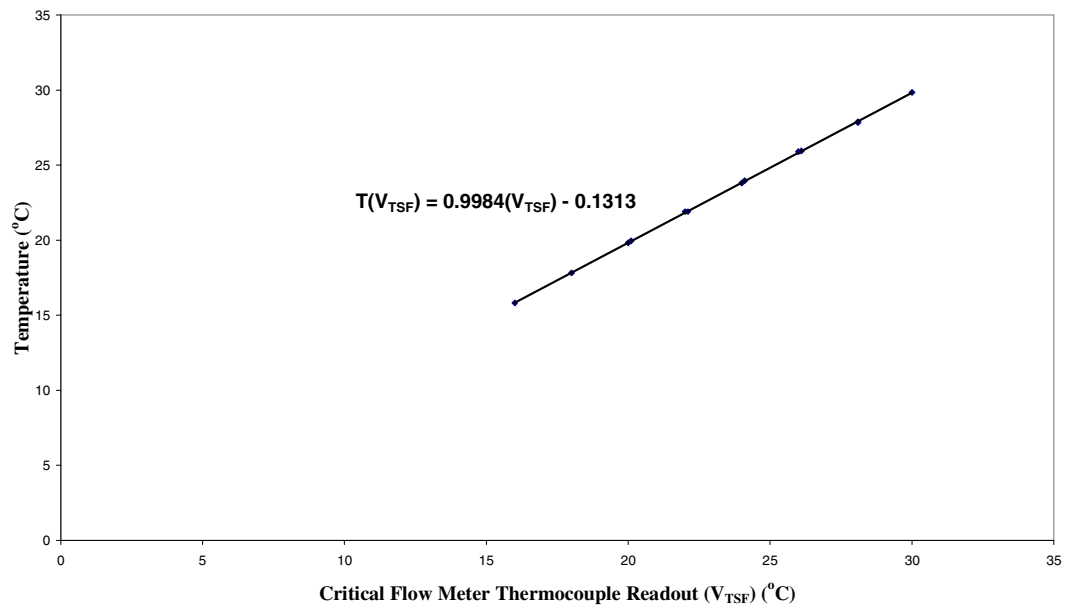


Figure A.3: Calibration curve for the critical flow meter thermocouple.

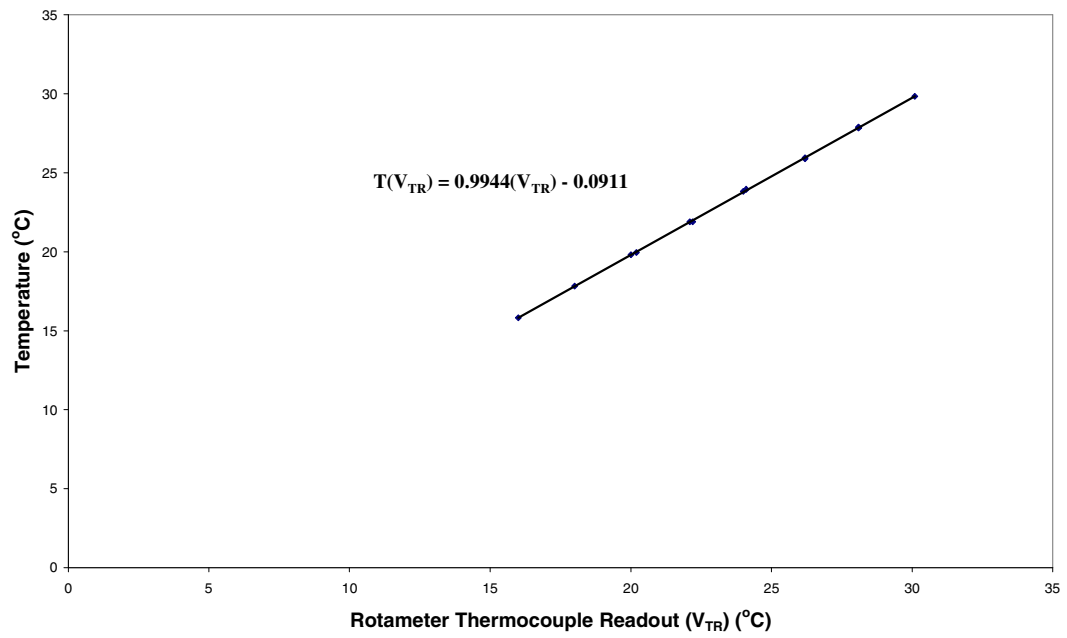


Figure A.4: Calibration curve for the rotameter thermocouple.

A.3 Calibration of microphone

The condenser microphone (Marshall electronics, MXL 603s studio condenser microphone) calibration was carried out in a homemade calibration unit that consisted of a box lined with egg crate foam having a 240 W 15.2 cm x 20.3 cm Pioneer car audio speaker mounted to it. A sinusoidal waveform was input to the speaker from a Tektronix® AFG2020 function generator that was amplified by a 250 W Kenwood KAC5201 car audio amplifier. The microphone was calibrated against an integrating sound level meter (Ono Sokki™, LA-2111). The functional relationship of the overall sound pressure level depended on the voltage coming from the microphone and the frequency of the signal. Thus the calibration curve for this instrument was a three dimensional curve. A trial version of Table Curve 3D® was used to generate the following curve fit in Eq. A.1 for the sample of calibration data shown in Table A.2.

$$L_p(f, v_{rms}) = a + bf + cf \ln f + df^{1.5} + ef^2 + ff^2 \ln f + \frac{gf}{\ln f} + h \ln v_{rms} \quad (\text{A.1})$$

Where, L_p is the over all sound pressure level (dB), f is the signal frequency (Hz) and v_{rms} is the root mean square voltage signal coming from the microphone. The values of the constant coefficient (i.e. a,b,c,...h) are listed in Table A.1.

Table A.1: Constan coefficient values for microphone calibration curve.

a	b	c	d	e	f	g	h
-7439.40	-822.49	75.31	-2.92	0.047	-0.0036	2626.80	8.65

Table A.2 is a sample of the data that was collected for the microphone calibration. The full microphone calibration data set contains over one thousand columns. Therefore, the full microphone calibration data set is not presented here.

Table A.2: Calibration data for microphone		
RMS Voltage (V)	Sound Pressure (dB)	freq (Hz)
0.021181	71	500
0.021185	71	500
0.021186	71	500
0.021189	71	500
0.021187	71	500
0.021193	71	500
0.021189	71	500
0.021189	71	500
0.021186	71	500
0.021187	71	500
0.033926	75	500
0.033906	75	500
0.033916	75	500
0.033921	75	500
0.033924	75	500
0.033931	75	500
0.033908	75	500
0.033902	75	500
0.033897	75	500
0.033909	75	500

APPENDIX B: UNCERTAINTY CALCULATIONS

Uncertainty in data collected and reported in this manuscript was calculated in the same manner for all cases studied (i.e. $Re = 27,000$, $49,000$ and $71,000$). Therefore, only details of uncertainty calculation for the $Re = 49,000$ data will be presented here.

B.1 Uncertainty in mass flow data

Uncertainty in mass flow rate data was largely dependent upon uncertainty in the temperature and pressure measurements required to obtain that data. Mass flow rate measurements of both the main flow and seeded flow required temperature and pressure measurements to account for the compressibility of air. Once uncertainty in temperature and pressure measurements were known, the Kline-McClintock method (Figliola and Beasley 2000) was used to determine uncertainty due to propagation of errors through the functional relationships used to calculate the mass flow rates.

B.1.1 Uncertainty in temperature measurements

Uncertainties in temperature measurements were obtained using the relationship in Eq. B.1.

$$u_T = \sqrt{(B_T)^2 + (S_T t_{v,95\%})^2} \quad (\text{B.1})$$

B_T was bias error associated with the calibration of thermocouples. $S_T t_{v,95\%}$ accounts for precision error in temperature measurements due to temperature fluctuations during experimentation. S_T is the standard deviation of a particular set of temperature

data while $t_{v,95\%}$ is the t estimator (i.e. $t = 1.96$ for $v > 60$ samples) for a 95 percent precision interval taken from the student-t distribution for finite statistics.

The bias error of temperature measurements consisted of two sources of error and was calculated using Eq. B.2.

$$B_T = \sqrt{(S_{TV}t_{v,95\%})^2 + (e_{T,STD})^2} \quad (B.2)$$

Curve fits were used to determine temperatures from the value indicated by the Omega® digital thermocouple readout. $S_{TV}t_{v,95\%}$ was the precision error introduced due by the use of the curve fits to determine actual temperatures from the calibrated thermocouples. S_{TV} was the standard error of the curve fits to the calibration data. Again, $t_{v,95\%}$ is the t estimator (i.e. $t = 1.96$ for $v > 60$ samples) for a 95% precision interval taken from the student-t distribution. The second term on the right hand side of Eq. B.2 accounts for the error introduced by the NIST traceable lab standard ($e_{T,STD}$) used for temperature (i.e. thermocouple) calibrations. Note that $e_{T,STD}$ is a constant for all cases and is equal to ± 0.3 °C. Shown in table B.1 were the uncertainty values calculated for temperature measurements on both the sonic flow meter (T_{SF}) and rotameter (T_R). Percent uncertainty for temperature measurements in all cases were based on the average temperature found from the temperature data recorded for that case.

Table B.1: Uncertainty values in temperature measurements for Re = 49,000

	Calibration		Data	Total
Thermocouple	$S_{TV}t_{v,95\%}$ (°C)	B_T (°C)	$S_T t_{v,95\%}$ (°C)	u_T (°C) [%]
T_{SF}	0.09	0.31	0.40	0.51 [2.3]
T_R	0.10	0.32	0.18	0.36 [1.6]

B.1.2 Uncertainty in pressure measurements

Uncertainty in the pressure measurements were estimated using the relationship in Eq. B.3.

$$u_p = \sqrt{(B_p)^2 + (S_p t_{v,95\%})^2} \quad (\text{B.3})$$

B_p was bias error associated with the calibration of pressure transducers. $S_p t_{v,95\%}$ accounts for precision error in pressure measurements due to pressure fluctuations during experimentation. S_p is the standard deviation of a particular set of pressure data while $t_{v,95\%}$ is the t estimator (i.e. $t = 1.96$ for $v > 60$ samples) for a 95% precision interval taken from the student-t distribution.

Bias error of pressure measurements consisted of two sources of error and was calculated using Eq. B.4.

$$B_p = \sqrt{(S_{PV} t_{v,95\%})^2 + (e_{P,STD \text{ of calibration}})^2} \quad (\text{B.4})$$

Curve fits were used to determine pressures from the voltage signal sent by the pressure transducers. $S_{PV} t_{v,95\%}$ was the precision error introduced through the use of the curve fits to determine actual pressures. S_{PV} was the standard error of the curves fit to the calibration data. Again, $t_{v,95\%}$ is the t estimator (i.e. $t = 1.96$ for $v > 60$ samples) for a 95% precision interval taken from the student-t distribution. The second term on

the right hand side of Eq. B.4 accounts for the error introduced by the NIST traceable lab standard ($e_{P,STD}$) used for pressure transducer calibrations. Note that $e_{P,STD}$ is a constant for all cases and is equal to ± 0.34 kPa (i.e. ± 0.05 psia). Shown in table B.2 were the uncertainty values calculated for pressure measurements on both the sonic flow meter (P_{SF}) and rotameter (P_R). Percent uncertainty for pressure measurements in all cases were based on the average pressure found from the pressure data recorded for that case.

Table B.2: Uncertainty values in pressure measurements for $Re = 49,000$

Pressure Transducer	Calibration		Data	Total
	$S_{PVT_{v,95\%}}$ (kPa)	B_P (kPa)	$S_{pt_{v,95\%}}$ (kPa)	u_P (kPa) [%]
P_{SF}	1.86	1.93	1.17	2.24 [0.49]
P_R	0.48	0.62	0.48	0.78 [0.47]

B.1.3 Uncertainty in primary mass flow rate

Mass flow rate of primary air flow to the jet was calculated using Eq. B.5 supplied with the sonic flow meter with an added unit conversion to SI units.

$$\dot{m}_{SF} \left(\frac{\text{kg}}{\text{s}} \right) = K_{SF} \left(\frac{\text{lbm} \cdot \sqrt{\text{R}}}{\text{s} \cdot \text{psia}} \right) \left[\frac{P_{SF}(\text{psia})}{\sqrt{T_{SF}(\text{R})}} \right] \left(\frac{0.4536 \text{kg}}{1 \text{lbm}} \right) \quad (\text{B.5})$$

Uncertainty in the primary mass flow rate was calculated using the Kline-McClintock method on Eq. B.5 shown below in Eq. B.6.

$$\mathbf{u}_{\text{MSF}} \left(\frac{\text{kg}}{\text{s}} \right) = \left(\frac{0.4536 \text{kg}}{1 \text{lbm}} \right) \sqrt{ \left(\frac{\partial \dot{m}_{\text{SF}} \left(\frac{\text{lbm}}{\text{s}} \right)}{\partial T_{\text{SF}} (\text{R})} \mathbf{u}_{T_{\text{SF}} (\text{R})} \right)^2 + \left(\frac{\partial \dot{m}_{\text{SF}} \left(\frac{\text{lbm}}{\text{s}} \right)}{\partial P_{\text{SF}} (\text{psia})} \mathbf{u}_{P_{\text{SF}} (\text{psia})} \right)^2 + \dots } \right. \\
 \left. \dots + \left(\frac{\partial \dot{m}_{\text{SF}} \left(\frac{\text{lbm}}{\text{s}} \right)}{\partial K_{\text{SF}} \left(\frac{\text{lbm} \cdot \sqrt{\text{R}}}{\text{s} \cdot \text{psia}} \right)} \mathbf{u}_{K_{\text{SF}} \left(\frac{\text{lbm} \cdot \sqrt{\text{R}}}{\text{s} \cdot \text{psia}} \right)} \right)^2 \right. \quad (\text{B.6})$$

T_{SF} and P_{SF} were the stagnation temperature and pressure respectively measured upstream of the sonic flow meter. Uncertainty in stagnation temperature and pressure measurements were those discussed in the previous sections. K_{SF} was the calibration coefficient supplied with the sonic flow meter which was dependent upon stagnation pressure. Eq. B.7 was the curve fit of the calibration coefficients dependence on stagnation pressure.

$$K_{\text{SF}} \left(\frac{\text{lbm} \cdot \sqrt{\text{R}}}{\text{s} \cdot \text{psia}} \right) = a + b P_{\text{SF}} (\text{psia}) + \frac{c}{\sqrt{P_{\text{SF}} (\text{psia})}} \quad (\text{B.7})$$

Uncertainty in sonic flow meter calibration coefficient was calculated using the Kline-McClintock method on Eq. B.7 shown below in Eq. B.8.

$$\mathbf{u}_{K_{\text{SF}} \left(\frac{\text{lbm} \cdot \sqrt{\text{R}}}{\text{s} \cdot \text{psia}} \right)} = \sqrt{ \left(\frac{\partial K_{\text{SF}} \left(\frac{\text{lbm} \cdot \sqrt{\text{R}}}{\text{s} \cdot \text{psia}} \right)}{\partial P_{\text{SF}} (\text{psia})} \mathbf{u}_{P_{\text{SF}} (\text{psia})} \right)^2 + \left(S_{\text{KP}t_{v,95\%}} \right)^2 } \quad (\text{B.8})$$

The first term on the right hand side of Eq. B.8 accounts for the propagation of error through the calculation of calibration coefficient using the functional relationship of Eq. B.7. $S_{\text{KP}t_{v,95\%}}$ is the standard error of the curve fit used to obtain the functional relationship of the calibration coefficient. Uncertainty in the calibration coefficient

was estimated to be $5.70(10^{-5})$ (lbm*R^{1/2}/s*psia) and uncertainty in primary mass flow rate was estimated to be $9.14(10^{-4})$ (kg/s) for the Re = 49,000 case.

B.1.4 Uncertainty in secondary mass flow rate

Mass flow rate of seeded air to the jet was calculated using Eq. B.9 supplied with the rotameter along with an added conversion from (L/min) to (kg/s).

$$\dot{m}_R = \dot{Q}_{RS} \left(\frac{L}{min} \right) \rho \left(\frac{kg}{m^3} \right) \left[\left(\frac{P_R (Hgmm)}{760 (Hgmm)} \right) \left(\frac{530 (R)}{T_R (R)} \right) \right]^{\frac{1}{2}} \left(\frac{1m^3}{1000L} \right) \left(\frac{1min}{60s} \right) \quad (B.9)$$

Uncertainty in mass flow rate through the seeder was determined using the Kline-McClintock method on Eq. B.9 as follows below in Eq. B.10.

$$u_{\dot{m}_R \left(\frac{kg}{s} \right)} = \sqrt{\left(\frac{\partial \dot{m}_R \left(\frac{L}{min} \right)}{\partial \dot{Q}_{RS} \left(\frac{L}{min} \right)} u_{\dot{Q}_{RS} \left(\frac{L}{min} \right)} \right)^2 + \left(\frac{\partial \dot{m}_R \left(\frac{L}{min} \right)}{\partial P_R (Hgmm)} u_{P_R (Hgmm)} \right)^2 + \dots} \quad (B.10)$$

$$\dots + \left(\frac{\partial \dot{m}_R \left(\frac{L}{min} \right)}{\partial T_R (^{\circ}R)} u_{T_R (^{\circ}R)} \right)^2 + \left(\frac{\partial \dot{m}_R \left(\frac{L}{min} \right)}{\partial \rho \left(\frac{kg}{m^3} \right)} u_{\rho \left(\frac{kg}{m^3} \right)} \right)^2$$

In Eqs. B.9 and B.10 P_R and T_R were the measured working pressure and temperature respectively of the rotameter. Uncertainty in these parameters was discussed in previous sections. In Eq. B.10 \dot{Q}_{RS} was the uncorrected volumetric flow rate of air through the seeder. The uncertainty in \dot{Q}_{RS} was due to the curve fit used to determine its value from the scale reading of the rotameter. The standard curve fit error and thus uncertainty in \dot{Q}_{RS} was determined to be 0.12 (L/min) using as

$$\dot{u}_{Q_R} = S_{yx} t_{v,95\%} \quad (\text{B.11})$$

where, $t_{v,95\%}$ was the student t distribution factor for a 95 percent confidence interval. The uncertainty in density measurements was determined by using the Kline-McClintock method on Eq. 4.8 the ideal gas law of chapter 4 and is shown below in Eq. B.12.

$$u_{\rho} = \sqrt{\left(\frac{\partial \rho}{\partial P_R \text{ (kPa)}} u_{P_R \text{ (kPa)}} \right)^2 + \left(\frac{\partial \rho}{\partial T_R \text{ (K)}} u_{T_R \text{ (K)}} \right)^2} \quad (\text{B.12})$$

Again the uncertainty in pressure and temperature measurements was discussed at the beginning of this chapter. For the $Re = 49,000$ case uncertainty in density was estimated to be $9.55(10^{-3})$ (kg/m³) and uncertainty in secondary mass flow rate was $6.51(10^{-6})$ (kg/s).

B.1.5 Uncertainty in total mass flow rate

Uncertainty in total mass flow rate was estimated using Eq. B.13 where, \dot{u}_{m_R} was the uncertainty in the mass flow rate measured using the rotameter and $\dot{u}_{m_{SF}}$ was the uncertainty in the mass flow rate measured using the sonic flow meter.

$$\dot{u}_m = \sqrt{\left(\dot{u}_{m_R} \right)^2 + \left(\dot{u}_{m_{SF}} \right)^2} \quad (\text{B.13})$$

For the $Re = 49,000$ case the total uncertainty in mass flow rate was determined to be $9.14(10^{-4})$ (kg/s) or 10.45 %. Percent uncertainty in all cases was based on the average mass flow rate recorded for that case.

B.2 Uncertainty in acoustic data

Uncertainty in overall sound pressure level (dB) measurements (u_{Lp}) were determined as

$$u_{Lp} = \sqrt{B_{Lp}^2 + u_{Lp,data}^2} \quad (B.14)$$

where, $u_{Lp,data}$ was the uncertainty due to fluctuations in the rms voltage and frequency used to calculate overall sound pressure level via the microphone calibration curve during experimentation. A Sequential perturbation (Figliola and Beasley (2000)) of the microphone calibration curve was used to determine $u_{Lp,data}$. The maximum standard deviation of rms voltage fluctuations and frequency fluctuations during experimentation was used as the perturbation parameters.

The bias error (B_{Lp}) introduced thru the calibration of the microphone used to obtain overall sound pressure level was estimated as

$$B_{Lp} = \sqrt{e_{Lp}^2 + S_{fLpV} t_{v,95\%} + u_{Lp,cali}^2} \quad (B.15)$$

where, e_{Lp} was the uncertainty of the standard microphone used for calibration of the microphone, $S_{fLpV} t_{v,95\%}$ was the standard curve fit error of the calibration curve fit to the calibration data, and $u_{Lp,cali}$ was determined using sequential perturbation on the calibration curve fit. The perturbation parameters used in the sequential perturbation were the maximum standard deviation of the rms voltage at a calibration point and the uncertainty in the frequency of the signal sent by the function generator. The maximum standard deviation in rms voltage at a calibration point was 7.67 mV and the uncertainty in frequency of the signal sent by the function generator was 5 Hz. The values of e_{Lp} , $S_{fLpV} t_{v,95\%}$, $u_{Lp,cali}$, and $u_{Lp,data}$ were 0.1 dB, 1.29 dB, 0.017 dB, and 3.57

dB, respectively. With the above values B_{Lp} turns out to be 1.27 dB resulting in an overall sound pressure level uncertainty of 3.79 dB.

B.3 Uncertainty in PIV data

Accuracy of a PIV measurement is largely dependent upon how accurate the particle displacement is measured. As discussed in chapter 5 a commonly accepted uncertainty in displacement is 0.1 pixels (Keane and Adrian (1992)) for a seed size of approximately 2-3 pixels in raw PIV images. In the current study the seed size is about 1 pixel in raw PIV images. The desired 2-3 pixel seed size is impossible to achieve in this study for two reasons. First, the seed size is kept small (i.e. 11 μm on average) in order to insure the seeds follow the flow field. Second, the field of view is relatively large in order to capture the entire flow field. However, (Dano 2005) validated the use of the 0.1 pixel uncertainty in displacement for a seed size of 1 pixel by creating artificial raw PIV images with a known velocity field in MatLab® and resolving the velocity fields with FlowManager® to characterize the error. Therefore, an uncertainty in particle displacement of 0.1 pixels is used to estimate the uncertainty of PIV measurements in this study.

B.3.1 Uncertainty in instantaneous velocity

The starting point for a PIV measurement is to obtain instantaneous whole field velocity measurements. A cross-correlation scheme is used to determine the displacement of particles in the flow field and solve the well known equation for velocity Eq. B.16, where Δx (m) is the measured particle displacement and Δt (s) is the user input time between laser flashes.

$$u_{ij} = \frac{\Delta x}{\Delta t} \quad (\text{B.16})$$

Uncertainty in instantaneous velocities is estimated by applying the Kline-McClintock method to Eq. B.16 as shown below in Eq. B.17.

$$u_{u_{ij}} = \sqrt{\left(\frac{\partial u_{ij}}{\partial \Delta x} u_{\Delta x}\right)^2 + \left(\frac{\partial u_{ij}}{\partial \Delta t} u_{\Delta t}\right)^2} \quad (\text{B.17})$$

The pixel pitch of the CCD camera is 6.45 $\mu\text{m}/\text{pixel}$ and the scale factor to convert from CCD space to image space is 5.37. Thus the uncertainty in displacement ($u_{\Delta x}$) for all cases is 3.46 μm determined by Eq. B.18.

$$u_{\Delta x} = (0.1 \text{ pixel}) \left(6.45 \frac{\mu\text{m}}{\text{pixel}} \right) (5.37) \quad (\text{B.18})$$

Uncertainty in camera timing ($u_{\Delta t}$) is given by the manufacturer to be $33(10^{-9})$ s which is three orders of magnitude less than the spatial uncertainty and is therefore neglected in uncertainty calculations. For $Re = 49,000$ cases Δt is 1.5 μs giving an uncertainty in instantaneous velocity of 2.31 m/s or 3.70 percent based on the free jet exit velocity.

B.3.2 Uncertainty in mean velocity

As was discussed in chapter 5 mean velocity in the streamwise direction at each location of the two dimensional velocity map was calculated using the relationship of Eq. B.19 where, U_{ij} and $u_{ij,k}$ where the streamwise components of mean and instantaneous velocity, respectively.

$$U_{ij} = \frac{1}{N} \sum_{k=1}^N u_{ij,k} \quad (\text{B.19})$$

The mean velocity in the cross stream direction is calculated in the same manner as Eq. B.19 and thus will not be shown here. Uncertainty in mean velocity was estimated by applying the Kline-McClintock method to Eq. B.19 and is shown below in Eq. B.20.

$$u_{U_{ij}} = \sqrt{\sum_{k=1}^N \left(\frac{\partial U_{ij}}{\partial u_k} u_{u_k} \right)^2} \quad (\text{B.20})$$

Writing out the summation in Eq. B.20 allowed for simplification and is shown below in equation B.21.

$$u_{U_{ij}} = \sqrt{\left(\frac{u_{u_1}}{N} \right)^2 + \left(\frac{u_{u_2}}{N} \right)^2 + \dots + \left(\frac{u_{u_N}}{N} \right)^2} = \sqrt{N \left(\frac{u_{u_{ij}}}{N} \right)^2} = \sqrt{\frac{u_{u_{ij}}^2}{N}} \quad (\text{B.21})$$

Note that the uncertainty in mean velocity is only dependent upon the uncertainty in instantaneous velocity u_v and the number of samples N (i.e. 750 samples) used to calculate the mean velocity. Therefore, the uncertainty in streamwise and cross stream velocity was equivalent. For the $Re = 49,000$ case uncertainty in mean velocity was 0.08 m/s or 0.13 percent based on the mean velocity at the exit of the free jet.

B.3.3 Uncertainty in fluctuating velocity

The uncertainty in fluctuating velocity in both the streamwise and cross stream directions were determined to be equivalent and were estimated using Eq. B.22.

$$u_{u'} = \sqrt{(u_v)^2 + (u_{u_{ij}})^2} \quad (\text{B.22})$$

For Re of 49,000 case $u_{u'}$ was 2.31 m/s or 7.89 percent based on the maximum fluctuation present for these cases.

B.3.4 Uncertainty in vorticity calculations

Dantec Dynamics® Flow Manager® software was used to process the PIV data and calculate the mean vorticity field using the finite difference approximation in Eq. B.23.

$$\Omega_z(m, n) = \frac{V_{m+1, n} - V_{m-1, n}}{\Delta x} - \frac{U_{m, n+1} - U_{m, n-1}}{\Delta y} \quad (\text{B.23})$$

Uncertainty in mean vorticity calculations were estimated by applying the Kline-McClintock method to Eq. B.23 (i.e. Eq. B.26) after making the substitutions shown in Eq. B.24 and B.25.

$$A = V_{m+1, n} - V_{m-1, n} \quad (\text{B.24})$$

$$B = U_{m, n+1} - U_{m, n-1} \quad (\text{B.25})$$

$$u_\Omega = \sqrt{\left(\frac{1}{\Delta x} u_A\right)^2 + \left(\frac{1}{\Delta y} u_B\right)^2} \quad (\text{B.26})$$

Uncertainty in the substitution variables A and B was determined by applying the Kline-McClintock method to Eq. B.24 and B.25 respectively shown below in Eq. B.27.

$$u_A = u_B = \sqrt{\left(u_{U_{ij}}\right)^2 + \left(u_{V_{ij}}\right)^2} \quad (\text{B.27})$$

For Re = 49,000 case Δx was 278 μm , Δy was 557 μm , u_A and u_B was 0.12 (m/s) resulting in an uncertainty in mean vorticity of 479.06 (Hz) or 0.66 percent based on the maximum vorticity measured for this case.

B.3.5 Uncertainty in volumetric flow rate

Volumetric flow rate was calculated using the mean velocity maps and integrating across the jet from the centerline to a location where the velocity was greater than or equal to 5 percent of the local mean centerline velocity. The integration Eq. B.28 was split into a right and left side term because of the singularity at r equal to zero.

$$\dot{Q} = \bar{U}A = \int_0^{r_L} \bar{U}(r) \frac{2\pi r}{2} dr + \int_0^{r_R} \bar{U}(r) \frac{2\pi r}{2} dr \quad (\text{B.28})$$

A numerical integration scheme shown in Eq. B.29 was used to integrate the discrete data available to calculate volumetric flow rate.

$$\dot{Q} = \pi\Delta r \left(\sum_{i=1}^N \bar{U}(r_i)r_i \right)_L + \pi\Delta r \left(\sum_{i=1}^N \bar{U}(r_i)r_i \right)_R \quad (\text{B.29})$$

Eq. B.30 and B.31 is a result of splitting up the left and right sides and expanding the summations.

$$\dot{Q}_L = \pi\Delta r \left[\bar{U}(r_1)r_1 + \bar{U}(r_2)r_2 + \dots + \bar{U}(r_N)r_N \right]_L \quad (\text{B.30})$$

$$\dot{Q}_R = \pi\Delta r \left[\bar{U}(r_1)r_1 + \bar{U}(r_2)r_2 + \dots + \bar{U}(r_N)r_N \right]_R \quad (\text{B.31})$$

The uncertainty in volumetric flow data was estimated by applying the Kline-McClintock method to Eq. B.30 and B.31 and root sum squaring the results in Eq. B.32.

$$u_{\dot{Q}} = \sqrt{\left(u_{\dot{Q}_L} \right)^2 + \left(u_{\dot{Q}_R} \right)^2} \quad (\text{B.32})$$

For the $Re = 49,000$ case the uncertainty in volumetric flow data presented was $1.72(10^{-4}) \text{ m}^3/\text{s}$ or 1.28 percent based on the local volumetric flow rate of the fixed position used to calculate uncertainty in volumetric flow rate.

APPENDIX C: PIV DATA FOR THE REYNOLDS NUMBER OF 27000 AND 71000

In Appendix C PIV data for the jet study with a Reynolds number equal to 27,000 and 71,000 is presented. The data in this section is similar to that discussed in chapter 5. Thus, refer to chapter five for an in depth explanation of the data presented in here in Appendix C.

C.1 PIV data for the Reynolds number of 27,000

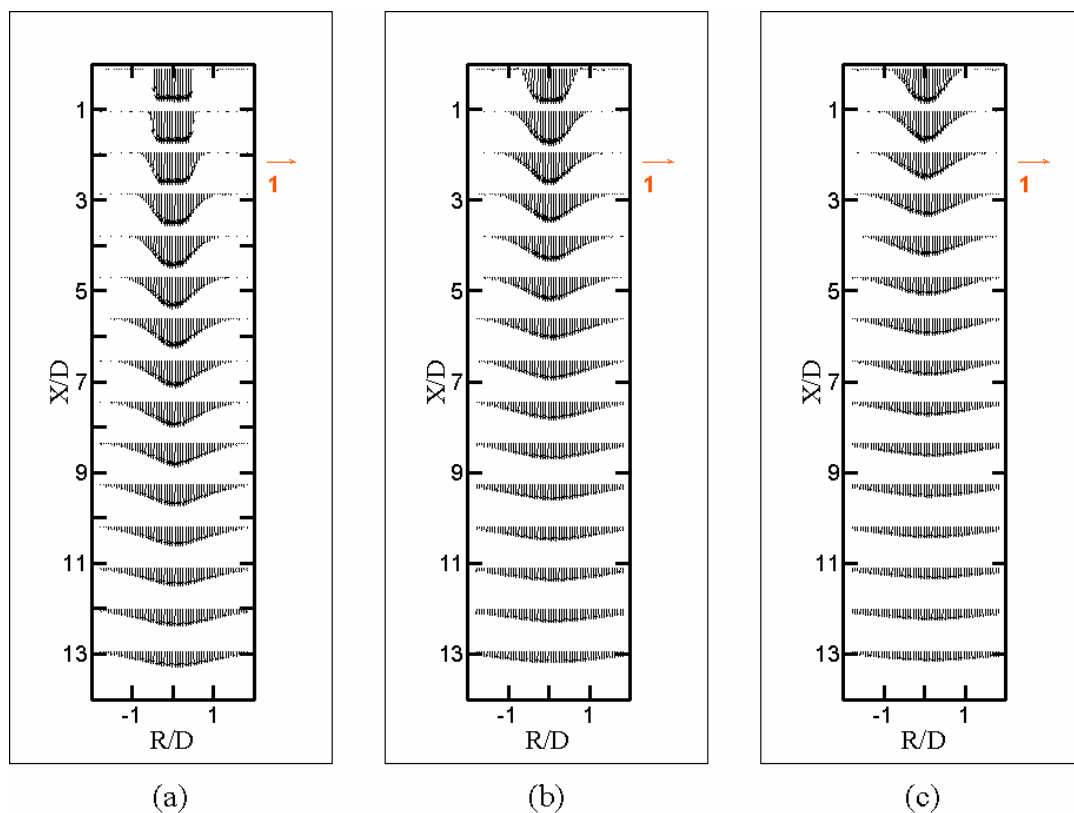


Figure C.1: Whole field streamwise variation of U/U_e - (a) unexcited jet; (b) first stage ASEJ; (c) second stage ASEJ.

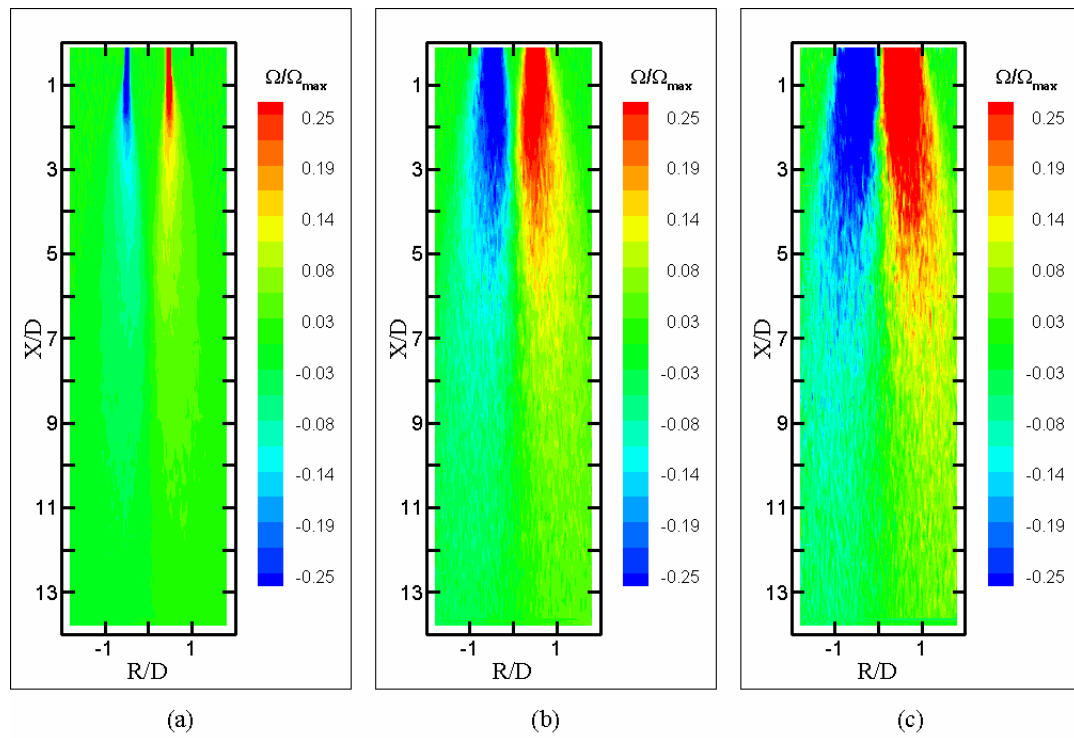


Figure C.2: Whole field streamwise variation of Ω/Ω_{\max} - (a) unexcited jet; (b) first stage ASEJ; (c) second stage ASEJ.

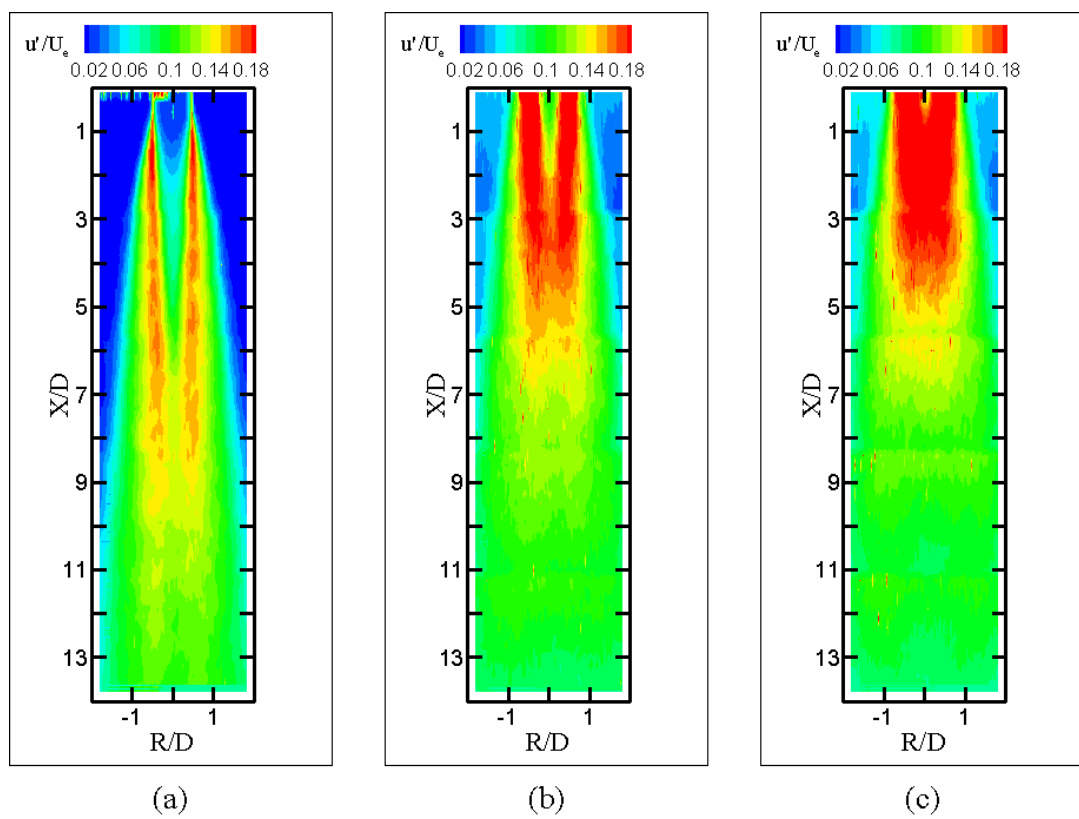


Figure C.3: Whole field streamwise variation of u'/U_e - (a) unexcited jet; (b) first stage ASEJ; (c) second stage ASEJ.

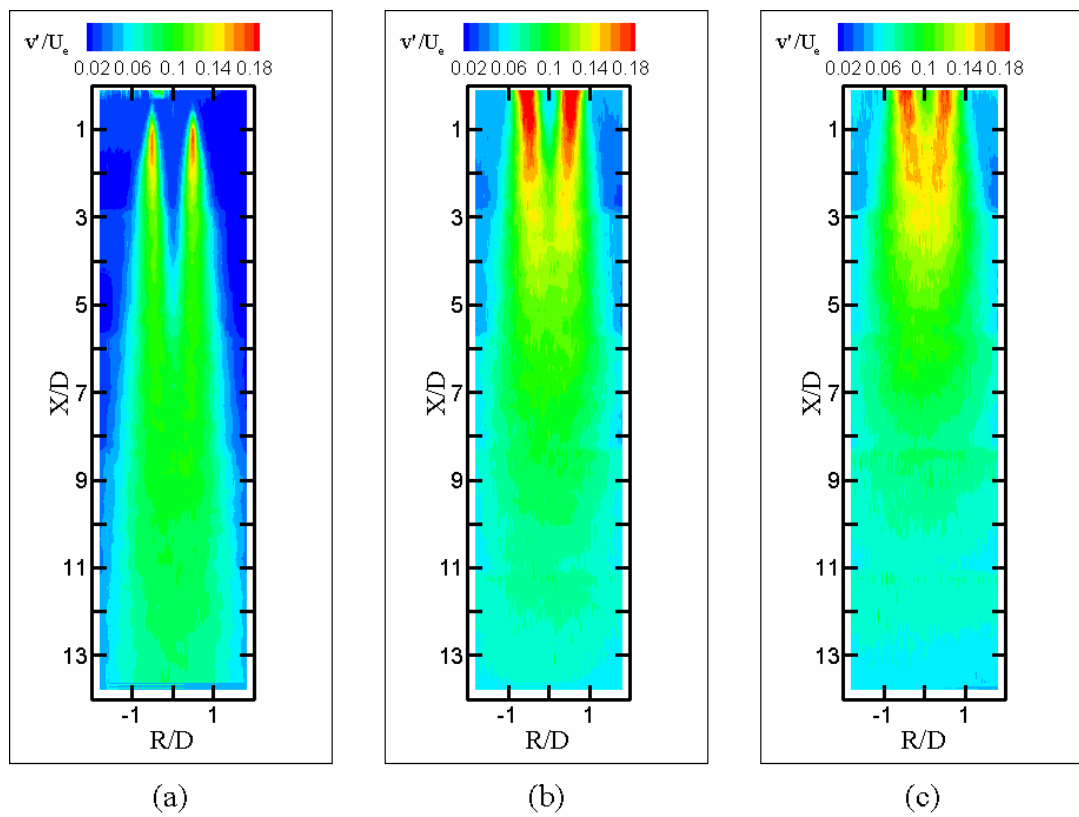


Figure C.4: Whole field streamwise variation of v'/U_e - (a) unexcited jet; (b) first stage ASEJ; (c) second stage ASEJ.

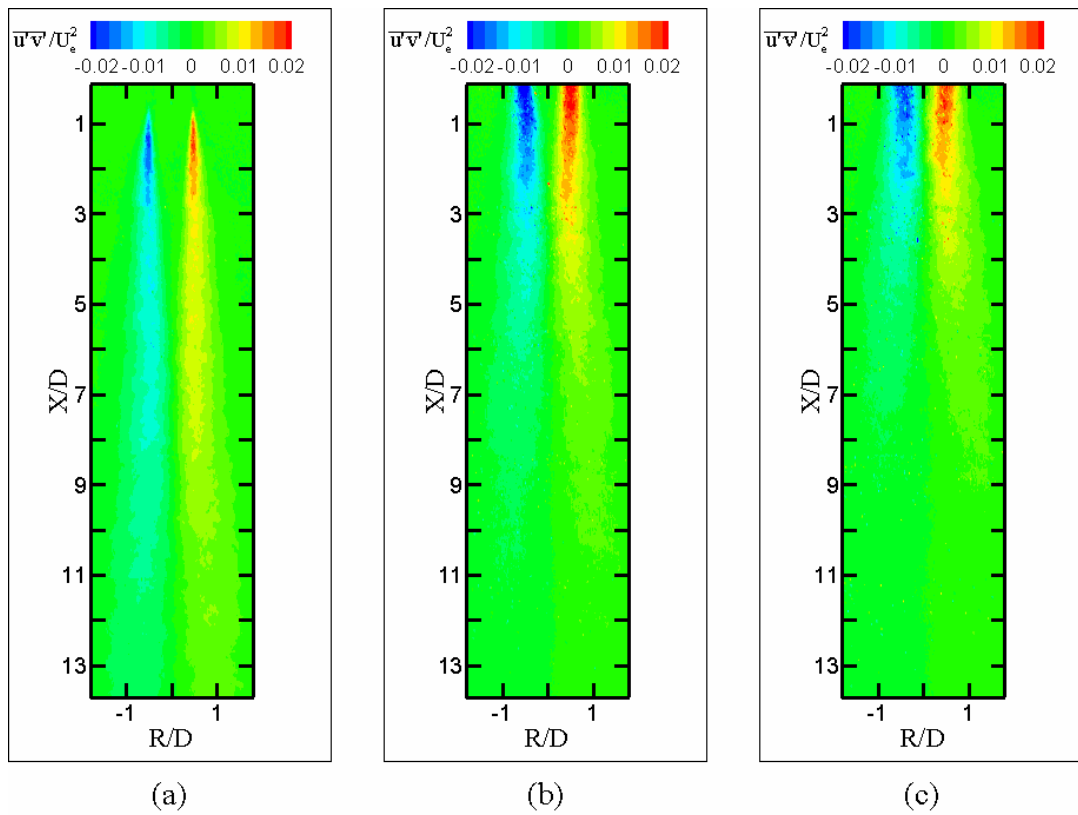


Figure C.5: Whole field variation in fluctuating velocity correlation $\overline{u'v'}/U_c^2$ - (a) unexcited jet; (b) first stage ASEJ; (c) second stage ASEJ.

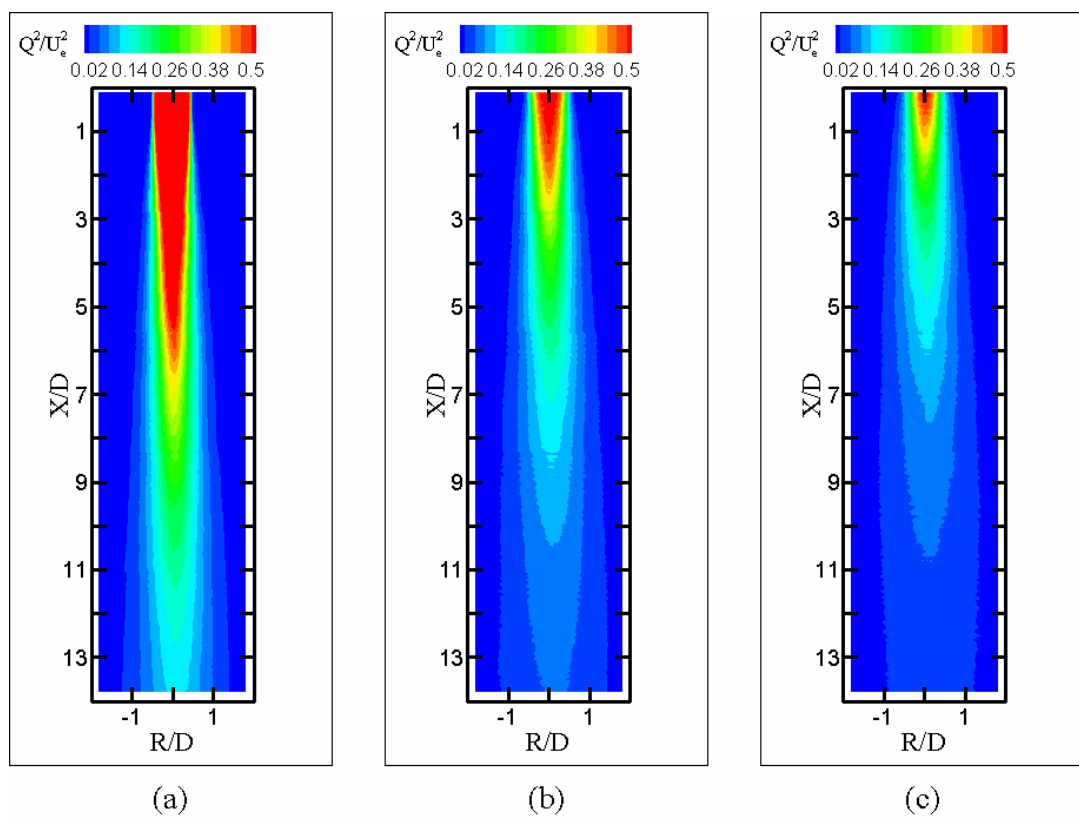


Figure C.6: Whole field variation of mean flow kinetic energy Q^2/U_e^2 - (a) unexcited jet; (b) first stage ASEJ; (c) second stage ASEJ.

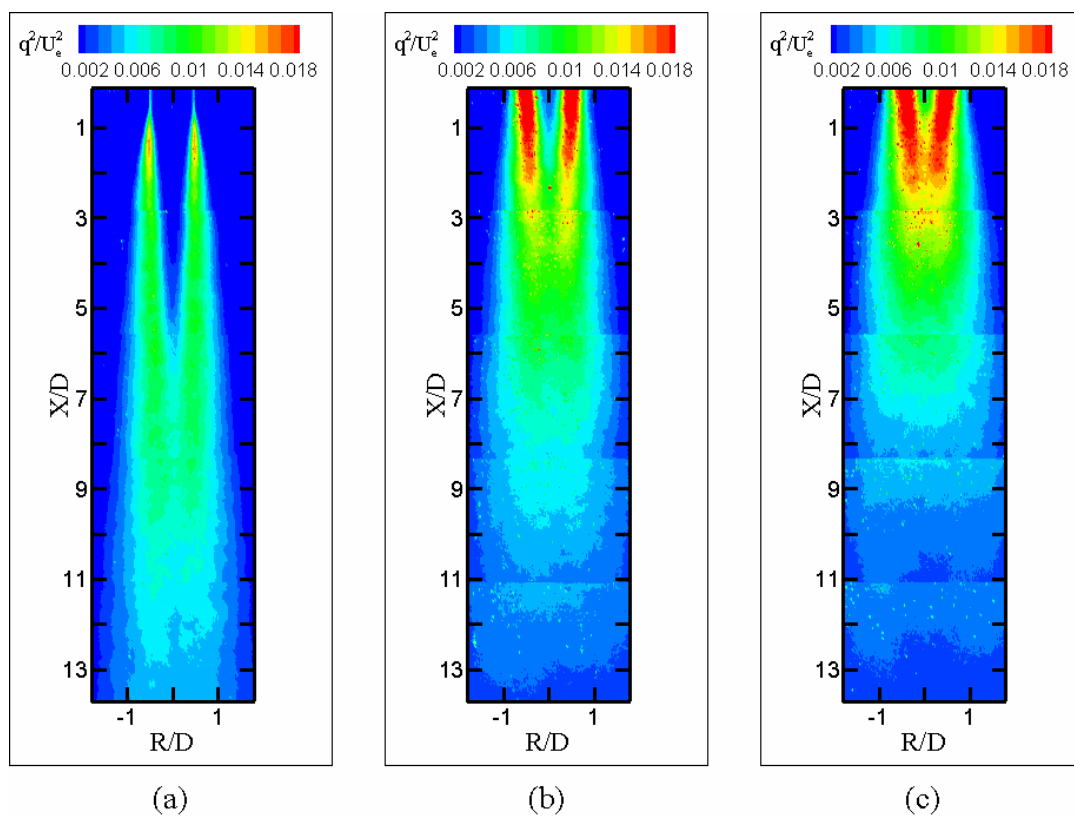


Figure C.7: Whole field variation of turbulent kinetic energy q^2/U_c^2 - (a) unexcited jet; (b) first stage ASEJ; (c) second stage ASEJ.

C.2 PIV data for Reynolds of 71,000

In the following section the PIV data for the jet study with a Reynolds number for 71,000 is presented. The data in this section is similar to that discussed in chapter 5. Thus, refer to chapter five for explanation of the data presented here.

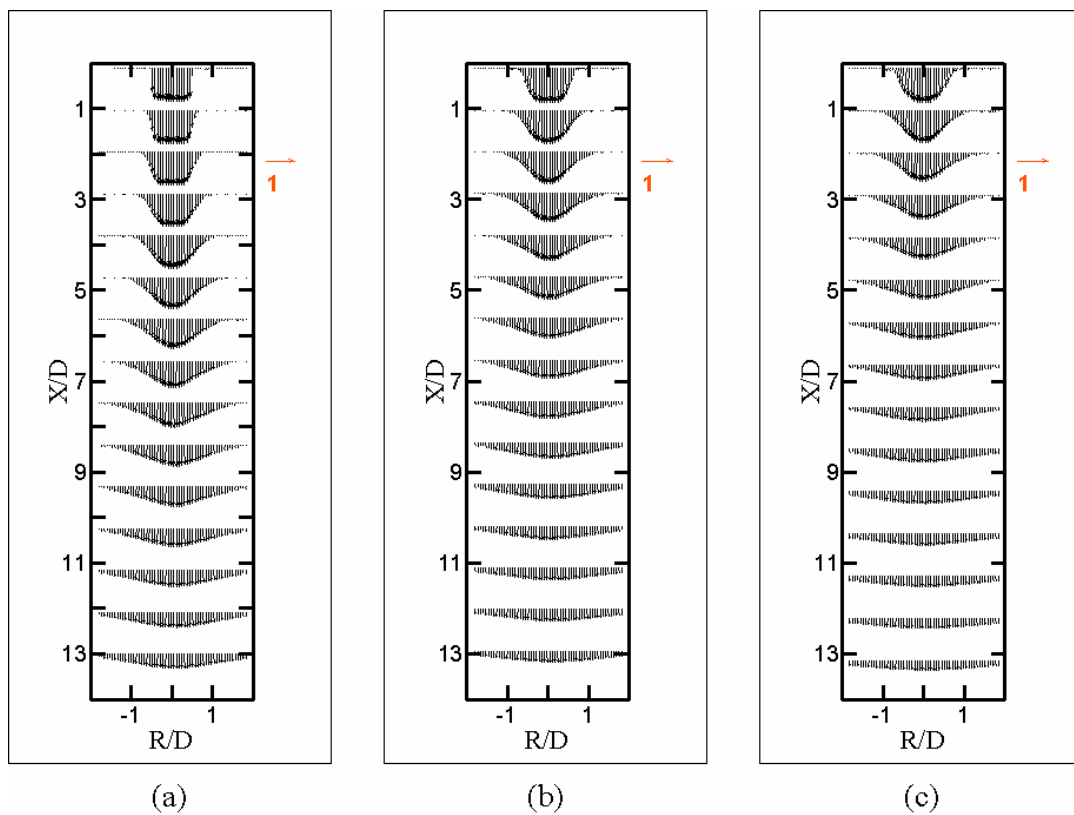


Figure C.8: Whole field streamwise variation of U/U_e - (a) unexcited jet; (b) first stage ASEJ; (c) second stage ASEJ.

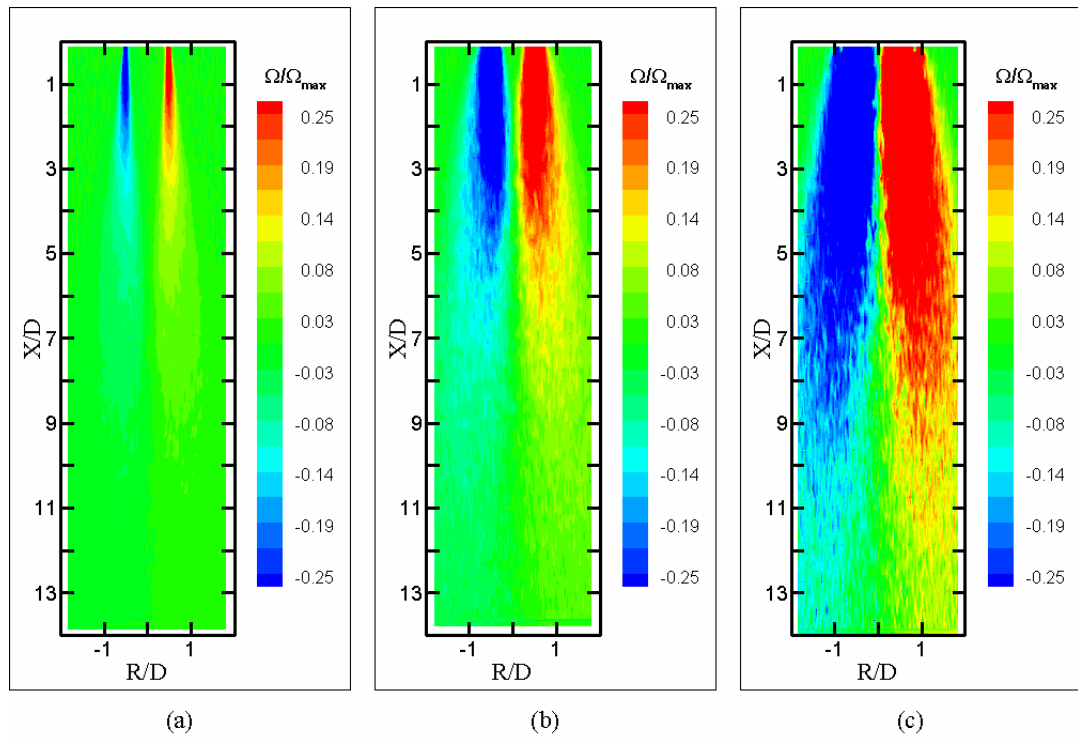


Figure C.9: Whole field variation of mean vorticity Ω/Ω_{\max} - (a) unexcited jet; (b) first stage ASEJ; (c) second stage ASEJ.

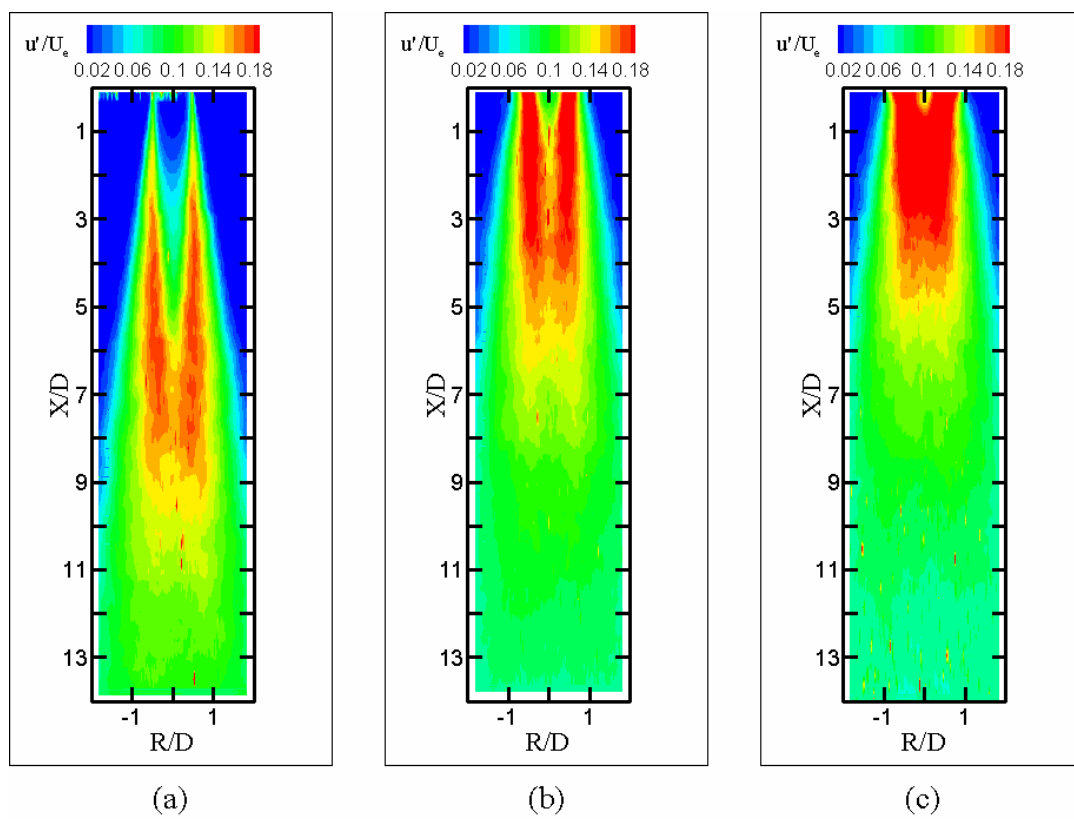


Figure C.10: Whole field streamwise variation of u'/U_e - (a) unexcited jet; (b) first stage ASEJ; (c) second stage ASEJ.

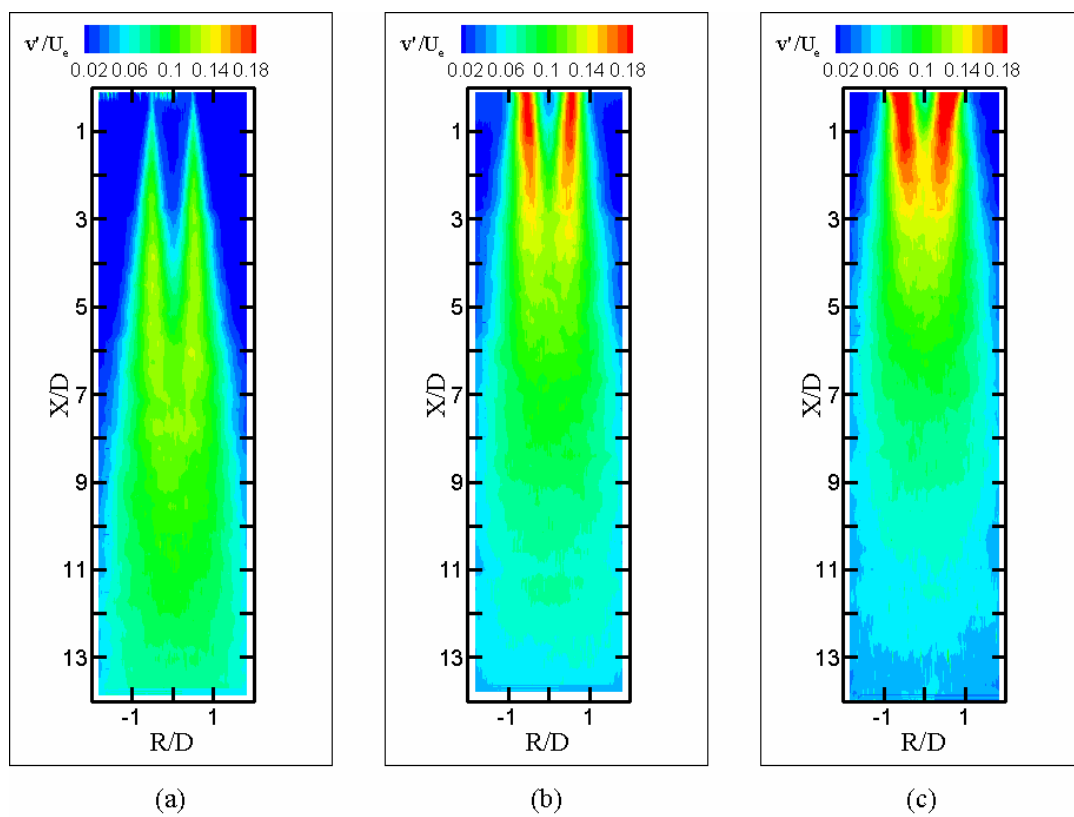


Figure C.11: Whole field streamwise variation of v'/U_e - (a) unexcited jet; (b) first stage ASEJ; (c) second stage ASEJ.

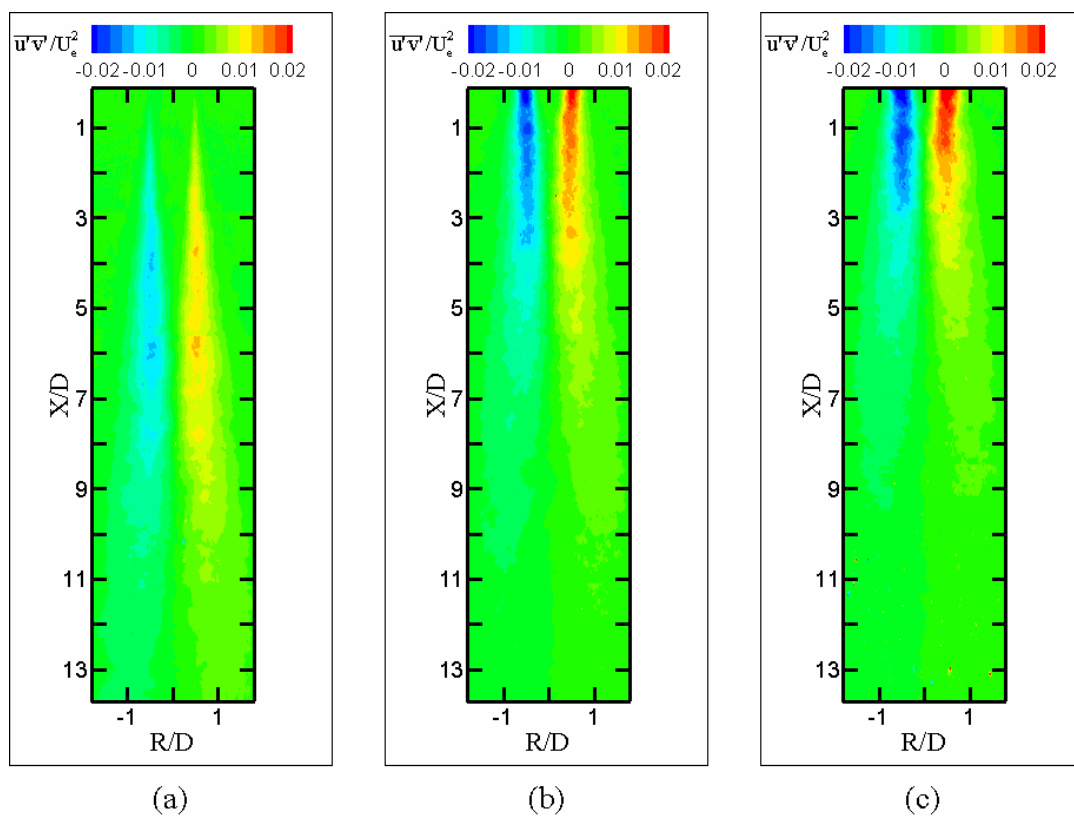


Figure C.12: Whole field variation in fluctuating velocity correlation $\overline{u'v'}/U_c^2$ - (a) unexcited jet; (b) first stage ASEJ; (c) second stage ASEJ.

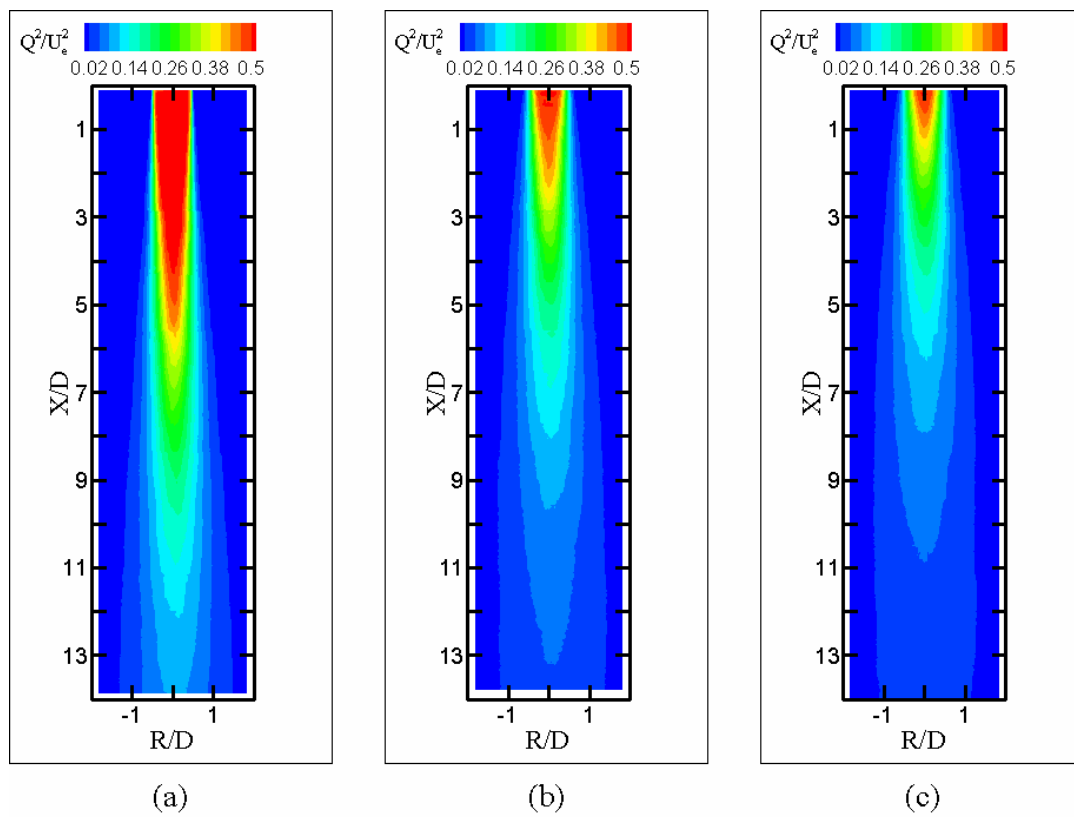


Figure C.13: Whole field variation of mean flow kinetic energy Q^2/U_e^2 - (a) unexcited jet; (b) first stage ASEJ; (c) second stage ASEJ.

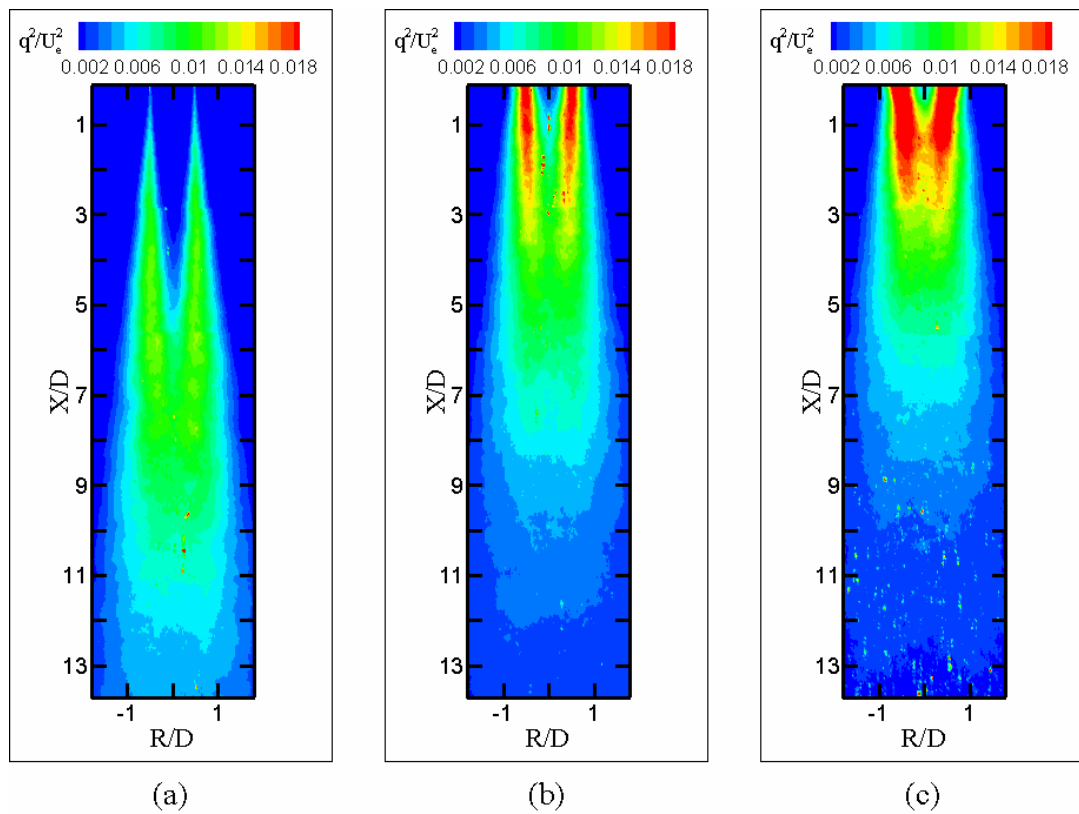


Figure C.14: Whole field variation of turbulent kinetic energy q^2/U_e^2 - (a) unexcited jet; (b) first stage ASEJ; (c) second stage ASEJ.

